

Investigation of dyestuff aggregation via static and dynamic light scattering and ultraviolet spectroscopy

Von der Fakultät für Naturwissenschaften
der Universität Paderborn

Dissertation

zur Erlangung des Grades eines
Doktors der Naturwissenschaften

— Dr. rer. nat. —

von

Mahnaz Doostdar

aus Rascht

November 2021

Die vorliegende Arbeit entstand in der Zeit von November 2017 bis Dezember 2021 im Fachbereich für Physikalische Chemie (Arbeitskreis Prof. Dr. Klaus Huber) der Fakultät für Naturwissenschaften der Universität Paderborn.

1. Gutachter: Prof. Dr. Klaus Huber
2. Gutachterin: Prof. Dr. Claudia Schmidt
3. Gutachter: Prof. Dr. Wolfgang Bremser

Hiermit erkläre ich, die vorliegende Dissertationsschrift selbstständig verfasst zu haben. Die dazu genutzte Literatur, zu Hilfeleistungen herangezogene Institutionen sowie Beiträge anderer Personen zu dieser Arbeit werden im Rahmen der Dissertationsschrift vollständig angegeben bzw. kenntlich gemacht.

Paderborn, November 2021

Mahnaz Doostdar

Acknowledgements

I would like to express my sincere gratitude to all people, who helped me during my studies and gave invaluable advice for my PhD.

In particular, I would like to thank Prof. Dr. Klaus Huber for supervision and all help and supports. Further thanks to Prof. Dr. Claudia Schmidt and Prof. Dr. Wolfgang Bremser for their willingness to act as referees.

Special thanks to Benjamin for being always supportive, giving great advice during the considerable time which he spent to help me in the new challenges.

Many thanks to my colleagues Fabian, Nico, Anne, Dominik, Leon and Wenke for their help and great moments of friendship. I would also like to thank Susanne, Rita, Gisela and Katrin for many helpful hints.

And thanks to my family, my parents, and my sister for all their love and support.

Kurzfassung

Aggregationen der Säurefarbstoffe Gelb, Blau und Rot werden mit time-resolved static und dynamic Lichtstreuung (TR-SLS/DLS) in Kombination mit UV/Vis-Spektroskopie untersucht. Die Experimente werden in Reinstwasser mit 5% Ammoniak bei 25 °C und in Gegenwart verschiedener Salze durchgeführt, wobei versucht wird, den pH-Wert der endgültigen Lösung über 10 zu halten. Zwei Lösungsmittel, nämlich PL1Cl mit 1% NH₄Cl und PL2P mit 1% Na₂HPO₄ werden als Referenzlösungsmittel zum Auflösen der Farbstoffe betrachtet. Im Gegensatz zum gelben Farbstoff zeigen blaue und rote Lösungen ein metastabiles Verhalten in PL1Cl, obwohl keine von ihnen Metastabilität in PL2P zeigt. Die UV/Vis-Spektroskopie im Wellenlängenbereich $300 \text{ nm} \leq \lambda \leq 800 \text{ nm}$ zeigt, dass alle drei Farbstoffe in PL2P besser löslich sind als in PL1Cl. In den Absorptionsspektren der roten und blauen Farbstoffe wird eine blau verschobene Absorptionsspitze beobachtet, die die Bildung von H-Aggregaten in blauen und roten Lösungen gezeigt werden kann.

Die Referenzlösungsmittel werden auf zwei Arten modifiziert: In der ersten Betrachtung werden den Referenzlösungsmitteln jeweils Benzylalkohol, Isopropanol und Guanidinsulfat zugesetzt, was unterschiedliche Löslichkeitspotentiale für die Farbstoffe aufzeigt. Die zweite Art der Modifizierung erfolgt durch das Einbringen verschiedener Salze der Hofmeister-Reihe in die Referenzlösungsmittel, da sie die Löslichkeit von Farbstoffen erheblich verändern können.

Mit den Ergebnissen aus UV-vis-spektroskopischen Messungen sind wir in der Lage, aus den verschiedenen untersuchten Salzen das geeignete Agens auszuwählen, um den Aggregationsprozess einzuleiten. Nach dieser Annahme ist CaCl₂ der geeignete Kandidat, um die Aggregation von Farbstoffen auszulösen.

Da die Löslichkeit von Farbstoff in Lösung stark vom pH-Wert abhängt, gilt die Salzsäure als zweites Agens, das die Aggregation auslöst. Da der Prozess schnell erledigt ist, wird die Säure nach und nach (Schritt für Schritt) zu den 4 ml jeder Farbstofflösung (gelber Farbstoff in der Konzentration von 1 mM und roter Farbstoff) gegeben von 0.8 und 0.2 mM).

Abstract

Aggregation of acidic dyestuffs yellow, blue and red is investigated via time-resolved static and dynamic light scattering in combination with UV-vis spectrometry. Experiments are carried out at 25°C in pure water and 5% ammonia and in the presence of different salts trying to keep the pH of final solution above 10. Two solvents as PL1Cl with 1% NH_4Cl and PL2P with 1% Na_2HPO_4 are considered as reference solvents to dissolve the dyestuffs. Unlike the yellow dyestuff, blue and red solutions exhibit a meta-stable behavior in *PL1Cl* although none of them show meta-stability in *PL2P*. The UV-vis spectroscopy in the wavelength range of $300\text{ nm} \leq \lambda \leq 800\text{ nm}$ reveals the solubility of all three dyestuffs in *PL2P* is better than *PL1Cl*. A blue shifted absorption peak is observed in the absorbance spectra of red and blue dyestuffs may declare the formation of H-aggregates in blue and red solutions.

Modification of the reference solvents is performed in two ways. In the first consideration, benzyl alcohol, isopropanol and guanidine sulphate are added to the reference solvents reveals different potentials of solubility for dyestuffs. Benzyl alcohol and isopropanol enhance the solubility of dyestuffs while guanidine sulphate reduces the solubility drastically. The second form of modification is done by introducing the different salts from Hofmeister series in the reference solvents as they can change the solubility of dyestuffs significantly.

With the results from UV-vis spectroscopy measurements we are able to select the appropriate agent among the different investigated salts in order to initiate the aggregation process. According to this assumption, CaCl_2 is the suitable candidate to trigger the aggregation of dyestuffs. Since the solubility of dyestuff in solution is strongly dependent on the pH values, the hydrochloric acid is considered as the second agent to start the aggregation. As the process is quickly done, the acid is added gradually (step by step) to the 4 ml of each dye solution (yellow dye in the concentration of 1 mmol.L^{-1} and red dye of 0.8 and 0.2 mmol.L^{-1}).

Contents

1	Introduction	1
1.1	Acidic Dyestuff	1
1.2	Solution Behavior of Dyestuffs	2
1.3	Outline of the Thesis	6
2	Methods and Instruments	7
2.1	UV-vis spectroscopy	7
2.1.1	Determination of the solubility limit	8
2.2	Light Scattering	9
2.2.1	Static Light Scattering (SLS)	9
2.2.2	Dynamic Light Scattering (DLS)	12
2.2.3	Scaling laws	15
2.3	Determination of the Refractive Index Increment	19
2.3.1	Refractive index increment of yellow and red dyestuffs in the applied solvents	20
2.4	Laser light scattering instruments	22
2.4.1	Single angle detection: ALV 5000E Compact Goniometer System	22
2.4.2	Multi angle detection: ALV/CGS3/MD-8 Multi detection Laser Light Scattering System	22
2.4.3	Data evaluation	25
2.5	Materials	28
2.6	Sample Preparation	28
2.6.1	Preparation of UV-vis spectroscopy samples	28
2.6.2	Preparation of Light Scattering Samples	30
3	Investigation of Dyestuff Solubility via UV-vis Spectroscopy	31
3.1	Solubility of Dyestuffs in Reference Solvents	31
3.2	Solubility of the Acidic Dyestuffs in the Presence of Additives	37
3.3	Effect of Ammonium Salts on the Aggregation of Acidic Dyestuffs	49
3.4	Effect of Chloride Salts on the Aggregation of Acidic Dyestuffs	53

4	Investigation of Dye stuff Aggregation via Static and Dynamic Light Scattering	59
4.1	Aggregation of Dye stuff Induced by Ca^{2+} Ions	59
4.1.1	Yellow Dye stuff Aggregation Induced by Adding $CaCl_2$	60
4.1.2	Red Dye stuff Aggregation Induced by Adding $CaCl_2$	67
4.2	Aggregation of Dye stuff Induced by Lowering the pH	71
4.2.1	Yellow Dye stuff Aggregation Induced by Lowering the pH	71
4.2.2	Red Dye stuff Aggregation Induced by Lowering the pH	76
5	Summary	83
6	Appendix I	87
7	Appendix II	97
8	Appendix III	109
	Bibliography	117

Introduction

1.1 Acidic Dyestuff

Acidic dyestuffs are a class of water soluble dyes with anionic properties. They are usually equipped with polar groups, acidic groups, and hydrophobic residues. The resulting molecular structure provides a suitable affinity to substrates like textiles and fibers. These dyes possess acidic groups to establish the bond between $-NH$ group of fiber and acid group of dye. In this form, dyes are attracted to the fiber resulting in a good fastness. For example, human hair as a protein fiber with numerous reactive functional groups is typically dyed with acidic dyes [1]. Figure 1.1 represents the structure of those three acidic rainbow dyestuffs which are investigated in detail in the present work.

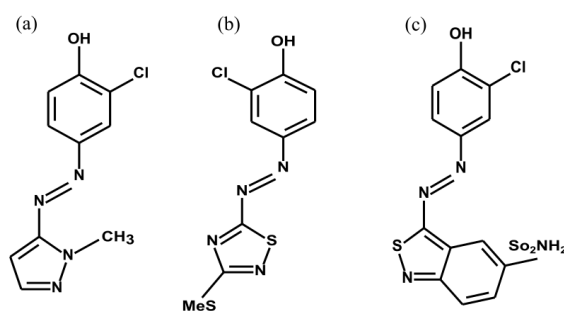
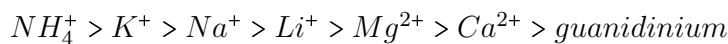
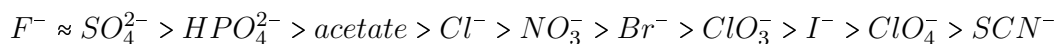


Figure 1.1. Chemical structure of acidic (a) yellow dyestuff (b) red dyestuff and (c) blue dyestuff.

1.2 Solution Behavior of Dyestuffs

Dyestuff aggregation in aqueous solutions has attracted attention since more than 100 years [2–6] and is of extreme importance from different points of view. Formation of the dye aggregates in solution is responsible for dramatic color change which is widely investigated by researchers in the field of dyeing chemistry [7–16]. Although a reduced solubility of dyestuffs is necessary for their adsorption on the fabric, it may also present difficulties in their application. The aggregated molecules can only enter the fiber very slowly and can not distribute easily through the fiber. To increase the migration of dyestuff molecules from the solution to the fiber, additives are used to facilitate dyeing action.

Numerous experimental studies have shown the importance of specific ion effects in so many physical, chemical and biological phenomena [17–28]. One of the most important studies about the effect of different ions has been accomplished by Franz Hofmeister, who studied the effects of cations and anions on the solubility of proteins. In 1888 a methodical survey was proposed by him through a qualitative ordering of ions based on their tendency to salt-out proteins from aqueous solutions [29]. Based on their ability to affect the solubility of proteins, ions are ordered into sequences which is called the Hofmeister series. On the basis of increasing the solubility (salting-in) from left to right the series are as follows for anions and cations:



As the aggregation of dyestuff shows similarities to protein aggregation and may work as a model for the reversible polymerization in physiological systems [30] or like protein fiber formation in protein folding diseases like Alzheimer [31], the Hofmeister series have been considered by several scientists to investigate the effect of anions and cations on the aggregation of dyestuffs.

A large number of studies have been focused on the interactions between anionic dye molecules and cations as well as those of cationic dyes with anions [32–35]. Although the most well-known interaction is the salting out effect leading to the precipitation of dyestuff, other effects of salts are also reported in literatures. The paper by R. Haller et al. at 1920 [36] introduced the additions of salts as a suitable medium which may raise the solubility (salting in effect), for instance in the case of cotton red.

In 1929 Ostwald et al. [37] pointed out that salts may cause an increase in solubility and dispersion. On 1930 and 1931 R. Tanaka discussed the color change of dyestuff

Congo blue after adding the salts and showed that the change does not depend on the pH changes but on the action of salts [38,39]. Moreover, he explained that in some cases, salting in and salting out effects can take place at the same concentration but distinct from one another as to time. Therefore, the effect of adding salt can be first to aggregate and then to dissolve the dyestuff. He investigated the effect of sodium sulphate on the solubility of Benzopurpurin 4B (direct red2) [40] where the solubility was boosted at fairly low concentrations of salt. It was shown that in a concentration of 0.001M Na_2SO_4 , the solubility reaches its maximum which is almost 5 times higher than in pure water and then it begins to reduce reaching the almost complete salting out effect with a concentration of 0.1M Na_2SO_4 .

The salting out effect was studied by Hamada et al. [4] where the aggregation of azo dyes was examined by means of UV-vis and NMR spectroscopy. He confirmed that the addition of salt to a simple monoazo dye in water increases the aggregation of dyestuff. Almost 15 years later Hamlin et al. [41] observed the same effect for some reactive dyes after adding sodium chloride whereas urea has reduced the aggregation of the same dyestuffs and elevated the amounts of monomeric species.

The effect of two well known cations Mg^{2+} and Na^+ on the solubility of anionic dyes and their mixtures was studied by Inglés et al. in 2000 [34]. A time resolved static light scattering (TR-SLS) enabled them not only to observe the effect of salts on the aggregation of dyestuffs but also to trace the evolution of aggregated particles during the time. Addition of Mg^{2+} ions to the aqueous solution of dyestuffs resulted in aggregates which can be originated from the interactions between bivalent Mg^{2+} ions and functional groups of the dyestuff molecules. UV-vis spectroscopy also confirmed a drastic change in the absorption behavior within 20 second after adding $MgSO_4$ to the dyestuff solution. In contrast, none of the measured parameters exhibited a significant trend with the Na_2SO_4 concentration. In the measured range of $2.16\text{ mM} < Na_2SO_4 < 11.3\text{ mM}$, the size and shape of the aggregates were small compared to respective addition of $MgSO_4$ and did not change with time, indicating a specific interaction of the salts and dyestuffs in case of Mg but not in case of Na .

In 2010 Fedoseeva et al. [42] studied a larger number of anions from the Hofmeister series (Cl^- , SCN^- , Br^- , SO_4^{2-}) which may induce aggregation in a water soluble cationic dyestuff. They applied a time-resolved surface second harmonic generation (TRSSHG) technique to analyze the aggregation of Malachite green (MG) induced by sodium salts. Interestingly the effect of NaCl on the aggregation of this cationic dyestuff was same as the one reported by Inglés on the aggregation of anionic dyestuff. UV-vis spectroscopy also confirmed that the absorption spectrum of MG does not change much by varying the NaCl concentrations, whereas it changes remarkably upon addition of NaSCN. The observed salt effect on the aggregation of MG was increased in the following order: $SO_4^{2-} < Cl^- < Br^- < SCN^-$.

The question that may now arise is about the effect of Hofmeister series cations on the acidic dyestuffs presented in section 1. In this work we try to answer this question by evaluating the effect of different salts on the solubility of three rainbow acidic dyestuffs in aqueous solutions. In other words, we use the Hofmeister series as a mantra to put a label on ion-specific behavior of acidic dyestuff under present considerations.

Precipitation of acidic dyestuff can be also achieved by lowering the pH of solution. This method has been widely used to remove the dyestuffs from the dye wastewater [35, 43–45] as the most problematic feature in the dyeing industries is the dye release to the environment in the form of wastewater. One of the first publications regarding the destruction of azo dyes was the paper of Schmidt, who reported on the reaction of azo dyes with chlorine, bromine and hypochlorous acid [46]. Later this was confirmed by other studies [47–49] as well as the degradation of dyestuffs with other acids e.g. chromic acid [50] and nitric acid [51]. In the framework of our study we choose hydrochloric acid HCl to initiate the precipitation of dye in solution.

In textile industries and dyeing processes, improving the uptake of dyestuff into the fiber is favorable. Boosting the uptake of dyestuff requires the appropriate additives which may enhance the solubility of dyestuff in aqueous solution. Benzyl alcohol is a well known alcohol with the formula $C_6H_5CH_2OH$ which shows strong polarity and limited water solubility. It is used as a general solvent for ink, coating, waxes, dyeing polyamide, and degreasing agent [52]. Another particular member in the family of alcohols is isopropyl alcohol or isopropanol with the formula $CH_3CHOHCH_3$ which dissolves a wide range of non-polar compounds and is used widely as a solvent [53]. Thus it can be expected that both benzyl alcohol and isopropanol increase the dyeing extent of acidic dye.

The aggregation or solubility limit of dye molecules is examined by UV-vis spectroscopy. Further details on the mechanism of particle formation can be provided by a time-resolved static and dynamic light scattering which are well established tools in combination with UV-vis spectroscopy [4, 6, 54, 55] to observe the structure of large molecules or colloids and provide insight in the aggregation behavior.

Static light scattering (SLS) can provide information on the shape and structure of the particles by determining the weight average molecular mass M_w and radius of gyration R_g from angular dependent scattering curves. In order to obtain these parameters, a calculation of refractive index increment dn/dc is also needed which is accomplished by use of a differential refractometer. Another parameter which can be extracted from angular dependence of scattered intensities is form factor $P(q)$ verifying information about the size and shape of the aggregated particles. A nice work on the interpretation of shape and the mechanism of growth for aggregated dyestuffs is

provided by Michels et al in 2013 [55,56] who studied the aggregation of azo-dyestuff upon addition of Mg^{2+} ions. They applied two kinetic growth models, the INE model (irreversible nucleation elongation) and the Lomakin model [57] to describe the evolution of aggregate mass values with time. The application of simple INE model suggested a short period of nucleation for the dyestuff aggregation and the Lomakin model also gave an explanation for the origin of nuclei by generating them from micelles. Direct fitting of the scattering curves with the theoretical models and the correlation of size parameters with the respective mass data suggested a wormlike shape of the growing dyestuff aggregates. Dynamic light scattering (DLS) reveals the diffusion coefficient and from this a hydrodynamic radius of particles will be calculated. Finally it is possible to obtain the evolution of particle mass and size with time, thereby gaining information on the nucleation and growth by time resolved light scattering (TR-SLS/DLS).

1.3 Outline of the Thesis

The objective of this dissertation is to characterize the solution behavior of the acidic rainbow dyestuffs in the presence of different additives. Two main investigated characteristics are (i) the modification of rainbow dyestuff solubility in the presence of selected additives and (ii) the aggregation/precipitation of rainbow dyestuffs initiated by specific salts and hydrochloric acid. Morphology and aggregation mechanism will be discussed at the end. The introduction chapter will be followed by four more chapters as bellow:

Chapter 2 provides the theoretical background of the present work. Ultraviolet visible spectroscopy is introduced as a helpful method for the quantitative determination of solubility limit and molar extinction coefficient of the different dyestuff samples. This is complemented by a review on the principle of UV-vis spectroscopy and presenting a detailed sketch of device. Determination of the solubility limit by use of Beer-Lambert law is discussed. The chapter is continued by introducing light scattering as a powerful tool for non-destructive characterization of the dyestuff samples. The physical principles of light scattering are explained and a comparison between two different instruments of single-angle and multi-angle detectors is provided. Determination of the refractive index increment via a differential refractometer is explained and corresponding physical principles are illustrated. The chapter is closed by describing the material and methods which are used in preparation of the samples for UV-vis spectroscopy and light scattering measurements.

Chapter 3 deals with experimental UV-vis data. The effect of benzyl alcohol and isopropanol on the solubility of dyestuffs in aqueous solution is investigated by use of UV-vis spectroscopy. Furthermore the impact of different cations and anions of Hoffmeister series on the solubility of acidic dyestuffs is evaluated.

Chapter 4 studies the aggregation of dyestuff triggered by adding $CaCl_2$ and HCl . The light scattering experiments are performed to investigate the aggregation of dyestuff. Time-resolved static and dynamic light scatterings provide insight into the process of aggregation/particle formation thereby an estimation of the growth mechanism of the rainbow dyestuffs. Finally the shape and structure of created particles are discussed.

Chapter 5 concludes this thesis by summarizing the findings of this work. Based on the questions arising from the discussed results a perspective on the future work is developed.

In the Appendix complementary measurements of UV-vis spectroscopy including the molar extinction coefficients and absorbance spectra are given. Furthermore the mathematical details related to the light scattering measurements are presented.

Methods and Instruments

2.1 UV-vis spectroscopy

When light shines on a sample, two kinds of interactions may be observed: the light is scattered or absorbed by the sample molecules. The later interaction constitutes the foundation of UV-vis absorption spectroscopy in which the molecules are raised to a higher energy state and the light intensity in the corresponding range of wavelengths is decreased due to the absorption. The difference between the new energy level and the former one is described by Bohr-Einstein relationship [58, 59].

$$\Delta E = E_2 - E_1 = h\nu \quad (2.1)$$

Considering I_0 and I as the incident and transmitted beams respectively, the absorbance A is defined as:

$$A = \log\left(\frac{I_0}{I}\right) \quad (2.2)$$

It is preferred to express the absorbance instead of transmittance because it is directly proportional to the concentration of dyestuff c and path length L as:

$$A = c\varepsilon L \quad (2.3)$$

where the parameter ε is known as the molar extinction coefficient. The Equation 2.3 is called *Beer – Lambert* law where ε is a measure of the amount of light absorbed per unit concentration and unit length. A simplified scheme of UV-vis spectrometer is depicted in Figure 2.1. In a Lambda 19 (Perkin Elmer) spectrophotometer, working

in the wavelength range of $300 \leq \lambda \leq 800$ nm, a tungsten-halogen lamp is installed as light source for visible range and a deuterium lamp is used for the UV spectrum. The wavelength of incident beam is specified by a monochromator. After interaction of the incident beam with any sample in the cuvette, the output beam is collected by a detector which is connected to a computer.

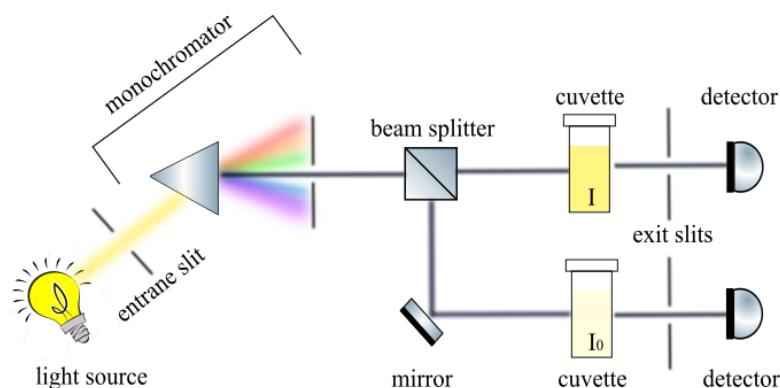


Figure 2.1. Scheme of UV-vis spectrometer

For the UV/VIS-measurements the solutions were filled into quartz glass 106-QS cuvettes (Hellma Analytics, Mehlheim-Germany) with different path lengths (0.1mm, 1mm and 2mm) depends on the concentration of the solutions. Filtration was done through a syringe filter (Chromafil filter; Xtra H-PTFE-20/25; MN GmbH, Germany) with a pore size of $0.2 \mu\text{m}$ to remove the precipitated dyestuffs from the solution. Each measurement is corrected with the absorbance of corresponding solvent. The absorbance data are recorded by the program PerkinElmer WinLab.

2.1.1 Determination of the solubility limit

Based on the nature of dyestuffs and the applied solvents, two different situations are observed: (i) The measured absorbance values satisfy the Beer-Lambert law following a linear increase of absorbance (red line in Figure 2.2-a) by enhancement of the dyestuff concentration up to a certain limit. Above this limit, a deviation from Beer-Lambert law is observed directly leading to an equilibrium in which the increasing of concentration does not change the absorbance values anymore (blue line in Figure 2.2-a). This state is defined as saturated state and the corresponding concentration is known as c_{sat} calculated from the intersection of blue and red lines. Consequently, the uncertainty of finding the intersection is considered as the uncertainty of the c_{sat} . (ii) Deviation from Beer-Lambert law happens through a sharp decay of the absorbance with increasing the dyestuff concentration so that a meta-stable state can be assumed (Figure 2.2-b). In such systems, a maximum solubility c_{max} can be determined as the last measured concentration which obeys the linear trend of the Lambert-Beer law. The uncertainty

of c_{max} is defined as the difference between c_{max} and the next measured concentration. Finally at high enough concentrations a saturated state is observed where the absorbance values remain almost constant and independent of the dyestuff concentration. This establishes a plateau line for the absorbance values. The c_{sat} and its uncertainty is determined as was explained before.

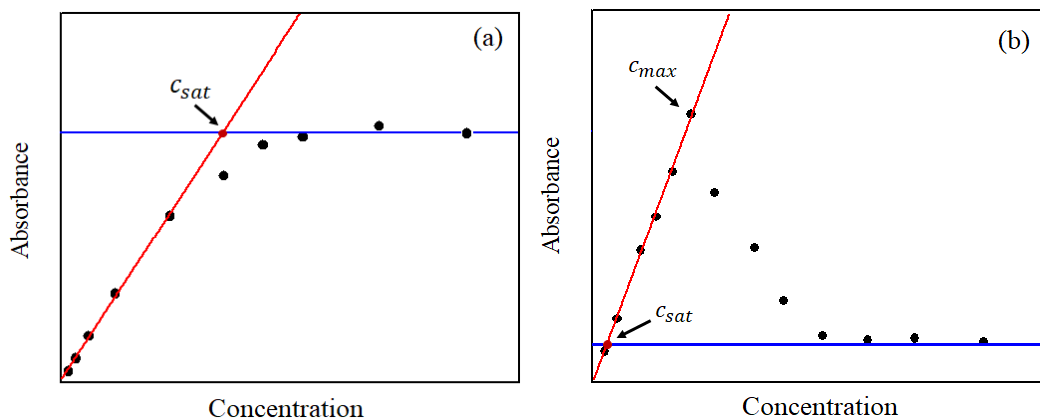


Figure 2.2. Schematic explanation of how to calculate the solubility limit and related uncertainty in different systems.

2.2 Light Scattering

The sky is blue! This is caused by the interaction of light and the atmospheric particles which scatter blue light stronger than the red [60–63]. This interesting behavior of light as an electromagnetic wave is the fundamental concept of light scattering. When the electromagnetic wave interacts with particles a dipole moment is induced which in turn emits a secondary electromagnetic wave with the same wavelength and frequency as the primary wave. The intensity of scattered waves is influenced by the mass, size and form of the scattering particles in the sample which is desired to be analyzed. Also the internal mobilities of the particles have an effect on the properties of scattered light. A brief discussion about the theoretical background and mathematics of the light scattering method is provided here. Detailed information about the light scattering and its immense influence on chemistry, biology and physics can be found in the textbooks [64–74].

2.2.1 Static Light Scattering (SLS)

In a static light scattering measurement, intensity of the scattered light expressed as Rayleigh ratio ΔR_θ is measured at different scattering angles θ

$$\Delta R_\theta = R_{\theta, std} \frac{r_{\theta, solution} - r_{\theta, solvent}}{r_{\theta, std}} \quad (2.4)$$

with $R_{\theta, std}$ the absolute scattering intensity of the standard toluene in units of reciprocal length, $r_{\theta, std}$ the measured scattering intensity of the standard toluene, $r_{\theta, solution}$ the measured scattering intensity of the solution and $r_{\theta, solvent}$ the scattering intensity of the solvent. It is convenient to represent the Rayleigh ratio as a function of the absolute value of the scattering vector $|\vec{q}|$, which is defined as the difference between the wave vector of the primary beam \vec{k}_i and scattered beam \vec{k}_s :

$$|\vec{q}| = |\vec{k}_s - \vec{k}_i| = \frac{4\pi n_{solvent}}{\lambda_i} \sin\left(\frac{\theta}{2}\right) \quad (2.5)$$

with $n_{solvent}$ the refractive index of the solvent, λ_i the wavelength of primary or incident beam and θ the scattering angle.

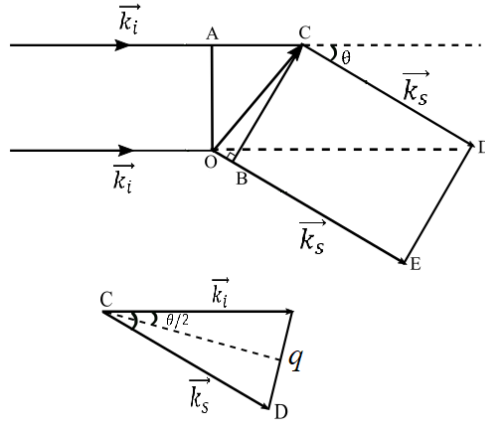


Figure 2.3. The beam is scattered at the angle θ from two different centers of the sample [71].

Different methods can be used to determine the particle size and mass from the angular dependent scattering intensities. During this work, two approximations have been applied the Zimm method [75] and the Guinier approximation [76]. From a Zimm-plot the molar mass M_w , the radius of gyration R_g and the second virial coefficient A_2 from dilute solutions of scattering particles are determined as follows:

$$\frac{Kc}{\Delta R_\theta} = \frac{1}{M_w} + \frac{(R_g \cdot q)^2}{3M_w} + 2A_2c \quad (2.6)$$

where c in g/L is the concentration of dissolved particles and K is the contrast factor which includes the parameters Avogadro's number N_A , primary beam wavelength λ_i , refractive index of the standard toluene n_{tol} and the refractive index increment $\frac{dn}{dc}$ of the solute in the solvent as:

$$K = \frac{4\pi^2 n_{tol}^2}{N_A \lambda_i^2} \left(\frac{dn}{dc} \right)^2 \quad (2.7)$$

The Zimm method for evaluation of the scattering intensities requires the extrapolation to infinite dilution ($c \rightarrow 0$) and to $q^2 \rightarrow 0$ in order to determine molecular weight M_w and the radius of gyration R_g . It must be mentioned that in the regime of sufficiently small angles, the condition of $qR_g < 1$ is satisfied as a red laser with ($\lambda = 633 \text{ nm}$) has been used in this work.

The second approach is a Guinier approximation determining the weight-averaged molar mass and the radius of gyration according to Equation 2.8 where the virial coefficient was neglected.

$$\ln \frac{Kc}{\Delta R_\theta} = \ln \frac{1}{M_w} + \frac{(R_g \cdot q)^2}{3} \quad (2.8)$$

As the scattered intensity contains information about intra-particle interferences, it provides information about the particle structure. The dependence of the scattered intensity on the size and the shape of particles is usually described by the form factor $P(q)$.

$$P(\vec{q}) \equiv \frac{I(\vec{q})}{I(0)} \quad (2.9)$$

$P(q)$ approaches 1 for the $q \rightarrow 0$. For static light scattering a particle size of at least 100 nm is necessary to discriminate significantly among different particle shapes.

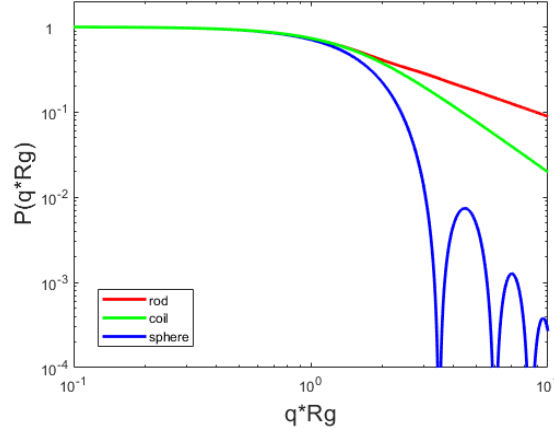


Figure 2.4. Form factor for a rod, a Gaussian coil and a hard sphere [77–79].

2.2.2 Dynamic Light Scattering (DLS)

When the light hits a moving particle, a Doppler broadening emerges due to the Brownian motion which changes the wavelength of primary beam. By collecting the intensity fluctuations, it is possible to compute the sphere size distribution and give a description of the particle's motion in the solution obtaining its diffusion coefficient by use of the autocorrelation function. To this purpose the detector is fixed at a certain angle recording a superposition of the intensities scattered from all particles in the scattering volume. The intensity fluctuations in time is expressed as time-dependent autocorrelation function $g^2(\tau)$ explaining why the dynamic light scattering is also known as photon correlation spectroscopy. The measurement over time t_{tot} is divided into time intervals Δt . The scattering intensity measured at any time t is multiplied by the intensity measured after a certain lag-time $\tau = n \cdot \Delta t$.

This procedure is repeated until a sufficient number of pairs of $I(t)$ and $I(t + \tau)$ is obtained and averaged. The time dependent autocorrelation function is given as the sum of all intensity products divided by the total number of all products. As the total measurement time t_{tot} is very large in comparison to the time interval t the sum can be described by the integral. The same routine is applied for different values of n which adopts only natural numbers. Obviously by increasing the lag-time the correlation of the intensities decreases.

$$\langle I(t) \cdot I(t + \tau) \rangle = \frac{1}{t_{tot}} \int_0^{t_{tot}} I(t) \cdot I(t + \tau) dt \quad (2.10)$$

and the normalized intensity-time autocorrelation function $g^{(2)}(\tau)$ can be resulted from

the division of Equation 2.10 by $\langle I(t) \rangle^2$:

$$g^{(2)}(\tau) = \frac{\langle I(t) \cdot I(t + \tau) \rangle}{\langle I(t) \rangle^2} \quad (2.11)$$

It is worthy to mention that the averaged value of the scattering intensity $\langle I(t) \rangle$ corresponds to ΔR_θ in static light scattering. For larger particles $g^{(2)}(\tau)$ decays slow because the particles move slower so they do not have a chance to move to a great extent from the initial state that they were in. In other words, they have the smaller diffusion coefficient. For small particles the correlation decays faster as particles have larger diffusion coefficient. The Siegert equation relates the second order autocorrelation function $g^{(2)}(\tau)$ with the first order or electric field-time autocorrelation function $g^{(1)}(\tau)$ as follows [68, 80]:

$$g^{(2)}(\tau) = 1 + \beta \cdot [g^{(1)}(\tau)]^2 \quad ; \quad g^{(1)}(\tau) = \frac{\langle E^*(t) \cdot E(t + \tau) \rangle}{\langle |E(t)|^2 \rangle} \quad (2.12)$$

where the parameter β is a spatial coherence factor. It is approximately equal to the inverse of the number of speckles from which light is collected [81].

$g^{(1)}(\tau)$ can be described by a single exponential decay as Equation 2.13 if the scatterers are monodispers particles.

$$g^{(1)}(\tau) = e^{-\Gamma\tau} \quad (2.13)$$

where the time constant Γ describes the inverse time required by the particles to cover a mean squared displacement of q^{-2} . It is connected to the translational diffusion coefficient via:

$$\Gamma = Dq^2. \quad (2.14)$$

In the case of polydispers particles a superposition of exponential decays is considered and a sum of exponential functions can describe the first order autocorrelation function.

$$g^{(1)}(\tau) = \sum_{i=1}^n c_i e^{-\Gamma_i \tau} \quad (2.15)$$

where Γ_i is the time constant and c_i the weighting factor of species i within the respective total ensemble.

A cumulant method [74] is applied to fit the correlation functions. To this end, the logarithm of the field-time-autocorrelation function is rewritten as a series

$$\ln[g^{(1)}(\tau)] = K_0 - K_1\tau + \frac{1}{2!}K_2\tau^2 - \frac{1}{3!}K_3\tau^3 + \dots \quad (2.16)$$

where K_0 is the signal to noise ratio and K_1 is the z-averaged time constant $\langle \Gamma \rangle$, which is related to the z-averaged diffusion coefficient according to

$$K_1 = \langle \Gamma \rangle = \langle D_z \cdot q^2 \rangle \quad (2.17)$$

The coefficient K_2 expresses the variance of the time constant being a measure for the polydispersity.

$$K_2 = \langle (\Gamma - \langle \Gamma \rangle)^2 \rangle \quad (2.18)$$

From the extrapolation of apparent diffusion coefficient D_z to the zero concentration $c \rightarrow 0$ and zero angle q^2 , D_0 can be obtained as

$$D_z = D_0(1 + q^2 R_g^2 \alpha + k_d c) \quad (2.19)$$

where α is a dimensionless parameter which depends on the shape of the particles and k_d is a parameter accounting for the concentration dependence of D_z . The hydrodynamic radius can be obtained by the Stokes-Einstein equation

$$R_h = \frac{k_B T}{6\pi\eta} \frac{1}{D_0} \quad (2.20)$$

with k_B the Boltzmann constant, T the temperature and η the viscosity of solvent.

Experimental results for the ratio R_g/R_h are compared with the anticipated values for various polymer structures which are listed in Table 2.1 [71]. This shape-sensitive factor is known as ρ -factor and in general, decreases by increasing the compactness. Therefore ρ -factor can be used as a tool to distinguish between spheres, rods, and fractal structures like unperturbed polymer coils. ρ parameter assumes a value between 1.5 and 1.8 for a polymer coil or a comparable fractal [82], $\rho = \sqrt{3/5} \cong 0.77$ is expected for a compact sphere [65] and $\rho \geq 2$ is assumed for rod-like structures [83,84]. Polydispersity also increases the ρ -ratio so that the randomly branched polymers in good solvent have

large values of $\rho \cong 2$ (near their gel point) [74].

It must be noted that experimental values of ρ for polymer coils are always smaller than the theoretical estimates, indicating that the hydrodynamic radius is underestimated. For example in the case of mono-disperse linear polymer chains under θ -conditions, the value of $\rho = 1.5$ predicted by theory is 17.5% larger than the experimental values [85].

$$\rho = \frac{R_g}{R_h} \quad (2.21)$$

Table 2.1. Ratio of radius of gyration and hydrodynamic radius for different polymer structures [66, 71].

Polymer structure	Solvent	ρ Zimm theory	ρ experiment
Randomly branched	Good	–	2.0
Linear monodisperse	Good	1.6	1.5
Randomly branched	θ	1.7	–
Linear $M_w/M_n = 2$	θ	1.7	–
Linear monodisperse	θ	1.5	1.3
3-Arm star	θ	1.4	1.2
4-Arm star	θ	1.3	1.05
12-Arm star	θ	1.17	0.93
270-Arm star	θ	1.08	0.77
Hard sphere	–	0.77	0.77

2.2.3 Scaling laws

A correlation between particle mass M_w and particle size R_g or R_h provides helpful information on the geometry and shape of the growing particles [86].

$$R_g \propto M_w^\alpha \quad (2.22)$$

where the shape sensitive exponent α adopts characteristic values if the varying R_g and M_w refer to self-similar structures: $\frac{1}{3}$ for compact, spherical particles, $\frac{1}{2}$ for Gaussian polymer coils, and 1 for infinitely thin rods.

The α value obtained from M_w and R_g by time-resolved SLS includes information not only about the structure of the growing particles but also about the mechanism of

growth of those particles. In a step-growth process where any particle can agglomerate with any other, the exponents satisfy the topology as it is described.

In case of monomer addition process, one has to be careful in using data from light scattering in Equation (2.22). Since in this mechanism the monomers are only added at active sites on the growing particles, data recordings are performed on an ensemble including two species: non-consumed monomers and particles. In this case, the exponent α is just half of the exponent in Equation (2.22) if R_g and M_w are determined from intercepts in the Zimm or Guinier representations [87,88].

$$R_g^2 \propto M_w^\alpha \quad (2.23)$$

Knowledge of the monomer concentration at the end of light scattering measurement can be used to re-evaluate the mass concentration of the aggregated particles so a better decision can be made on determination of the aggregation process.

The evolution of weight-averaged molar mass M_w and the z-averaged squared radius of gyration R_g are suitable to be interpreted by kinetic models. In our work two limiting models of growth shall be explained. Independent of the model, the number of constituent particles at the onset of process is fixed at n_0 with a number density of ν_0 [87]. The size of these constituent particles is given by the outer sphere radius R_0 . Any k-mer, formed from k constituent particles, has a volume of V_k with:

$$V_k = k \left(\frac{4\pi R_0^3}{3} \right) \quad (2.24)$$

and a radius of gyration of:

$$R_{g,k} = \sqrt{(3/5) \left(\frac{3V_k}{4\pi} \right)^{2/3}} \quad (2.25)$$

(i) Particle growth occurs via coagulation of particles. A good estimation of the time dependent evolution of particle size and particle size distribution is provided by Marian von Smoluchowski [89] who could solve an approximate version of the respective differential equations. The process is characterized by a characteristic coagulation time τ and a time dependent number density of k-meric particles ν_k

$$\nu_k = \nu_0 \frac{(t/\tau)^{k-1}}{(1 + t/\tau)^{k+1}} \quad ; \quad k = 1, 2, 3, \dots \quad (2.26)$$

where $k = 1$ yields $\nu_1 = \nu_0$ at $t = 0$. The z-averaged squared radius of gyration is:

$$R_g^2 = \frac{\sum_{k=1}^x R_{g,k}^2 V_k^2 \nu_k(t)}{\sum_{k=1}^x V_k^2 \nu_k(t)} \quad (2.27)$$

Weight averaged mass values can be easily calculated from averaged volume V_w by From $M_w = \rho \cdot V_w$:

$$V_w = \frac{\sum_{k=1}^x V_k^2 \nu_k(t)}{\sum_{k=1}^x V_k \nu_k(t)} \quad (2.28)$$

(ii) Monomer-addition growth, is the second limiting model. In this model, the monomer fraction decreases while the polymer fraction increases, forming a bimodal system with changing amounts of the two fractions. Two assumptions can be considered: (a) the nucleation rate is slower than the growth; (b) the nucleation is faster than the growth.

The weight averaged molar mass of growing polymers is:

$$M_w = \frac{\sum_{k=1} n_k k^2 M_0^2}{\sum_{k=1} n_k k M_0} \quad (2.29)$$

which has to be compared with a z-averaged squared radius of gyration:

$$R_g^2 = \frac{\sum_{k=1} n_k k^2 M_0^2 R_{g,k}^2}{\sum_{k=1} n_k k^2 M_0^2} \quad (2.30)$$

The limiting case of fast nucleation and monomer addition slow compared to the nucleation, results in a monodisperse polymers sample. For these monodisperse polymers only two species exist corresponding to monomers ($k = 1$) and polymers with a degree

of polymerization k .

$$M_w = \frac{(n_0 - k)M_0^2 + M_0^2 k^2}{n_0 M_0} \quad (2.31)$$

$$R_g^2 = \frac{(n_0 - k)M_0^2 R_{g,0}^2 + M_0^2 k^2 R_{g,k}^2}{(n_0 - k)M_0^2 + M_0^2 k^2} \quad (2.32)$$

where the k is degree of polymerization, M_0 is the mass of a monomer, and $n_0 - k$ is the non-consumed monomers. As we considered here the case of monodisperse polymers, the weight fraction of k -mers is equal to k/n_0 .

Figure 2.5 shows the correlation of R_g versus M_w for the particles which grow according to the (i) coagulation mechanism and (ii-a) monomer addition. $\rho = 1 \text{ g/mL}$ is considered to yield the mass. The monomer in both cases is the sphere with volume of $4\pi 10^3 \text{ nm}^3/3$.

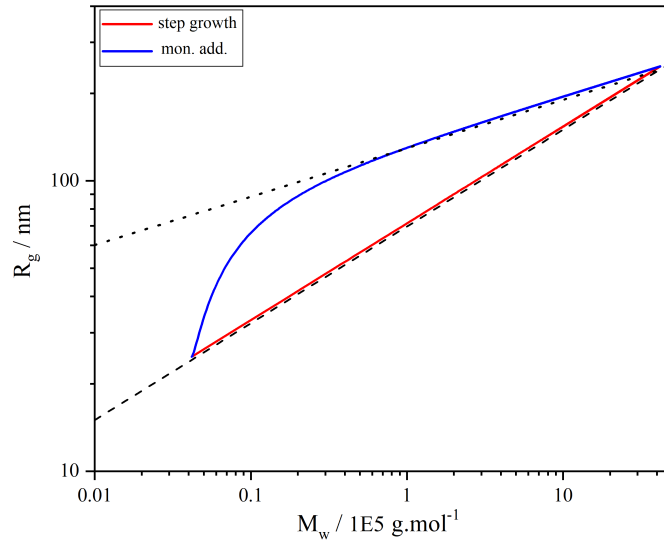


Figure 2.5. Correlation of R_g with M_w for a step growth and a monomer addition process. The dotted line indicates a slope of $1/6$ and dashed line $1/3$.

2.3 Determination of the Refractive Index Increment

As mentioned in section 2.2.1, the calculation of all molecular parameters from the light scattering is dependent on knowing the sample refractive index increment dn/dc . The refractive index increment dn/dc of the solutions are measured by a differential refractometer provided by SLS-Systemtechnik. The light source is a He-Ne laser with the wavelength of $635nm$. A two-chamber cuvette containing the solvent in one side and the solution on the other side is subjected to the laser beam. Separation of the solvent and solution in two-chambers cuvette is done by a thin glass plate positioned diagonally at 45° . Advantage of this optical design in comparison to other types of refractometers is that only the difference of the refractive indices influences the deflection. Since the refractive index of solvent leads to a basic deflection, the detection unit of other refractometers have to cover a broader angle regime which results in a lower resolution in common refractometers. Even a small change in temperature can cause a considerable impact on the refractive indices so a precise temperature control of the cuvette is required.

The measurement is started with two reference measurements: the first one denoted as zero-measurement is a measurement of the free beam path, without cuvette determining an absolute reference point for the linear Δn . Such a highly reproducible measurement can be used to check the measured data for a potential signal shift. The second reference measurement denoted as ref-measurement is a measurement in which the laser beam is guided into the cuvette filled with solvent in both chambers. The ref-measurement provides an offset for the applied setup. Since an inverse setup (rotation of the cuvette by 180°) is used to produce additional data points, the ref-measurement must be performed for both the regular and the inverse setup as the offset of the cuvette can be different for the two different cuvette orientations. At the end both offset values are taken into the calculation to align the positive and the negative deflections. The interior design of a refractometer is shown in Figure 2.6 consisting of three main sections: the cuvette holder, the detection unit and the computer which receive the intensity signal after projection onto a CCD camera [90].

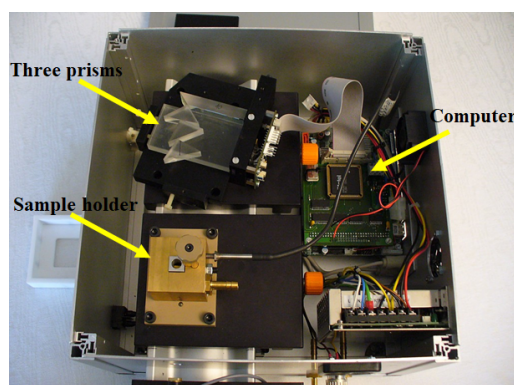


Figure 2.6. The interior design of a differential refractometer of SLS-Systemtechnik [91].

2.3.1 Refractive index increment of yellow and red dyestuffs in the applied solvents

As will be explained in 2.6, PL1Cl and PL2P are two main solvents in this work which are considered to dissolve the acidic dyestuffs. The dn/dc of yellow dyestuff in PL1Cl and red dyestuff in PL2P at room temperature has been determined to $0.4293 \times 10^{-3} L/g$ and $0.6905 \times 10^{-3} L/g$ respectively. The value of dn/dc for both dyestuffs is also measured in a third solvent PL1OH which is shown in Figure 2.7. This figure displays the measured differences in the refractive indices of solvent and solution as a function of the dyestuffs concentration. Values of dn/dc for yellow and red dyestuffs in different solvents are listed in Table 2.2.

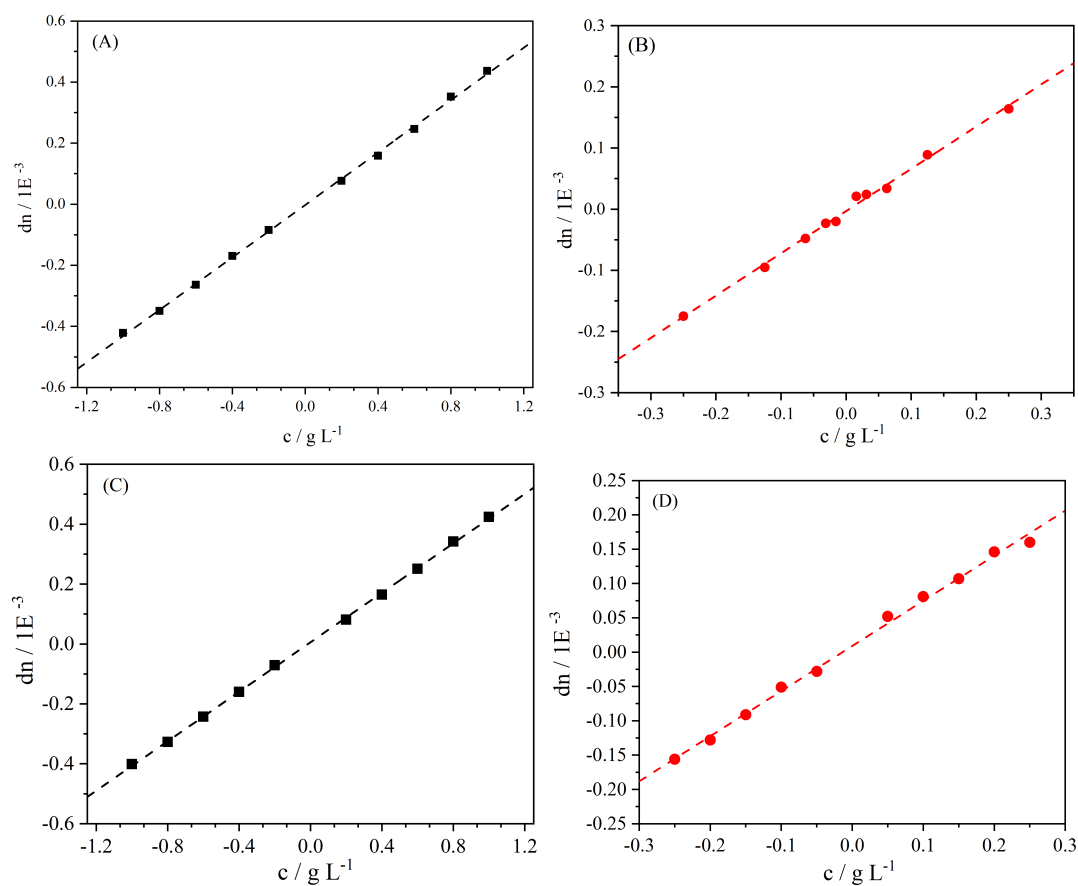


Figure 2.7. Refraction of the (A) yellow dyestuff in PL1Cl, (B) red dyestuff in PL2P, (C) yellow dyestuff in PL1OH and (D) red dyestuff in PL1OH as a function of the concentration. The measurements are done at room temperature ($\theta = 25^\circ C$).

Table 2.2. Values of dn/dc in $mL.g^{-1}$, measured for yellow and red dyestuffs in different solvents.

	PL1Cl	PL2P	PL1OH
yellow	0.42	—	0.41
red	—	0.69	0.66

2.4 Laser light scattering instruments

2.4.1 Single angle detection: ALV 5000E Compact Goniometer System

The instrument ALV-CGS 5000E (ALV-Laservertriebsgesellschaft, Langen) with a single detector was used to perform combined static and dynamic light scattering (SLS/DLS). Figure 2.8 illustrates the scheme of the device. The device is equipped with a He-Ne laser operating at $\lambda = 632.8\text{ nm}$ with a power of 100 mW . If the scattering intensity of the sample is too high for the detector then a beam attenuation can be done manually. The adjusted laser beam passes through a beam splitter. One part of the beam goes to a reference detector (monitor diode) and the other part focuses into the center of a goniometer. The goniometer includes a toluene bath as a liquid to match the refractive indices of bath and the glass (scattering cell). A sample holder is established to locate the scattering cell in the center of toluene bath. The beam is scattered by the sample, coupled into a waveguide via apertures and collected by the detector which is positioned at variable angles θ (with respect to the primary beam) around the toluene bath. The detector is connected to a computer to record the measured intensities. A thermostat keeps the temperature at $T = 25^\circ\text{C}$ during all measurements. The single angle device was used for samples that were stable or that show slow kinetics such that no significant changes occurred during a typical time required for the analysis of an angular dependent scattering curve.

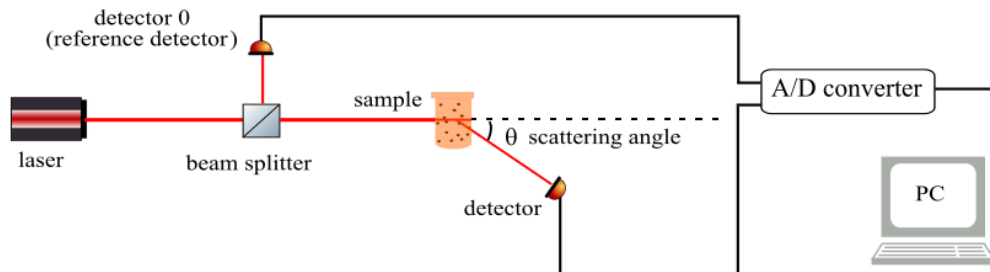


Figure 2.8. Sketch of a single-angle detection instrument. The intensity of scattered light is collected at variable angles θ sequentially and divided by the intensity of the incident light, which is measured by a reference detector.

2.4.2 Multi angle detection: ALV/CGS3/MD-8 Multi detection Laser Light Scattering System

Time resolved SLS and DLS experiments (TR-SLS/DLS) were carried out on an ALV CGS3/MD-8 Multi detection instrument (ALV Laservertriebsgesellschaft, Langen), which is equipped with eight detectors spaced 8° from each other. As is shown in Figure 2.9, the 8 detectors cover a wide range of angles ($20^\circ \leq \theta \leq 136^\circ$) and allow to record

the scattered light at 8 fixed different angles simultaneously. A He-Ne Laser with a wavelength of 632.8 nm and a power of 35 mW is used as a light source. In this device an automatic attenuation is possible via seven attenuator stages which is controlled by a general control unit (LSE). It checks every attenuation stage from high attenuation to full laser intensity. At each stage a user-defined limit of intensity allows the detector at smallest scattering angle θ to record the scattering intensity. Depending on the recorded intensity, the appropriate attenuation will be applied. The whole process of adjusting the primary beam via attenuator takes almost 8 seconds reducing the resolution of time-resolved scattering experiments. Although it may harm the detectors in case of strongly scattering particles, it is also possible to set the attenuation on a fixed value for the whole run of measurements. In this way 8 seconds are saved in each run optimizing the time resolution of time resolved measurements. The adjusted beam passes through a beam splitter. One part of the beam goes to a reference detector (monitor diode) and the other part focuses into the center of a goniometer where the bath is located. The bath is filled with toluene, as it matches the refractive index of glass (from the cuvette), in order to eliminate significant scattering effects from the interface glass-toluene. An external thermostat is implemented to control the temperature of the toluene bath inside the goniometer. A rotation unit is designed under the goniometer to drive the group of the detectors around the toluene bath covering the angular regime of $20^\circ \leq \theta \leq 136^\circ$. For each angle one lens and one aperture is inserted to guide the scattered light into the waveguides which are connected to Avalanche diode. The resulting signal from each Avalanche diode is correlated as a function of time.

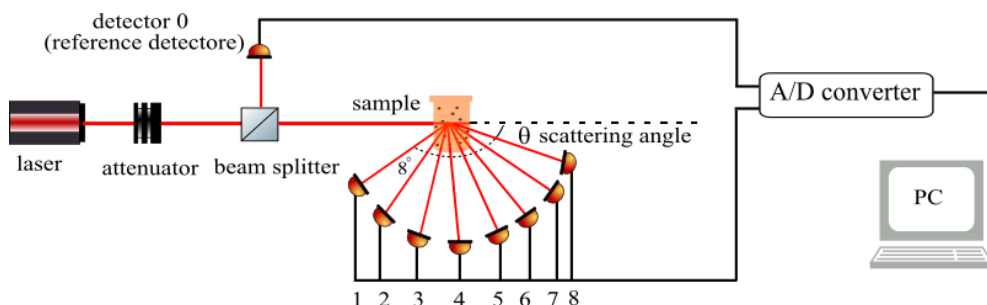


Figure 2.9. Sketch of a light scattering instrument with 8 detectors. The intensity of scattered light of each detector is measured simultaneously and divided by the intensity of incident light, which is measured by a reference detector.

It is worthy to note that the detector sensitivities must be corrected before performing a light scattering measurement. To measure the sensitivity of all 8 detectors it is needed to set the sensitivity of one detector (the smallest angle in our measurements) as 1 and the recorded scattering intensity of toluene from the other detectors has to be set in relation to the intensity of the reference detector. The values listed in 2.3 represent the

detector sensitivities calculated from the data measured by the ALV/CGS3/MD-8. The sensitivity values have to be checked periodically by a measurement.

Table 2.3. The measured detector sensitivities for all eight detectors (from low to high angle).

detector numbers	detector sensitivities
1	1.000
2	1.065
3	0.977
4	1.104
5	1.004
6	1.024
7	0.971
8	1.133

The main advantage of a multi-detector device is that it enables us to trace the particle growth due to the recording of light scattering data at eight angles simultaneously. The time resolved dynamic light scattering provides very important parameters like diffusion coefficient, the shape-sensitive factor ρ and a correlation function. This is very useful to evaluate the particle formation process. However it must be mentioned that the time resolution in DLS is smaller than SLS as it is limited by the correlation time. Although the detection of a whole scattering curve with a larger number of scattering angles at once is a great advantage, it may also reduce the quality of instrument alignment, as it is difficult to achieve the same degree of alignment for all detectors. In case of a single detector instrument a standard deviation of $\pm 1\%$ for the scattering intensity over the whole angle regime is achieved while this value for eight detector instrument lies around $\pm 5\%$ over the whole angular range.

2.4.3 Data evaluation

The measurement program generates two types of files. The first file contains all measurement points with relevant data such as the time (t), the averaged count rates (CR) and the laser intensity (I). In addition, a file is generated which contains the correlation functions of dynamic light scattering ($g^2(\tau)$) and progress of the count rate over time. Within the scope of this work, a suitable program to visualize the data, and to evaluate it routinely and appropriately is written on the basis of MATLAB by Benjamin Hämisch. In general, the program uses the laser intensity to check which standard and solvent values are required for the calculation according to Equation 2.6. These are then saved in a temporary matrix in order to generate the corresponding $Kc/\Delta R_\theta$ values. Then the temporary matrix is overwritten for the next data point.

In the next step, the scattering curves can be evaluated depending on the generated data. Various tools are available for this, which can be seen in Figure 2.10. The example is selected from the time-resolved measurement of 1 mmol.L^{-1} yellow dyestuff aggregated by addition of 2 ml CaCl_2 in the concentrations of 1.8 mmol.L^{-1} (the blue data points ▲ in Figure 4.3 at $t = 31\text{ min}$).

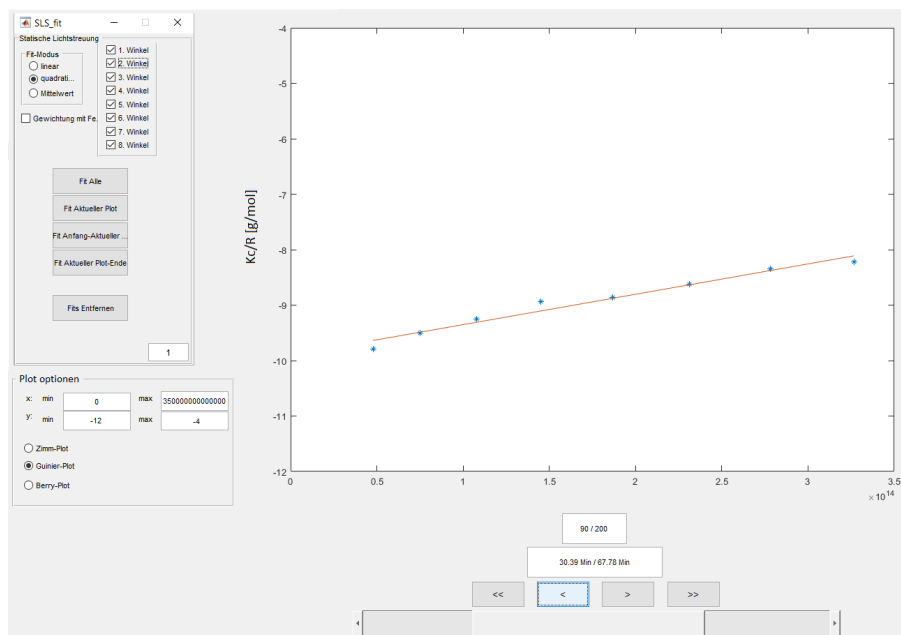


Figure 2.10. Overview of the fit program for static light scattering (quadratic fit on the Guinier plot).

Here we can set the type of plot for the fit procedure. The choices are Zimm, Berry and Guinier plot. A linear or quadratic fit can also be selected. In the present thesis all

data are fitted with a Guinier plot.

The work area for evaluating the dynamic light scattering data is shown in Figure 2.11. Different displaying modes can be selected on the left-hand side, including the intensity-time correlation function $g^{(2)} - 1$ or the field-time correlation function $g^{(1)}$. Furthermore, the count rate CR can be presented as well as the calculated diffusion coefficients versus q^2 . In this work, the fitting procedure is based on the cumulant method, with a flexible cutoff. Correlation functions of a desired data set can be displayed on the right side of the screen.

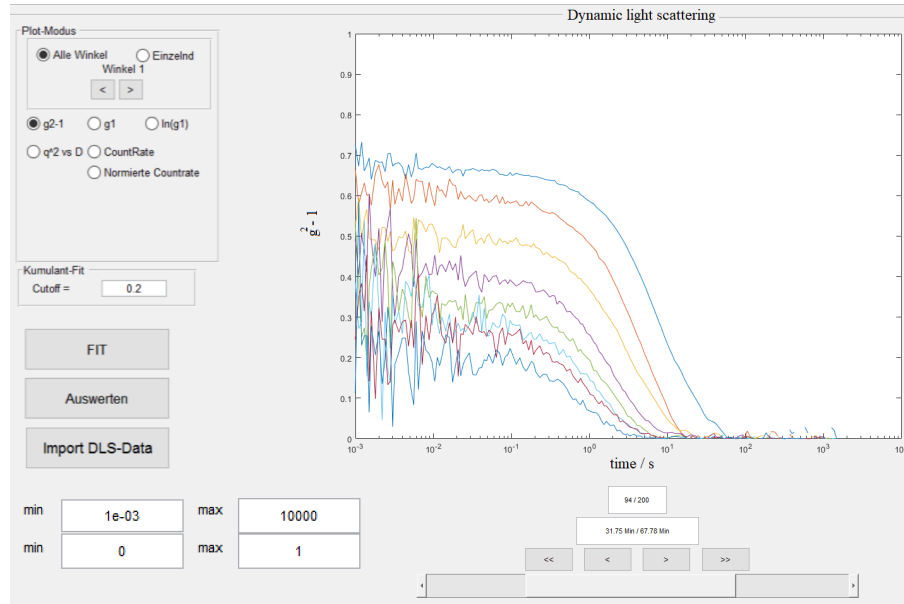


Figure 2.11. Overview of the fit program for dynamic light scattering, showing a set of intensity-time correlation function recorded at 8 angles.

To apply the cumulant method, the field-time correlation function $g^{(1)}$ is plotted versus time t as is displayed in Figure 2.12. The slope of each curve provides eight Γ values, thereby yielding the eight values of apparent diffusion coefficient D_z . In the last step, the D_z is plotted versus q^2 . Using a linear regression, D_z is extrapolated to $q^2 = 0$ and the diffusion coefficient D_0 is obtained. Finally hydrodynamic radius R_h can be calculated from Equation 2.20. If this entire process is not possible due to the data situation, for example if the measurement is very noisy, then the script skips the process (the corresponding run would be discarded). The calculated values of R_g , R_h and M_w can then exported from the program. More details are presented in Appendix I.

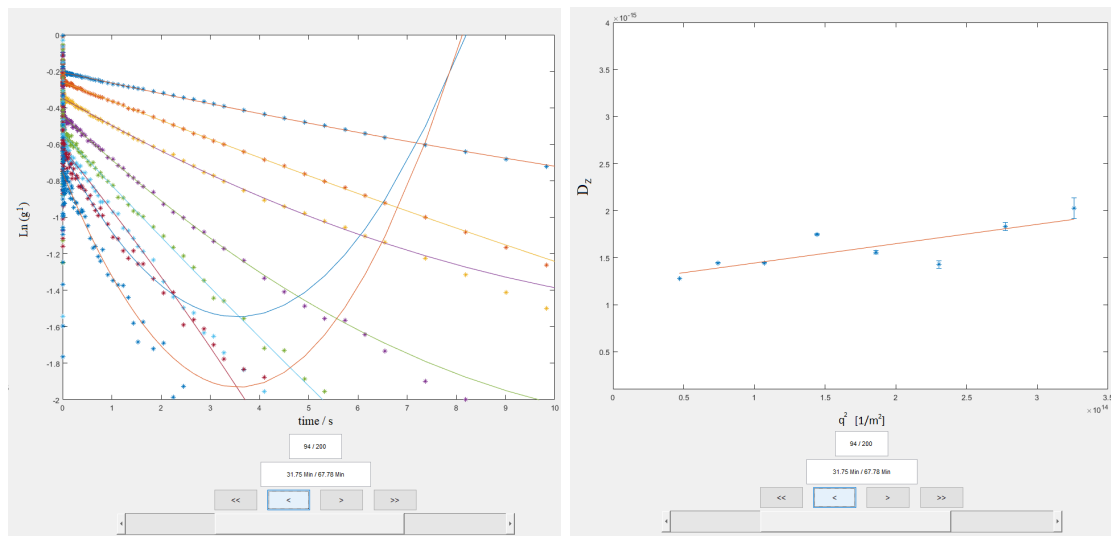


Figure 2.12. (A) Evaluation of the parameter Γ via fitting the plot of $g^{(1)}$ versus time t . (B) Extrapolation of D_z to $q^2 = 0$ via a linear fit (cumulant fit, single mode).

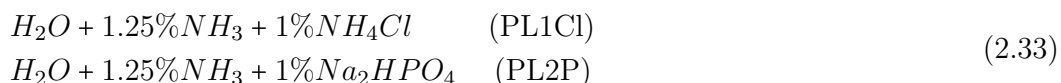
2.5 Materials

Three rainbow dyestuffs provided by KAO GmbH (Germany, Darmstadt) shall be analyzed: yellow (T44P2), red (FPK-245) and blue (FPK-145). The dyestuffs are used as received and stored at room temperature. All samples are prepared with high purity water (HPLC) provided by Merk company (Germany, Darmstadt). A standard ammonia solution with a concentration of 25% from the same company is used as a base in all solvents and stored at room temperature. Ammonium chloride with a purity of 99.9%, disodium phosphate with a purity of 99.8%, benzyl alcohol with a purity of 99.8%, isopropanol with a purity of $\geq 99.5\%$, guanidine sulphate with a purity of 99%, ammonium sulphate with a purity of 99.8%, sodium chloride with a purity of $\geq 99.5\%$, potassium chloride with a purity of $\geq 99.9\%$ and guanidinium chloride with a purity of 99% are obtained from Merk company (Germany, Darmstadt). Ammonium iodide with a purity of $\geq 99\%$ is obtained from Acros-Organics (USA, New Jersey). Sodium hydroxide NaOH (assay $\geq 99\%$) and hydrochloric acid HCl 1M (assay $\geq 99\%$) are purchased from Merk (Germany, Darmstadt). Calcium chloride hexahydrate $CaCl_2 \cdot 6H_2O$ (assay $\geq 99\%$) is purchased from Fluka (Buchs, Switzerland). The percentages are given by weight and all materials are stored at room temperature.

2.6 Sample Preparation

2.6.1 Preparation of UV-vis spectroscopy samples

The preparation of the UV-vis samples is performed in three steps. In a first step two solvents referred as reference solvents are prepared based on the following recipes:



In the second step *PL1Cl* solvent is altered by adding 2% benzyl alcohol, 2% isopropanol and 3% guanidinium sulphate. The resulting solvents are named as *PL1BA*, *PL1IP* and *PL1Gn* respectively. Subsequently *PL2P* solvent is altered by adding the same additives resulting in the new solvents *PL2BA*, *PL2IP* and *PL2Gn* respectively. The pH value of solvents are measured and summarized in Table 2.4.

Table 2.4. Measurements of the pH for PL1Cl, PL2P and the altered solvents by adding benzyl alcohol, isopropanol and guanidine sulphate.

solvent	pH	recipe
PL1Cl	10.20	$H_2O + 1.25\%NH_3 + 1\%NH_4Cl$
PL1BA	10.05	$H_2O + 1.25\%NH_3 + 1\%NH_4Cl + 2\%BA$
PL1IP	10.04	$H_2O + 1.25\%NH_3 + 1\%NH_4Cl + 2\%IP$
PL1Gn	10.18	$H_2O + 1.25\%NH_3 + 1\%NH_4Cl + 3\%GnCl$
PL1BAGn	10.09	$H_2O + 1.25\%NH_3 + 1\%NH_4Cl + 2\%BA + 3\%Gn$
PL2P	11.40	$H_2O + 1.25\%NH_3 + 1\%Na_2HPO_4$
PL2BA	11.40	$H_2O + 1.25\%NH_3 + 1\%Na_2HPO_4 + 2\%BA$
PL2IP	11.32	$H_2O + 1.25\%NH_3 + 1\%Na_2HPO_4 + 2\%IP$
PL2Gn	11.26	$H_2O + 1.25\%NH_3 + 1\%Na_2HPO_4 + 3\%GnCl$

To analyse the effect of different ions from the Hofmeister series, *PL1Cl* is altered in a second step via replacing the ammonium chloride by ammonium sulphate ($(NH_4)_2SO_4$), ammonium phosphate ($(NH_4)_2HPO_4$), ammonium iodide (NH_4I), potassium chloride (KCl), sodium chloride ($NaCl$) or guanidinium chloride ($GnCl$). The resulting solvents are named as *PL1SO4*, *PL1HPO4*, *PL1I*, *PL1K*, *PL1Na* and *PL3Gn* respectively. The pH of solvents are measured and summarized in Table 2.5. In some cases an appropriate acid was included to adjust the pH of solvent.

Table 2.5. Measurements of the pH for the solvents altered by the salts from Hofmeister series.

solvent	pH	recipe
PL1SO4	10.25	$H_2O + 1.25\%NH_3 + 1.23\%(NH_4)_2SO_4$
PL1I	10.21	$H_2O + 1.25\%NH_3 + 2.70\%NH_4I$
PL1HPO4	10.23	$H_2O + 1.25\%NH_3 + 0.82\%(NH_4)_2HPO_4 + 0.4\%H_3PO_4 (15.2M)$
PL3Gn	10.23	$H_2O + 1.25\%NH_3 + 1.78\%GnCl + 12\%HCl (1M)$
PL1Na	10.22	$H_2O + 1.25\%NH_3 + 1.09\%NaCl + 12\%HCl (1M)$
PL1K	10.21	$H_2O + 1.25\%NH_3 + 1.39\%KCl + 12\%HCl (1M)$

The three rainbow dyestuffs are dissolved in the 15 solvents mentioned above. For each solvent at least 10 different concentrations of dyestuff solution are prepared to provide a series of UV-vis measurements in each case. The samples are transferred

into the rectangular glass cuvettes (Hellma absorption cuvettes from Sigma-Aldrich) with different thicknesses selected in dependence of the concentration of dyestuff in the respective solution. In some cases the filtration through a syringe filter (Chromafil filter; Xtra H-PTFE-20/25; MN GmbH, Germany) with a pore size of $0.2\ \mu\text{m}$ is needed to remove the precipitated dyestuffs from the solution. To condition the filter, the first 2 mL of the solution is filtered and discarded. All experiments are performed at 25°C at two different ages of 4 hours, 24 hours and 6 days.

2.6.2 Preparation of Light Scattering Samples

Dyestuff and Ca^{2+} solutions for the light scattering experiments are prepared from a solvent based on the following recipe. The pH of solvent is measured as 11.95.



Direct Mixing of Component Solutions. Three solutions are required, the initial dyestuff solution, the aqueous Ca^{2+} solution and the hydrochloric acid HCl as the two initiators of the aggregation process. The yellow and red dyestuffs are dissolved in *PL1OH* solvent at different concentrations. Accordingly, calcium chloride is dissolved in the same solvent. The samples are transferred into the dust free cylindrical cuvettes (Hellma cuvettes from Sigma-Aldrich) with different diameters. The 18 mm diameter cuvettes are used for red solutions and the ones with 24 mm diameter are used for yellow dyestuff solutions. Removal of possible dust from the cuvettes is achieved by flushing them upside down with distilled acetone for 10 minutes. The filtration through a syringe filter (Chromafil filter; Xtra H-PTFE-20/25; MN GmbH, Germany) with a pore size of $0.2\ \mu\text{m}$ is needed to remove the dust from the solutions. To condition the filter, the first 2 mL of the solution is filtered and discarded. All experiments are performed at 25°C . Addition of the initiators (calcium chloride or HCl solution), as the second component solution, set time zero for the respective particle formation experiment. The time regime analyzed by multi-angle light scattering device depends on the sample. The measurement time on the single angle device depends on the intensity of scattered light from the sample.

Investigation of Dyestuff Solubility via UV-vis Spectroscopy

3.1 Solubility of Dyestuffs in Reference Solvents

We first analyzed the UV-vis absorbance of acidic rainbow dyestuffs dissolved in the reference solvents PL2P and PL1Cl. Both solvents are proposed by KAO (KAO GmbH, Germany, Darmstadt) as the first one has provided a good solubility for red dyestuff and the second one for yellow and blue dyestuff. The reason why the red dyestuff is considered to be dissolved in PL2P instead of PL1Cl is that the pH of PL1Cl is not high enough to dissolve this dyestuff. PL2P including the Na_2HPO_4 provides a higher pH resulting in a good solubility of red dyestuff.

The solutions were prepared and stored 4 hours at $25^{\circ}C$ before the first series of measurements were carried out. The measurements were repeated after 24 hours and 6 days to evaluate the stability of solutions. Results of UV-vis spectroscopy at different concentrations of yellow, blue and red dyestuff in PL1Cl and PL2P solvents are presented in Figures 3.1 - 3.6.

Figure 3.2-A represents the relation between the absorbance values of **yellow dyestuff** and concentration at the wavelength of $\lambda = 490\text{ nm}$, 4 hours after preparation of the solutions. The wavelength of $\lambda = 490\text{ nm}$ is selected as the absorbance of the solutions in wavelengths closer to the peak maximum go beyond the sensitivity of the UV-vis detector. An increase of the absorbance by increasing the concentration of dyestuff up to a certain limit in both solvents is observed. There is a linear relationship between

the absorbance values and concentrations indicating the Beer-Lambert law is satisfied and there is no aggregation at this range of concentrations. Above the solubility limit the solutions are in saturated state and a deviation from the Beer-Lambert law becomes visible which is a result of dyestuff precipitation or aggregation in the solutions. Obviously the solubility of yellow dyestuff in PL2P is higher than in PL1Cl.

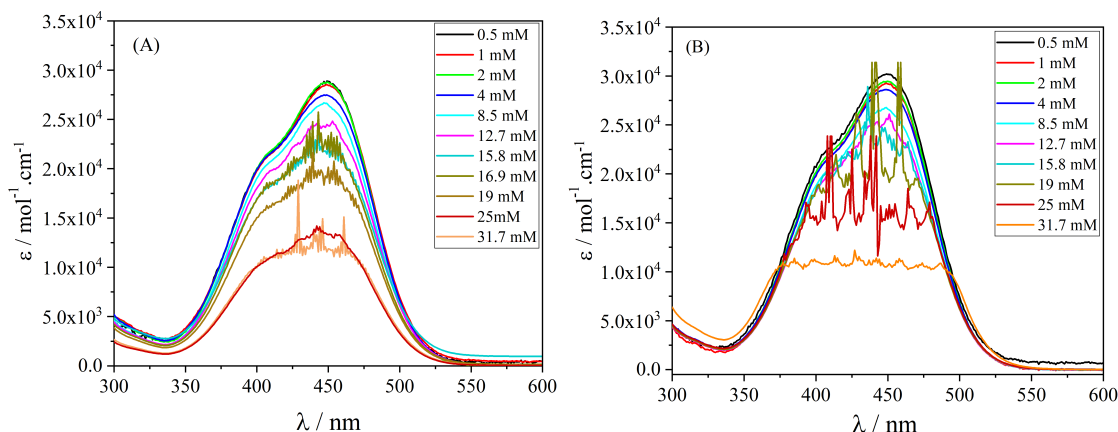


Figure 3.1. Molar extinction coefficients ϵ versus wavelength λ for different concentrations (in mmol/L) of **yellow dyestuff** in (A) PL1Cl and (B) PL2P solvent. The sensitivity limit close to the maximum is reached of 12.7 mM for both solvents.

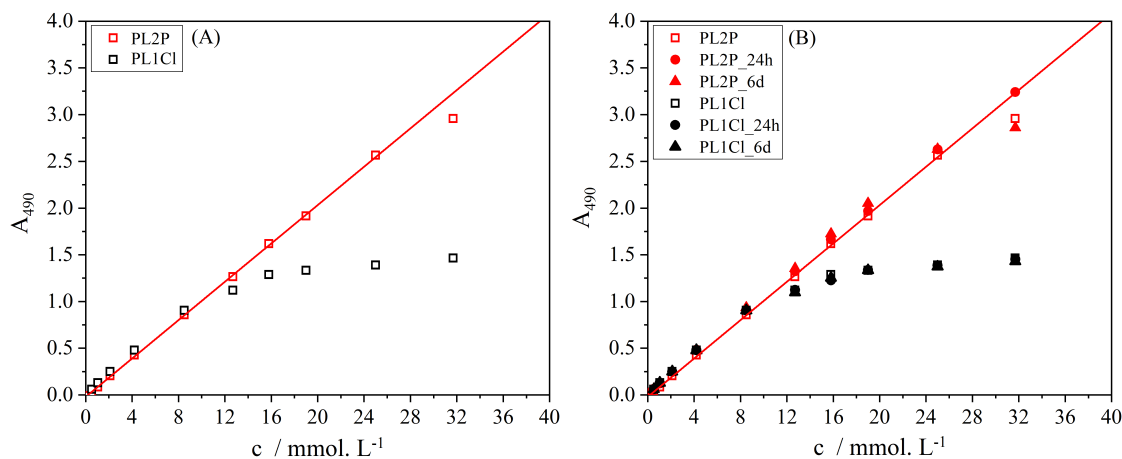


Figure 3.2. (A) Absorbance at $\lambda = 490 \text{ nm}$, 4 hours after dissolving the **yellow dyestuff** in PL1Cl \square and PL2P \square solvent. (B) Verification of solution stability with absorbance values measured at three different ages of the solutions in both PL1Cl and PL2P (\square 4h, \bullet 24h and \blacktriangle 6days).

The stability of solutions are investigated in Figure 3.2-B. Absorbance values are mea-

sured at three different ages of the solutions and show a perfect overlay even 6 days after the first measurement. It can be concluded that yellow dyestuff in both solvents is stable.

Results of UV-vis spectroscopy at different concentrations of **blue dyestuff** at the age of 4 hours which are presented in Figure 3.3. The absorbance in PL1Cl is enhancing by increasing the concentration of dyestuff up to a certain limit ($c_{max} = 0.68\text{ mM}$) and then it drops and solutions in saturated state reveal the solubility of $c_{sat} = 0.14\text{ mM}$ implying a meta-stable state in PL1Cl solvent. Solubility of blue dyestuff in PL2P is significantly higher than PL1Cl. Absorbance values in PL2P show a deviation from Lambert-Beer law at the concentrations higher than 8.1 mM . It can be interpreted from the plot that there is no c_{sat} in the measured concentration range but it might be found in higher concentration range.

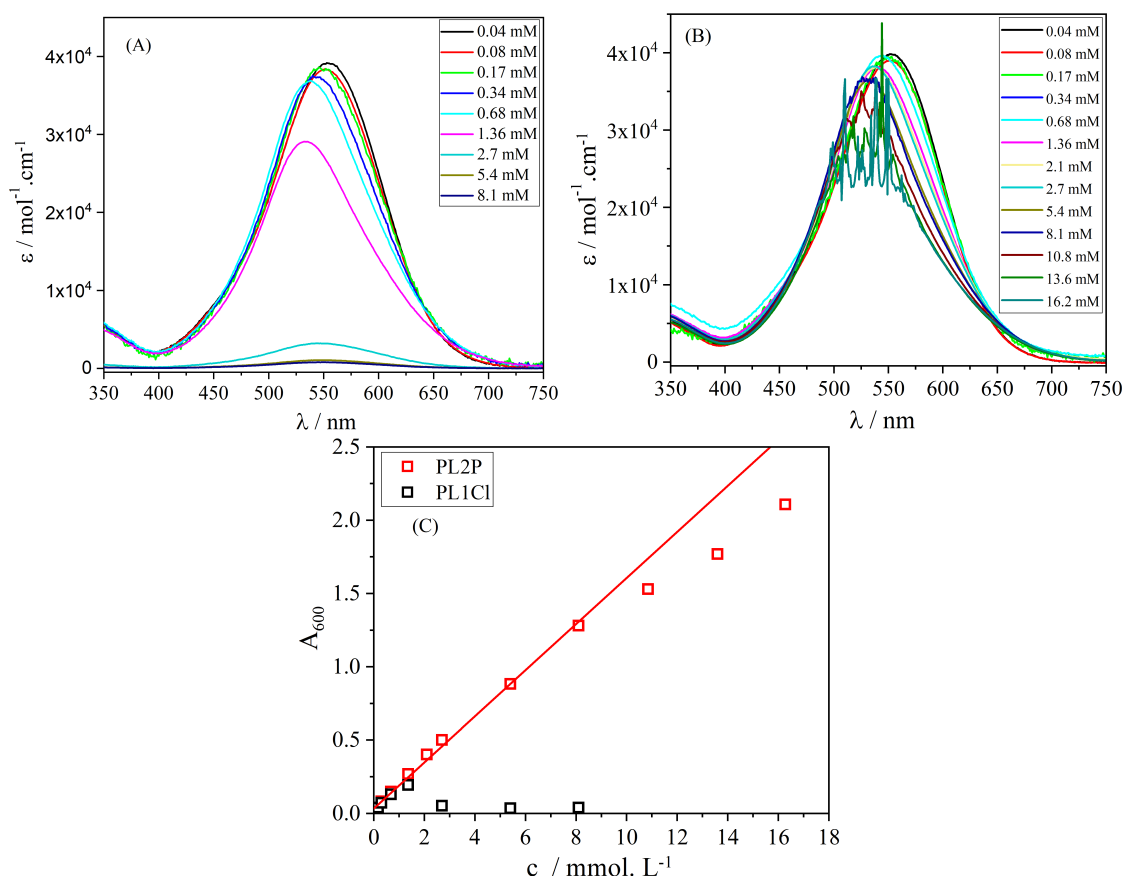


Figure 3.3. Molar extinction coefficients ϵ versus wavelength λ for different concentrations (in mmol/L) of **blue dyestuff** in (A) PL1Cl and (B) PL2P solvent at the age of 4 hours. (C) Verification of solution stability at $\lambda = 600\text{ nm}$ for blue dyestuff in PL1Cl \square and PL2P \square solvent at the age of 4 hours.

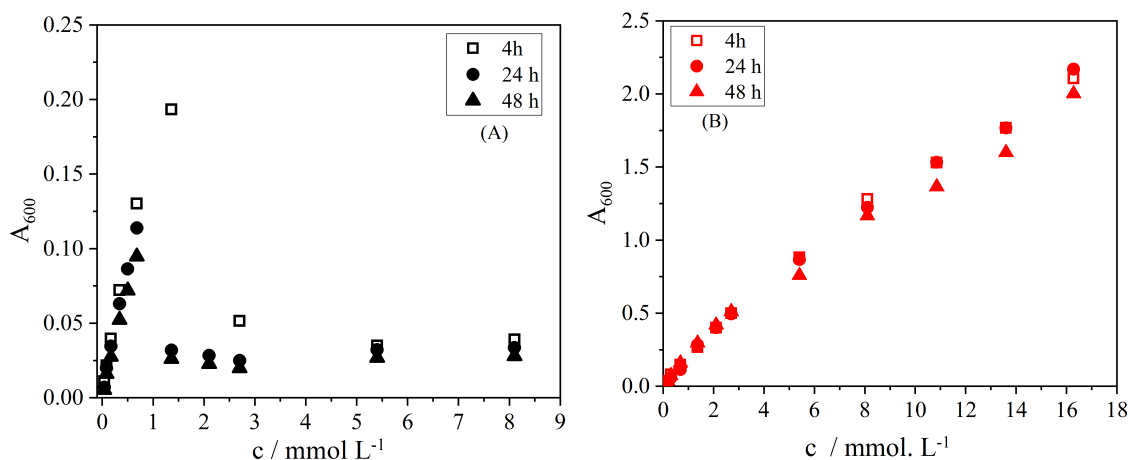


Figure 3.4. Verification of solution stability at $\lambda = 600 \text{ nm}$ for **blue dyestuff** in (A) PL1Cl and (B) PL2P solvent at the age of \square 4h, \bullet 24h and \blacktriangle 48h.

Stability of blue dyestuff in PL1Cl and PL2P solvents are represented in Figure 3.4. In PL1Cl solutions, the absorbance values in meta-stable regime reduces significantly from 4 to 24 hours and weakly from 24 to 48 hours indicating a persistent meta-stability which survives 48 hours.

In PL2P solutions, also the absorbance values are measured at three different ages of the solutions and show an overlay till 48 hours after the first measurement. It can be concluded that blue dyestuff in PL2P solvent holds a good stability.

Results of UV-vis spectroscopy at different concentrations of **red dyestuff** are presented in Figure 3.5. A noticeable reduction of absorbance after the c_{max} proves the meta-stability of red dyestuff same as the blue one. As was found in the case of two other dyestuffs, the solubility of red dyestuff in PL2P is higher than PL1Cl. In PL1Cl, the absorbance values are almost constant at concentrations higher than 2.7 mmol/L (saturated state). Break of the Beer-Lambert law at concentration of 0.01 mmol/L reveals a very low solubility of red dyestuff in PL1Cl solvent. The meta-stable solutions in PL1Cl are observed in the concentration range of $0.01 \text{ mmol/L} < c < 2.7 \text{ mmol/L}$.

In PL2P, red solutions exhibit a growth of absorbance by increasing the concentration of dyestuff up to 26.1 mmol/L . Above these concentrations a deviation from the Beer-Lambert law emerges due to the precipitation or aggregation in the solution. The absorbance values decrease significantly and the last data points form a plateau which represents the saturated level.

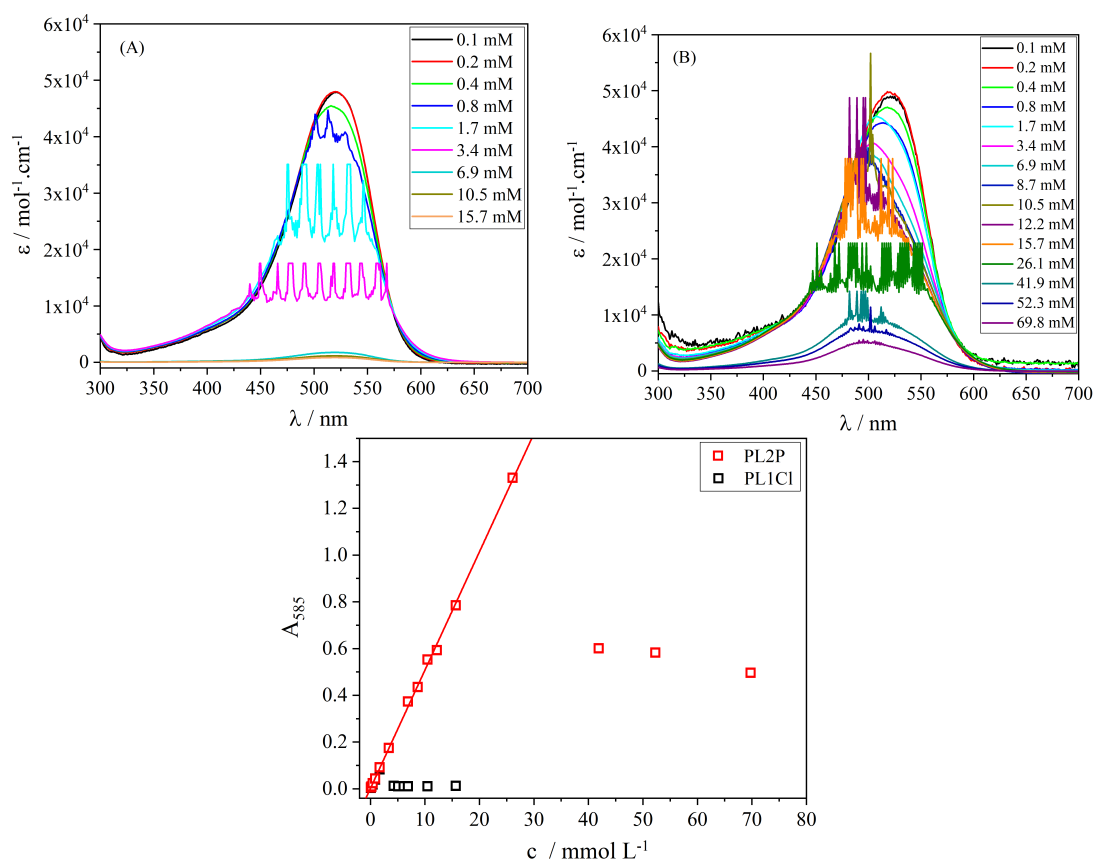


Figure 3.5. Molar extinction coefficients ϵ versus wavelength λ for different concentrations (in mmol/L) of red dyestuff in (A) PL1Cl and (B) PL2P solvent at the age of 4 hours. (C) Verification of solution stability at $\lambda = 585 \text{ nm}$ for red dyestuff in PL1Cl \square and PL2P \square solvent at the age of 4 hours.

The stability of the red dyestuff in the two solvents is represented in Figure 3.6. Absorbance values are measured at three different ages of the solutions and reveal a slight decrease of values in the saturated level after 24 hours. The absorbance values for the entire measured range of concentrations for all three dyestuffs are represented in Appendix II.

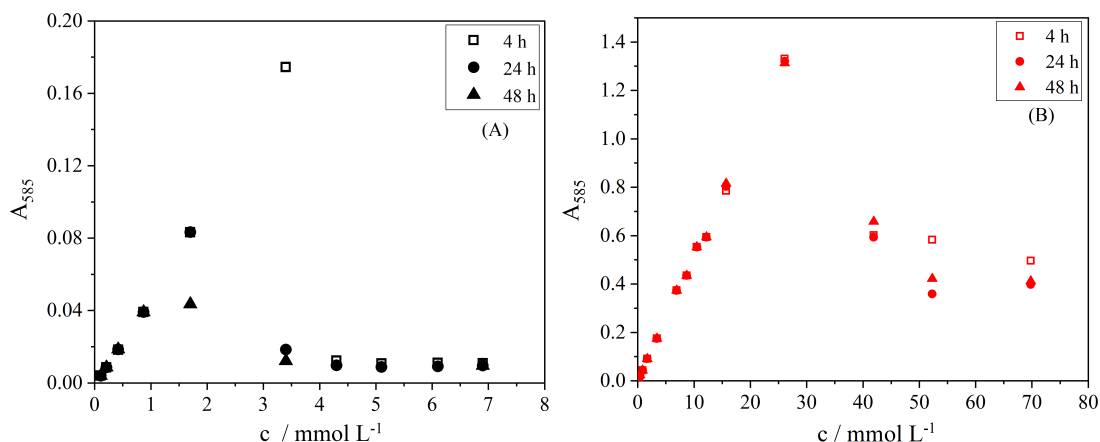


Figure 3.6. Verification of solution stability at $\lambda = 585 \text{ nm}$ for **red dyestuff** in (A) PL1Cl and (B) PL2P solvent at the age of \square 4h, \bullet 24h and \blacktriangle 48h.

An interesting phenomenon which comes into view in case of blue and red solutions is a blue shift of the absorption maximum. The effect becomes visible by increasing the concentration of dyestuff. Figure 3.7 displays the λ_{max} (the wavelength corresponding to the highest measured absorbance) for different concentrations of blue and red dyestuffs in PL1Cl and PL2P solvent. A blue shifted absorption peak occurs in both solvents. Formation of H-aggregates for this blue shift is anticipated [92, 93].

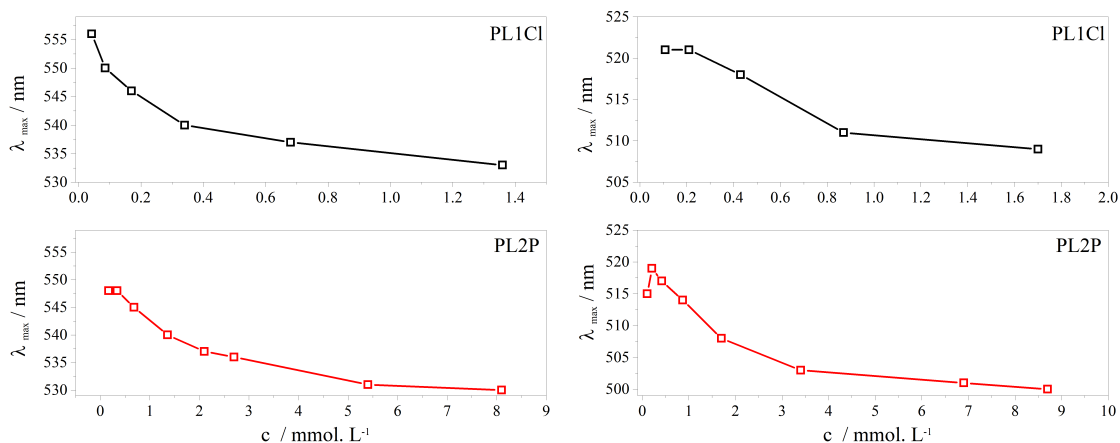


Figure 3.7. Representation of λ_{max} for different concentrations of (left) blue and (right) red dyestuffs in PL1Cl and PL2P solvents.

To summarize, it has been found that the solubility of all three dyestuffs in PL2P is better than PL1Cl. Yellow dyestuff represents a good stability in both solvents. Regardless of the type of the solvent, blue and red dyestuffs exhibits a concentration regime with meta-stable solutions except the case of blue in PL2P.

3.2 Solubility of the Acidic Dyestuffs in the Presence of Additives

As was explained in Section 1.2 improving the uptake of dyestuff is favorable in textile industries and dyeing processes. Benzyl alcohol and isopropanol are well known additives which are expected to enhance the solubility of dyestuff in aqueous solution thereby increasing the uptake of dyestuff into the fibers. Hence, it is appropriate to investigate the solubility of acidic rainbow dyestuffs in the presence of solvents which are altered by adding benzyl alcohol, isopropanol and guanidine sulphate to PL1Cl and PL2P where the resulting solvents are named as PL1BA, PL1IP, PL1Gn, PL2BA, PL2IP and PL2Gn respectively.

Figure 3.8 compares the Beer-Lambert law for **yellow dyestuff** dissolved in different solvents. It can be seen that adding benzyl alcohol and isopropanol to the PL1Cl solvent increases the solubility of dyestuff up to 40% (Figure 3.8-A). The solubility of yellow dyestuff is increased up to 21 mmol/L for PL1BA and 19.9 mmol/L for PL1IP compared to PL1Cl. After these concentrations the curves start to bend and form a plateau, which represents a saturated state.

Guanidine sulphate shows the opposite effect as it reduces the solubility of yellow dyestuff in the saturated state. Up to the concentration of 15.8 mmol/L the Beer-Lambert law is satisfied and after this concentration there is a sharp reduction in the absorbance values indicating meta-stable solutions, eventually, a plateau is established by the last three data points. At this concentration range ($19\text{ mmol/L} < c < 31.7\text{ mmol/L}$) the solubility of yellow dyestuff reduces by a factor of $1/2$ compared to the reference solvent PL1Cl.

Figure 3.8-B implies that in the measured concentration range, the additives could not change the solubility of yellow dyestuff in PL2P based solvents significantly. No saturated state was achieved for yellow dyestuff in PL2P and adjusted PL2P solvents because it was not possible to measure the spectra higher than 31.7 mmol/L . Almost the same trend of Beer-Lambert has been found for all three additives where the absorbance value rises by increasing the concentration of dyestuff. Absorbance spectra and molar extinctions measured from the yellow dyestuff in all solvents adjusted with the these additives are represented in Appendix II.

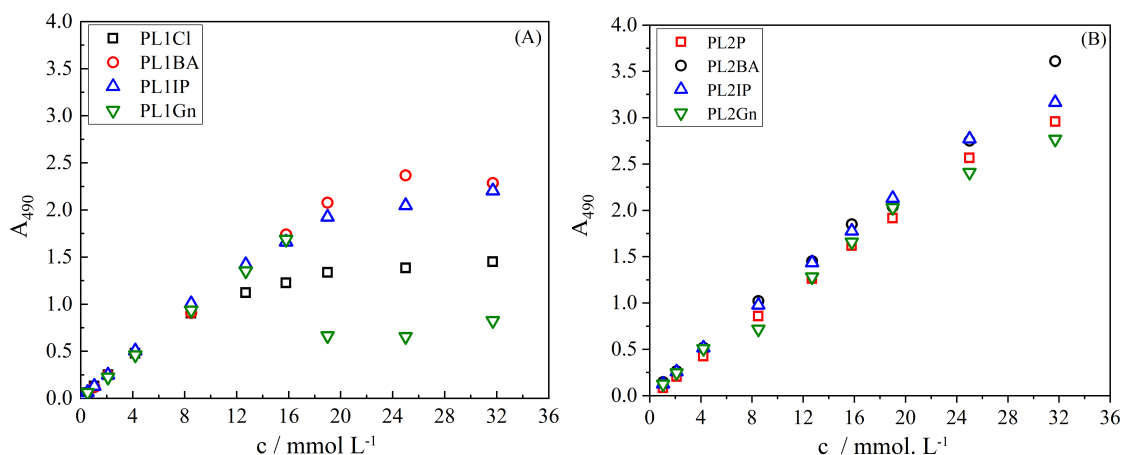


Figure 3.8. Comparison of the solubility limit via investigation of Beer-Lambert law for **yellow dyestuff** dissolved in (A) altered PL1Cl solvent and (B) altered PL2P solvent at $\lambda = 490\text{ nm}$ and the age of 24 hours.

Figure 3.9 illustrates the Beer-Lambert law for **blue dyestuff** dissolved in the different solvents.

A meta-stable regime can be seen for all solutions in Figure 3.9-A. Benzyl alcohol and isopropanol increase the solubility of blue dyestuff in the PL1Cl solution where the effect of isopropanol is significantly higher than the benzyl alcohol and meta-stable regime becomes visible in the high concentration range of 10 mmol/L (subplot in Figure 3.9-A). In the presence of benzyl alcohol, the c_{max} in meta-stable regime for blue dyestuff is measured as 0.68 mmol/L . Above this concentration the absorbance decreases and the last three data points form a plateau where the absorbance values are 60% higher than the values measured from PL1Cl. The absorbance measured from PL1Gn and PL1Cl solutions overlay clarifying that guanidine sulphate could not change the solubility of blue dyestuff with respect to PL1Cl.

Figure 3.9-B implies that the additives benzyl alcohol and isopropanol given to PL2P do not change the solubility of blue dyestuff remarkably. No meta-stable phase is noticed with the two alcohols, while in PL1Gn a meta-stable regime appears along with a sharp reduction of solubility. Almost the same trend of Beer-Lambert has been found for both benzyl alcohol and isopropanol.

It must be mentioned that the bended curves of PL2IP and PL2BA are not only representing a deviation from Lambert-Beer law but also a blue shift in the absorbance spectra as is illustrated in Figure 3.10. This blue shift is observed with and without additives in the red and blue absorbance spectra. The blue shift (bathochromic shift) suggests the formation of H-aggregates in which the dye molecules may aggregate in

a parallel way (plane to plane stacking) to form a H-oligomer. The appearance of isosbestic points in the absorbance spectra of red and blue dyestuffs in some solvents suggests an equilibrium is established between two species and reflect a binary system (monomer-aggregate). For blue dyestuff the isosbestic point is observed in PL1Gn, PL1IP and PL2IP while red has shown an isosbestic point in PL2Gn and PL2IP (see Appendix II).

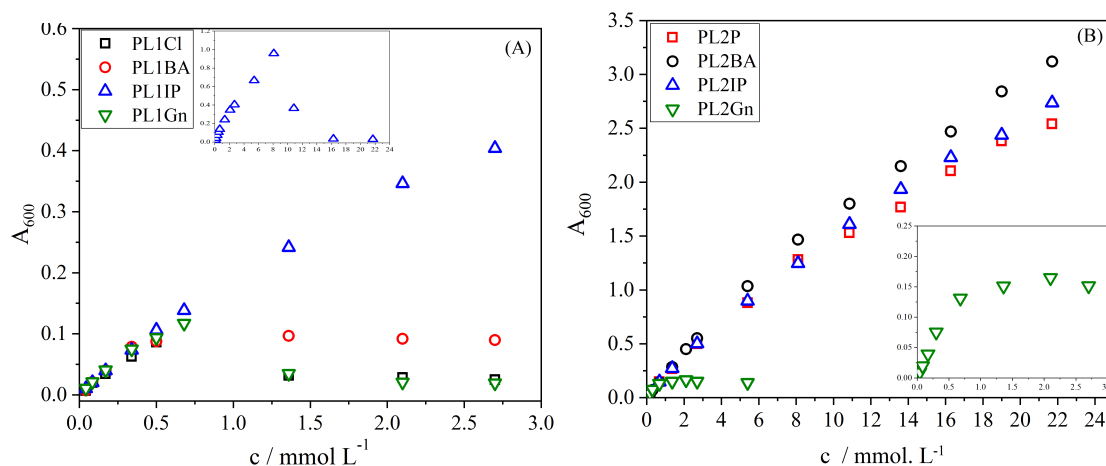


Figure 3.9. Comparison of the solubility limit via investigation of Beer-Lambert law for **blue dyestuff** dissolved in (A) altered PL1Cl solvent and (B) altered PL2P solvent at $\lambda = 600\text{ nm}$ and the age of 24 hours.

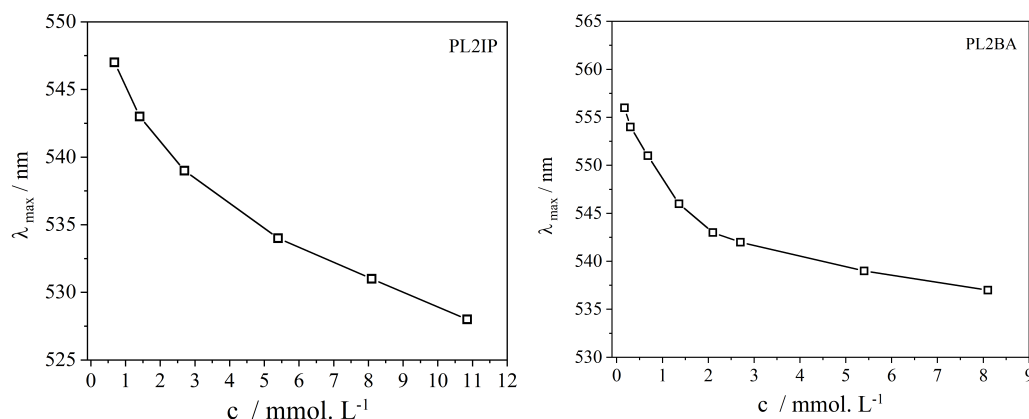


Figure 3.10. Representation of λ_{max} for different concentrations of blue dyestuff in PL2IP and PL2BA solvents at the age of 24 hours.

Figure 3.11 evaluates the effect of different additives on the solubility of **red dyestuff** dissolved in different solvents at the wavelength of $\lambda = 585\text{ nm}$ 24 hours after preparation of the solutions. In all 4 solvents based on PL1Cl, Lambert-Beer behavior is observed

up to a certain limit (c_{max}). Isopropanol and benzyl alcohol decrease the solubility of red dyestuff in meta-stable regime. In the presence of guanidine sulphate, the reduction is significant in the entire concentration range.

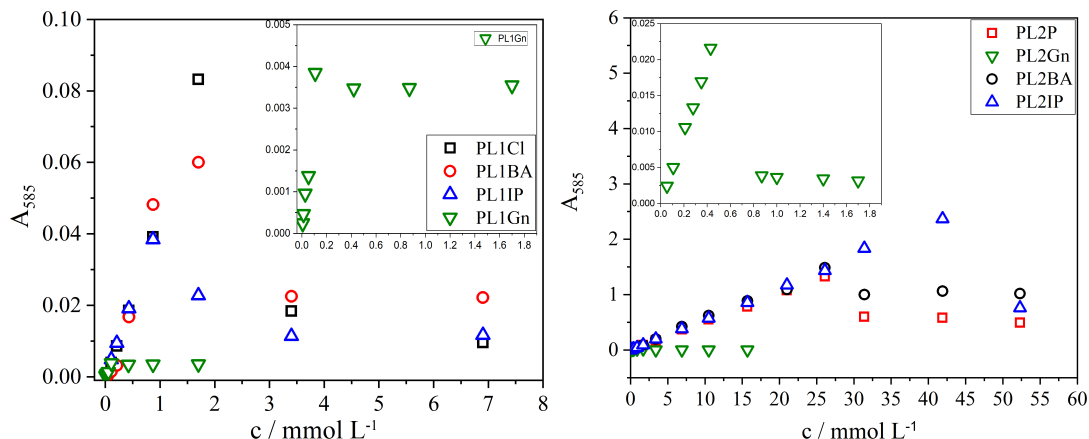


Figure 3.11. Comparison of the solubility limit via investigation of Beer-Lambert law for **red dyestuff** dissolved in (A) altered PL1Cl solvent and (B) altered PL2P solvent at $\lambda = 585\text{ nm}$ and the age of 24 hours.

Appendix II gives the detail of measurements which are performed in later times to assess the stability of solutions. The yellow dyestuff exhibits a good stability till 72 hours in all altered solvents. In case of PL1BA and PL1IP the stability assessment was extended respectively to 6 days and 17 days which in both cases have shown a perfectly stable solution.

For blue dyestuff in PL1BA, PL2BA and PL2IP the solutions are stable till age of 48 hours while in PL1Gn, PL2Gn and PL1IP the solutions are unstable from 24 hours on.

Red dyestuff turns out to be stable in both PL1BA and PL2BA till 48 hours. PL2IP solutions are also stable after 48 hours while PL1IP solutions failed to be stable in the age of 24 hours. Despite of low solubility, PL1Gn and PL2Gn show a good stability for red solutions up to 48 hours.

The solubility limit of rainbow dyestuffs in different solvents are summarized in Figure 3.12, Table 3.1 and Table 3.2. Clearly PL2P provides a better solubility than PL1Cl for all three dyestuff in both saturated and meta-stable states. It can be concluded that benzyl alcohol and isopropanol increase the solubility of yellow dyestuff in saturated solutions (compared to the PL1Cl) by a factor of ≈ 1.6 and ≈ 1.5 respectively. Guanidine sulphate raised the solubility of yellow dyestuff in meta-stable regime by a factor of ≈ 1.2 while it reduces the c_{sat} almost to the half. In the case of PL2P

solutions, additives could not trigger any changes in the c_{max} values except in the presence of benzyl alcohol where c_{max} is larger than 31.7 mmol/L and measurement is limited by saturation of detector (due to the high absorbances above the sensitivity limit of detector). All comparison are related to the measurements at the age of 24 hours.

Table 3.1. Maximum concentration of dissolved dyestuff in the meta stable state (c_{max}) at different solvents. The concentrations are measured at the wavelength of $\lambda = 490 \text{ nm}$ for yellow, $\lambda = 585 \text{ nm}$ for red and $\lambda = 600 \text{ nm}$ for blue dyestuff at the age of 24 hours.

	$c_{max} \text{ /mmol.L}^{-1}$							
	PL1Cl	PL1BA	PL1IP	PL1Gn	PL2P	PL2BA	PL2IP	PL2Gn
yellow	–	–	–	15.8	–	–	–	–
red	1.7	1.7	0.87	0.1	26.1	26.1	42	0.4
blue	0.68	0.68	8.1	0.68	>21.7	>21.7	>21.7	–

Table 3.2. Highest concentration of dissolved dyestuff in the saturated state (c_{sat}) at different solvents. The concentrations are measured at the wavelength of $\lambda = 490 \text{ nm}$ for yellow, $\lambda = 585 \text{ nm}$ for red and $\lambda = 600 \text{ nm}$ for blue dyestuff at the age of 24 hours.

	$c_{sat} \text{ /mmol.L}^{-1}$							
	PL1Cl	PL1BA	PL1IP	PL1Gn	PL2P	PL2BA	PL2IP	PL2Gn
yellow	13	21	19.9	6.5	25	>31.7	25	25
red	0.24	0.58	0.26	0.1	10	18	13	0.08
blue	0.14	0.4	–	0.1	–	–	–	0.68

Figure 3.12 illustrates that benzyl alcohol and guanidine sulphate made no changes in the solubility of blue dyestuff in PL1Cl in the regime of meta-stability while in the saturated state, benzyl alcohol increased the solubility by a factor of ≈ 2.8 and guanidine sulphate reduced it by almost 25%. Isopropanol has shown the highest impact to enhance the solubility of blue dyestuff in meta-stable regime while it decreases c_{sat} significantly. Like the case of PL2P, PL2BA, PL2IP and PL2Gn has shown no meta-stability for blue dyestuff, although PL2Gn reduces the solubility of blue dyestuff remarkably.

Guanidine sulphate lowers drastically the solubility of red dyestuff in both solvents (c_{sat} and c_{max}). Benzyl alcohol improves c_{sat} in both solvents isopropanol enhance the c_{max} only at PL2IP.

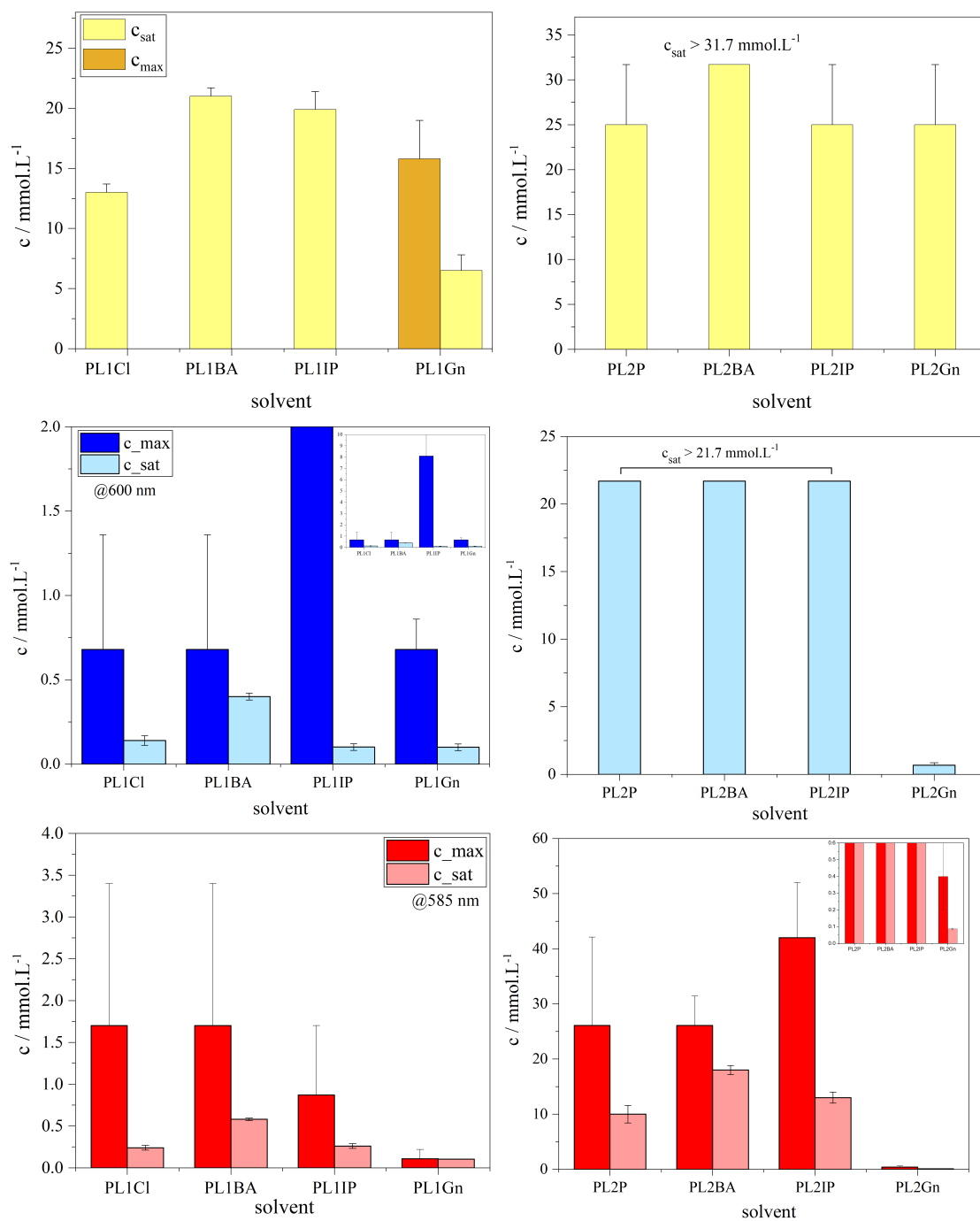


Figure 3.12. Different solubility limits of (A) yellow, (B) blue and (C) red dyestuff in different solvents at the age of 24 hours.

Furthermore it is interesting to investigate the competition of two additives with opposite effect. The question may arise that whether the benzyl alcohol assists the solubility of dyestuff in the presence of guanidinium sulphate or the guanidinium sulphate suppresses the benzyl alcohol. To this purpose, the solvent *PL1BAGn* is prepared including 2% benzyl alcohol and 3% guanidinium sulphate to be compared with *PL1Cl*. The Beer-Lambert law in Figure 3.13 compares the power of two mentioned additives affecting the solubility of the acidic dyestuffs. Stability of solutions are shown in Figure 3.14.

A very fascinating result is related to the yellow dyestuff in saturated state where the benzyl alcohol increases the c_{sat} and guanidine sulphate brings it down. But when the both additives are included in *PL1BAGn*, they compensate each other as the Beer-Lambert law approaches again the plateau of the reference solvent *PL1Cl*.

For the blue solution the effect of *PL1BA* and *PL1BAGn* at meta-stable regime is almost the same where they both increase the solubility of dyestuff. In saturated state c_{sat} exhibits the same behavior as yellow dyestuff.

In case of the red solution, the effect of guanidinium sulphate in *PL1BAGn* is very dominant acting as a strong precipitation agent. The dye molecules in *PL1BAGn* aggregate to an extent which is almost equal to that of the *PL1Gn* solvent (green and purple symbols in Figure 3.13-C).

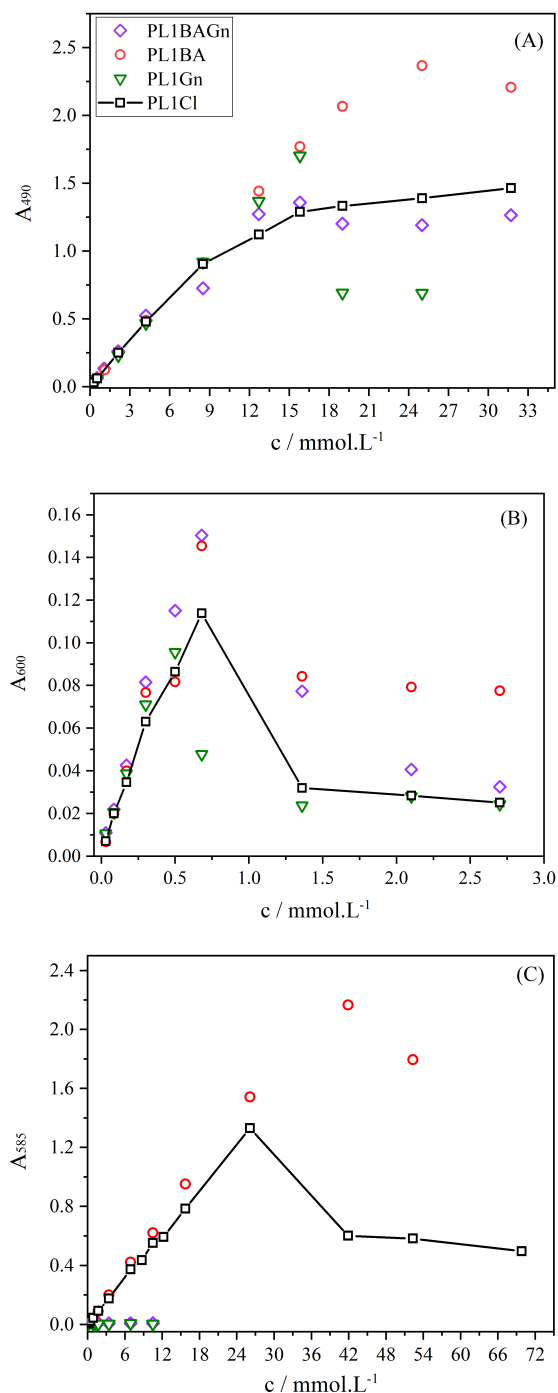


Figure 3.13. Comparison of the solubility limit via investigation of Beer-Lambert law for (A) yellow dyestuff at $\lambda = 490 \text{ nm}$ (B) blue dyestuff at $\lambda = 600 \text{ nm}$ and (C) red dyestuff at $\lambda = 585 \text{ nm}$ in PL1BAGn solvent at the age of 24 hours.

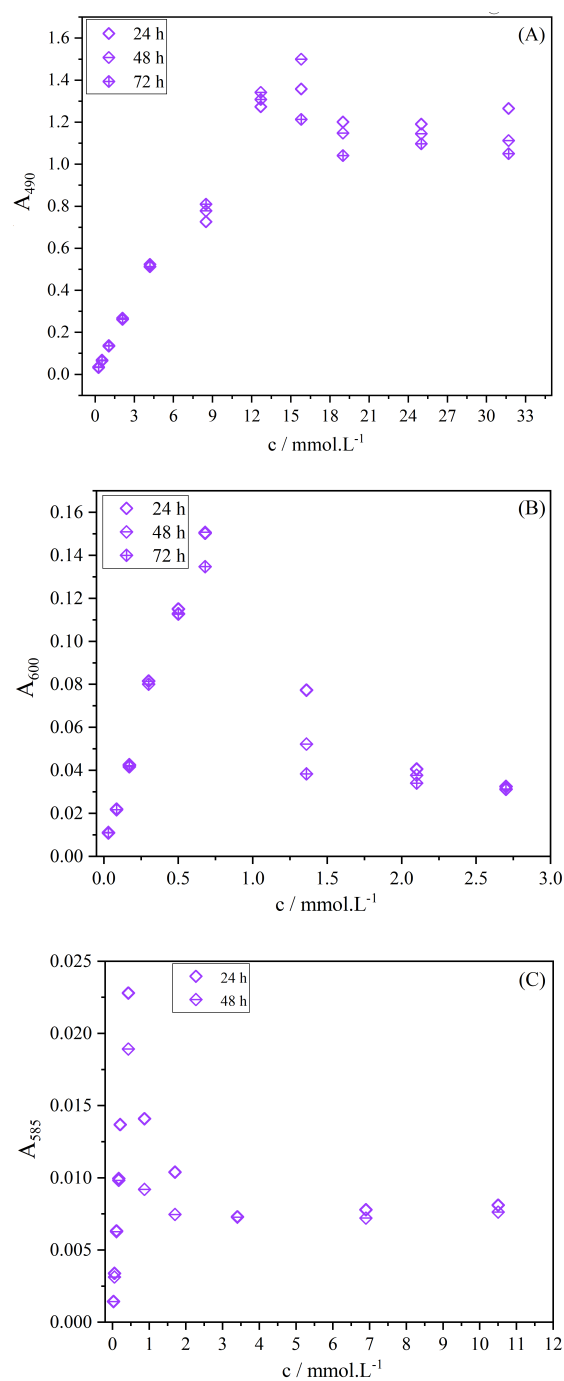


Figure 3.14. Evaluation of the stability of (A) yellow dyestuff at $\lambda = 490 \text{ nm}$ (B) blue dyestuff at $\lambda = 600 \text{ nm}$ and (C) red dyestuff at $\lambda = 585 \text{ nm}$ in PL1BAGn solvents.

All in all, PL2P solvents provided a better solubility than the PL1Cl solvents (Figure 3.12). In PL2P solvents where Na_2HPO_4 was used as a buffer, a higher pH was achieved leading to a better solubility of all three dyestuffs than PL1Cl. In addition to the good solubility which is an important parameter in dyeing processes and treatment practices, PL2P dye solutions displayed a good stability for all three dyestuffs.

In some cases the solubility of dyestuffs were boosted by adding the benzyl alcohol and isopropanol to the reference solvents PL1Cl and PL2P (for yellow dyestuff, enhancement of c_{sat} in PL1BA, PL1IP and PL2BA; for blue dyestuff enhancement of c_{max} in PL1IP and c_{sat} in PL1BA; for red dyestuff enhancement of c_{max} in PL2IP and c_{sat} in PL1BA). These outcomes can be used in dyeing processes to meet the demands of the consumer market. The mentioned additives increase the effective volume available for the diffusion of dyes and consequently the diffusion rate in the fiber (hair, wool, ...) is enhanced. This important result has the advantages of high rate of dye uptake and short time of dyeing process. It plays an important role in industrial production and utilization of dyestuffs as it includes economic advantages in terms of increased productivity, and the decrease of environmental pollution, allowing a more efficient utilization of the water resources.

Correspondingly, the reverse diffusion process can occur when the hair is washed, leading to the removal of dyestuffs from the hair. Therefore a second agent like Guanidinium sulphate can be considered to elevate the fastness of dye molecules to the hair fiber (wash fastness). Guanidinium sulphate has been found to reduce the solubility of all three dyestuffs. The only exception was the case of yellow dyestuff in PL2P solvent. Therefore it can be considered as an agent which allows a better resistance to wash fastness (Figure 3.15-B).

To investigate our expectations about the effect of additives on coloration and also on the durability of colors in the fibers, some measurements on the hair samples (goat hair) in the Kao lab (Kao Germany GmbH, Darmstadt) have been done. The hair samples dyed with yellow solution reveals a good wash fastness in the presence of guanidinium sulphate while benzyl alcohol deteriorates both durability and coloration (Figure 3.16). It is also found that BA and IP have a positive effect on the coloration of blue and red dyestuffs while the combination of them enhances the wash fastness. The other suggestion for using the emulsifying nature of $GnSO_4$ is to apply it as an after-treatment at the end of dyeing process to provide high molecular weight and deposit on the fiber (hair) resulting in a better color fastness .

(A)		
yellow	blue	red
		
pH = 7.0	pH = 7.0	pH = 7.0
PL 1C1	PL 1C1	PL 2P
		
pH = 10.40	pH = 10.27	pH = 11.26

(B)		
PL1BA		PL2BA
		
pH = 10.20	pH = 10.30	pH = 11.29
PL1Gn		PL2Gn
		
pH = 10.40	pH = 10.37	pH = 11.36

Figure 3.15. (A) Increasing the color uptake into the hair fiber by elevating the pH of dyeing liqueur. (B) Effect of benzyl alcohol and guanidinium sulphate on durability and fastness of the color in dyeing process.























PL1Cl		PL1BAGn		PL1Gn		PL1BA	
Rainbow Yellow 0,02% + Rainbow lotion 0%							
30min/40°C / Goat hair							
fresh colored	30min/40°C shake bath	fresh colored	30min/40°C shake bath	fresh colored	30min/40°C shake bath	fresh colored	30min/40°C shake bath
							
							
							

Figure 3.16. The effect of combined and separately used additives on the dye ability and wash fastness of the dyed hair samples.

3.3 Effect of Ammonium Salts on the Aggregation of Acidic Dyestuffs

As it is discussed in section 1.2, the nature of cations and anions can change the solubility of acidic dyestuffs in aqueous solutions. Here we evaluate the effect of different salts on the solubility of three rainbow acidic dyestuffs, which may aggregate in solution. To this purpose, the acidic rainbow dyestuffs are first dissolved in the solvents prepared with ammonium salts of different anions belonging to the Hofmeister series. In other words, the reference solvent PL1Cl containing ammonium chloride salt as buffer was altered. The NH_4Cl was replaced by $(NH_4)_2SO_4$, $(NH_4)_2HPO_4$ and NH_4I where the new solvents are referred as $PL1SO_4$, $PL1HPO_4$ and $PL1I$.

As is shown in Figure 3.17 the **yellow dyestuff** shows the following solubility limits: 20.9 mmol/L for $PL1SO_4$, 16.7 mmol/L for $PL1PO_4$, 14.7 mmol/L for $PL1I$ and 12.0 mmol/L for $PL1Cl$. Below this maximum solubility there is a linear relationship between the absorbance values and concentrations proving the Beer-Lambert law is satisfied and there is no aggregation at this range of concentrations. The solubility limits in this regime are represented by c_{sat} in Figure 3.17. Above c_{sat} a deviation from the Beer-Lambert law becomes visible which is a result of precipitation or aggregation in the solutions. At this point the curve starts to bend and form a plateau which represents a saturated level. It can be seen that the solubility of yellow dyestuff in the presence of NH_4SO_4 has the highest value while NH_4Cl stays in the last place of this order as it causes the lowest solubility of dyestuff in the solution. Stability of the solutions is investigated by measuring the absorbance values at two different ages of 4 and 24 hours. It can be seen that yellow dyestuff in all solvents holds a good stability.

Unlike the yellow dyestuff, **blue dyestuff** solutions exhibit a meta-stable behavior which is illustrated in Figure 3.18-A. The maximum solubility c_{max} of 1.36 mmol/L in $PL1SO_4$ and $PL1Cl$ solvents, 5.4 mmol/L in $PL1PO_4$ and 8.1 mmol/L in $PL1I$ are measured for blue dyestuff. Above these limits the absorbance values decrease significantly and finally the last data points approach a plateau implying a saturated state. The highest absorbance value in meta-stable regime c_{max} is measured from $PL1I$. The solubility limits (c_{max} and c_{sat}) at the age of 4 hours are represented in Figures 3.18.

Like the blue dyestuff a meta-stable behavior is observed for **red dyestuff** which is shown in Figure 3.19. The solubility of red dyestuff in the $PL1Cl$ reaches the highest value in terms of c_{max} (3.4 mmol/L). The other three solvents show the same c_{max} for red dyestuff (1.7 mmol/L) which is lower than the c_{max} in $PL1Cl$ by a factor of $1/2$. It is worth mentioning that the plateau for red dyestuff solutions can be determined already after 4 hours.

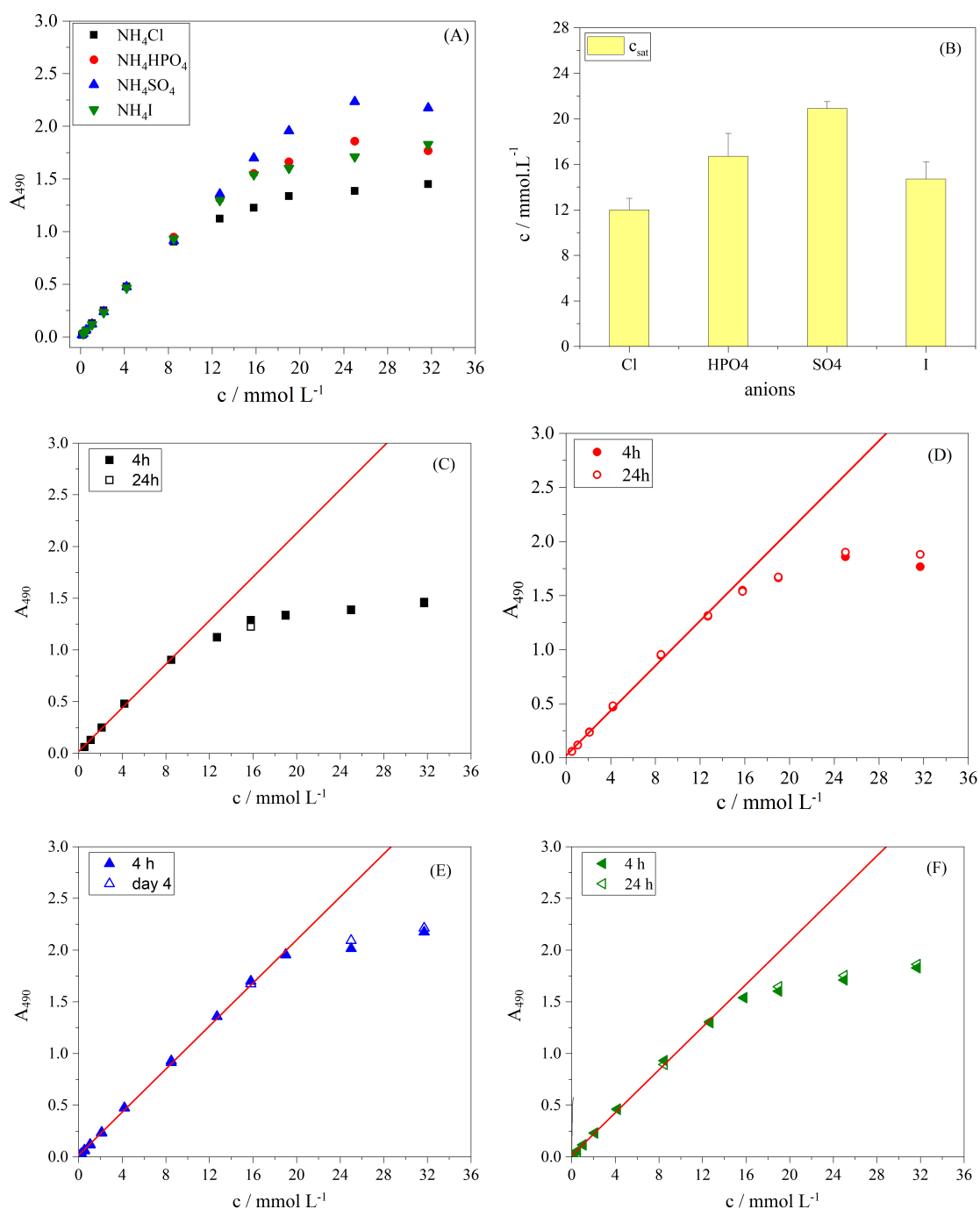


Figure 3.17. (A) Verification of solution stability and (B) maximum solubility of the **yellow dyestuff** at the age of 4 hours. Absorbances at different ages of the solutions \blacksquare PL1Cl, \bullet PL1HPO4, \blacktriangle PL1SO4 and \blacktriangledown PL1I at $\lambda = 490 \text{ nm}$.

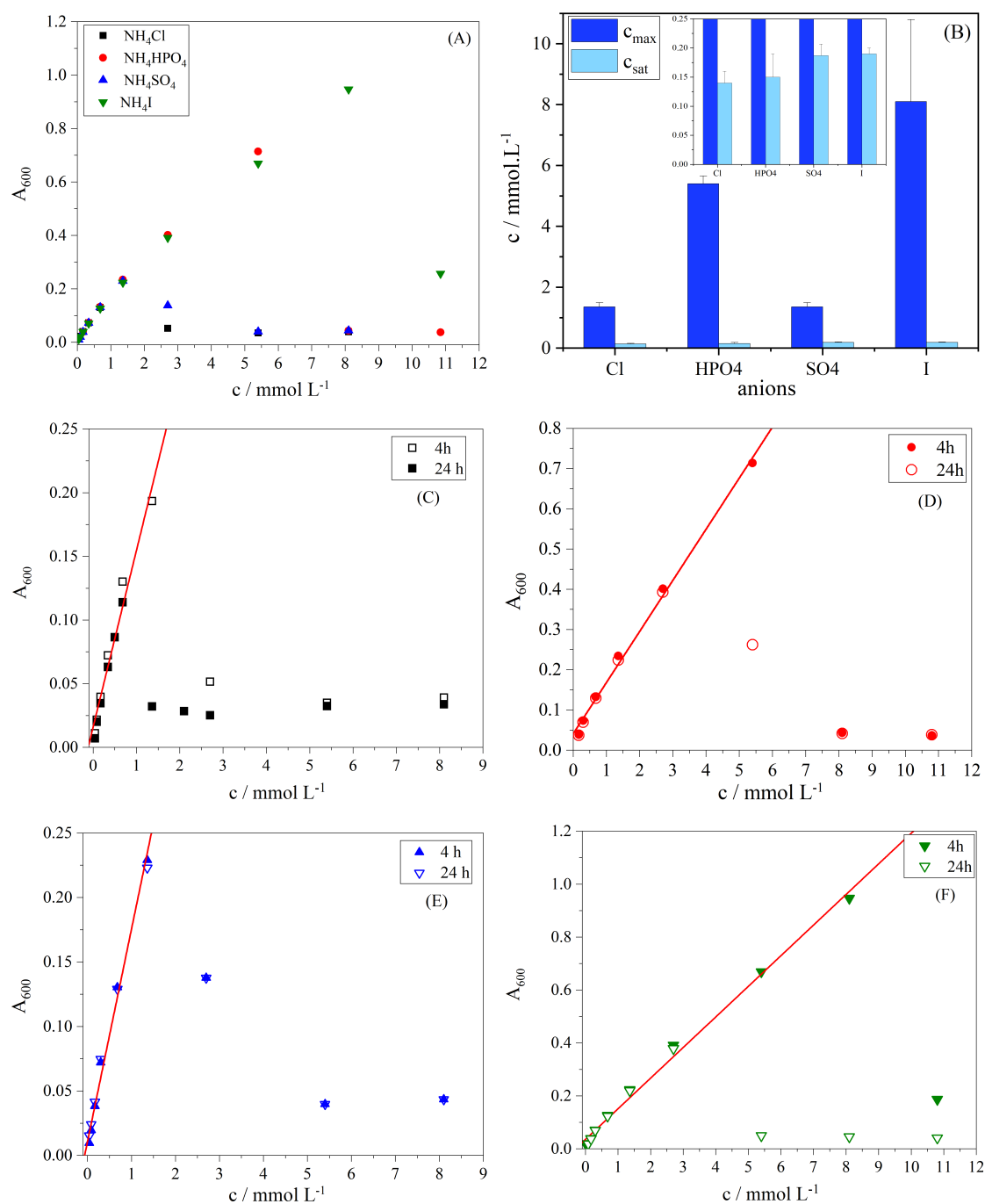


Figure 3.18. (A) Verification of solution stability and (B) maximum solubility of the **blue dyestuff** at the age of 4 hours. Absorbances at different ages of the solutions \blacksquare PL1Cl, \bullet PL1HPO4, \blacktriangle PL1SO4 and \blacktriangledown PL1I at $\lambda = 600 \text{ nm}$.

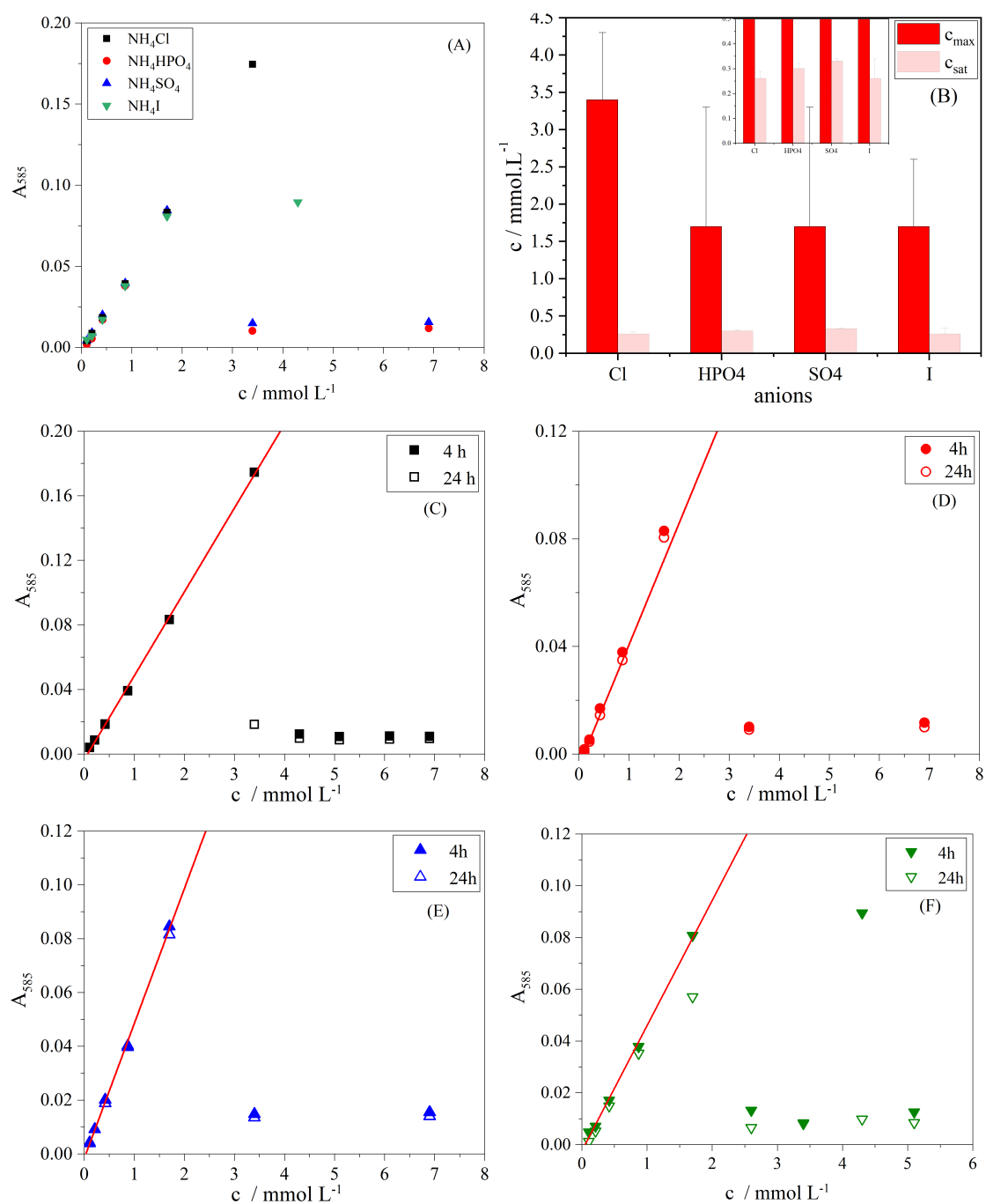


Figure 3.19. (A) Verification of solution stability and (B) maximum solubility of the red dyestuff at the age of 4 hours. Absorbances at different ages of the solutions \blacksquare PL1Cl, \bullet PL1HPO4, \blacktriangle PL1SO4 and \blacktriangledown PL1I at $\lambda = 585 \text{ nm}$.

3.4 Effect of Chloride Salts on the Aggregation of Acidic Dyestuffs

After analyzing the anions, we investigated the effect of different cations in chloride salts similar to the Hofmeister series on the absorbance spectra of the acidic dyestuffs. To this purpose, the reference solvent PL1Cl is adjusted via replacing the NH_4Cl by KCl , $NaCl$, $GnCl$ and $CaCl_2$. In the presence of $CaCl_2$ it was almost impossible to dissolve the rainbow dyestuffs in the solvent, therefore, the related measurements are not presented and only the results are reported in Table 3.3.

Figure 3.20 represents the solubility of **yellow dyestuff** in the presence of different cations. NH_4^+ causes the lowest solubility while Na^+ , K^+ and guanidinium increase it with almost the same factor. Measurements after 24 hours illustrate the yellow dyestuff is stable in the presence of all four different cations.

Meta-stable solutions have been found for **blue dyestuff** in PL1Cl, PL1Gn and PL1K already as is shown in Figure 3.21. The PL1Na solution is stable in the first 4 hours while it becomes meta-stable after 24 hours. In comparison to the ammonium, guanidinium reduces the solubility of blue dyestuff in meta-stable regime while Na^+ and K^+ increase that by a factor of 4 and 8 respectively. In the saturated state the highest solubility belongs to Na^+ . Na^+ and K^+ stand in the second and third places. Like the meta-stable regime, guanidinium brings the lowest solubility for blue dyestuff in saturated state.

Figure 3.22 shows the competition of different cations on the solubility of **red dyestuff** in solvent. Again the meta-stable solutions for all salts are revealed. Clearly potassium containing solvent provides a high solubility in meta-stable regime ($c_{max} = 10.5 \text{ mmol/L}$). It also brings the highest solubility in saturated state ($c_{sat} = 0.5 \text{ mmol/L}$) for red dyestuff. NH_4^+ and Na^+ have the same effect on c_{max} which is almost 3 times less than potassium. In saturated regime, the solubility of red dyestuff in the presence of Na^+ is higher than NH_4^+ . Guanidinium has the most interesting effect as it lowers the solubility in both meta-stable and saturated regimes drastically.

From the stability measurements which are carried out 24 hours after preparation of the solutions it can be concluded that yellow dyestuff holds a good stability in all four solvents. The detected spectra from red dyestuff in PL1Gn after 24 hours are found to be very weak so that the uncertainties are very high, therefore the measurements are skipped. The solubility limit of rainbow dyestuffs in their meta-stable state c_{max} and saturated state c_{sat} in the solvents containing different anions and cations are summarized in Table 3.3. Absorbance spectra and molar extinctions measured from all three dyestuffs in different solvents are represented in Appendix III.

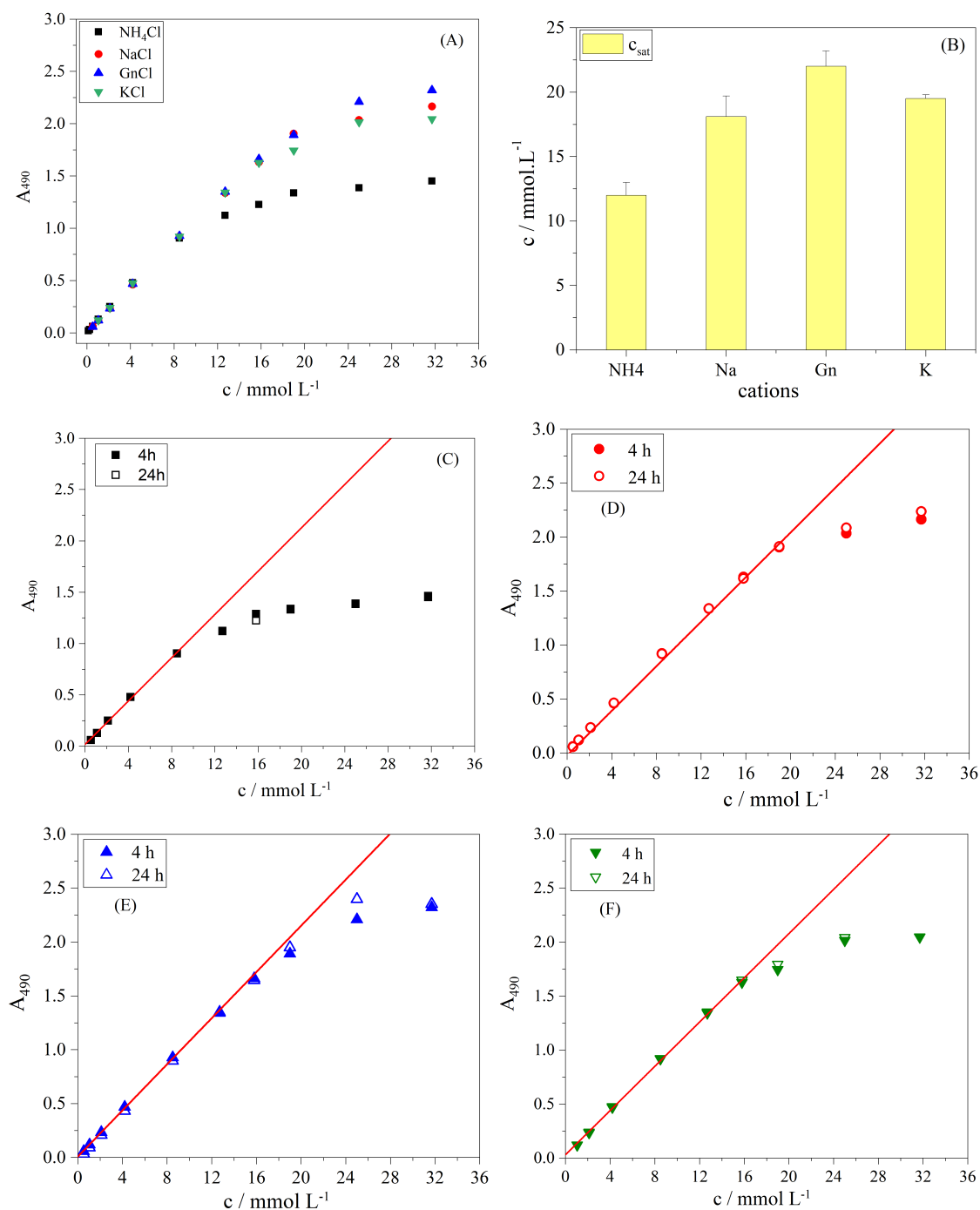


Figure 3.20. (A) Verification of solution stability and (B) maximum solubility of the yellow dyestuff at the age of 4 hours. Absorbances at different ages of the solutions \blacksquare PL1Cl, \bullet PL1Na, \blacktriangle PL3Gn and \blacktriangledown PL1K at $\lambda = 490 \text{ nm}$.

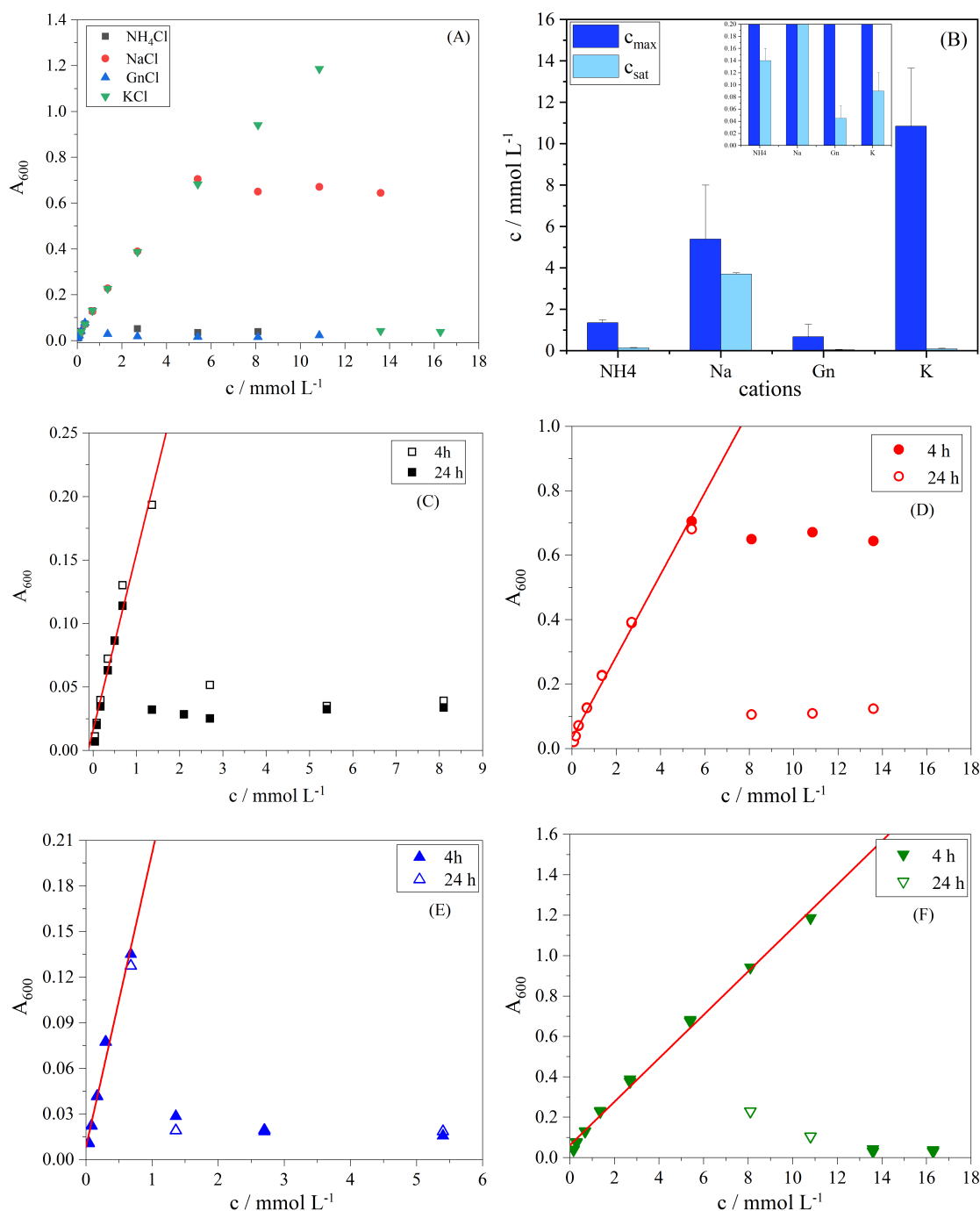


Figure 3.21. (A) Verification of solution stability and (B) maximum solubility of the **blue dyestuff** at the age of 4 hours. Absorbances at different ages the solutions \blacksquare PL1Cl, \bullet PL1Na, \blacktriangle PL3Gn and \blacktriangledown PL1K at $\lambda = 600 \text{ nm}$.

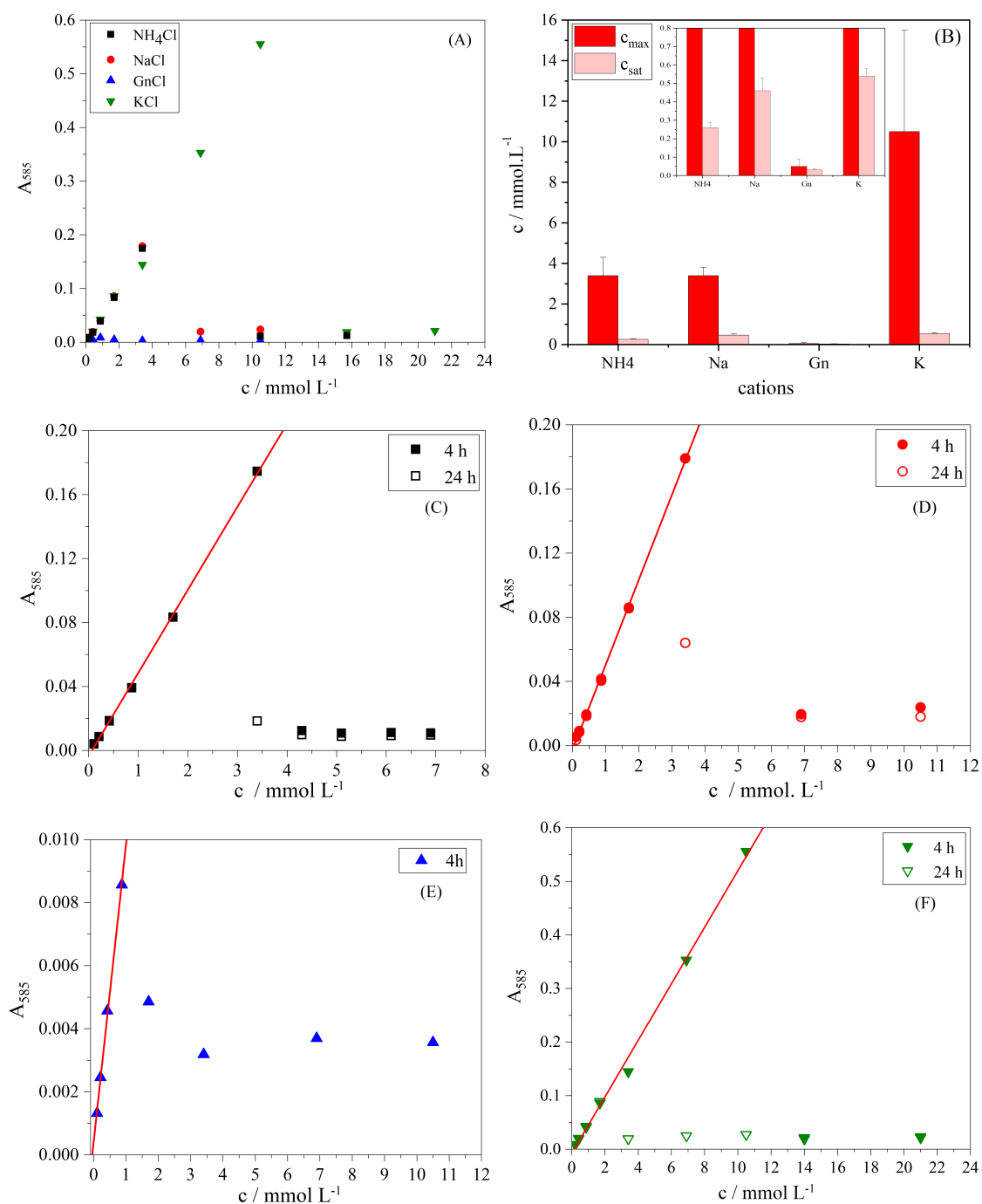


Figure 3.22. (A) Verification of solution stability and (B) maximum solubility of the red dyestuff at the age of 4 hours. Absorbances at different ages the solutions \blacksquare PL1Cl, \bullet PL1Na, \blacktriangle PL3Gn and \blacktriangledown PL1K at $\lambda = 585 \text{ nm}$.

Table 3.3. Maximum concentration of dissolved dyestuff in solvents at meta stable state (c_{max}) and saturated state (c_{sat}). The concentrations are measured at the wavelength of $\lambda = 490\text{ nm}$ for yellow $\lambda = 585\text{ nm}$ for red and $\lambda = 600\text{ nm}$ for blue dyestuff.

	$c_{max} / \text{mmol.L}^{-1}$								
	anions				cations				
	Cl^-	SO_4^{2-}	HPO_4^{2-}	I^-	NH_4^+	Gn	K^+	Na^+	Ca^{2+}
yellow	—	—	—	—	—	—	—	—	—
blue	1.36	1.36	5.4	8.1	1.36	0.68	10.8	5.4	<0.01
red	3.4	1.7	1.7	1.7	3.4	<0.05	10.5	3.4	<0.01

	$c_{sat} / \text{mmol.L}^{-1}$								
	anions				cations				
	Cl^-	SO_4^{2-}	HPO_4^{2-}	I^-	NH_4^+	Gn	K^+	Na^+	Ca^{2+}
yellow	12	20.9	16.74	14.7	12	22	19.54	18.1	<0.01
blue	0.14	0.18	0.15	0.19	0.14	0.04	0.09	3.7	<0.01
red	0.26	0.33	0.30	0.26	0.26	<0.01	0.5	0.45	<0.01

Upon considering the different anions, the highest solubility of yellow dyestuff is obtained in the presence of sulphate. The following orders can be concluded for the power of anions and cations increasing the solubility limit of **yellow dyestuff** in terms of c_{sat} :

$$SO_4^{2-} > HPO_4^{2-} > I^- > Cl^- \quad ; \quad Gn > K^+ \approx Na^+ > NH_4^+ > Ca^{2+}.$$

Due to meta-stable solutions of blue and red dyestuffs, a second classification can be assigned to the effect of anions and cations increasing the solubility limit of blue and red dyestuff in the meta stable state where the highest solubility of both dyestuffs was resulted from potassium.

A blue shift has been observed for the mentioned dyestuff solutions in all different solvents. As was discussed, the blue shifted absorption peak in water mixtures may be caused by the existence of H-aggregates where the dye molecules aggregate in a plane to plane way to form oligomers. In case of blue dyestuff, the appearance of isosbestic point in some solvents as $PL1HPO_4$, $PL1SO_4$, $PL1K$ and $PL1I$ is a proof for the existence of two species.

Based on increasing the solubility of dyestuff in meta stable and saturated state, the following orders can be derived for the effect of anions and cations on the **blue dyestuff**:

meta stable state:



saturated state:



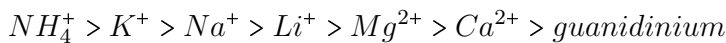
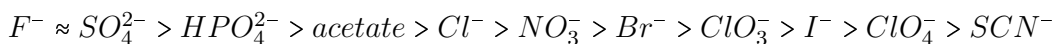
and for the **red dyestuff** at meta stable state:



and saturated state:



From the comparison of these results with Hofmeister series established according to their strength of precipitating protein:



it can be seen that Ca^{2+} is playing the same role decreasing the solubility of all three dyestuffs as it has played in the case of proteins. Guanidinium also has shown the same effect as Hofmeister series for blue and red dyestuffs while in case of yellow dyestuff it has completely the opposite effect.

Among anions, the effect of iodide is quit interesting as it opposes the order of Hofmeister series by increasing the solubility in both meta-stable and saturated states of yellow and blue dyestuffs. In the case of red dyestuff our finding about iodide is in a agreement with Hofmeister series. In case of yellow dyestuff and of the saturated state of two other dyestuffs, SO_4^{2-} could satisfy the order of Hofmeister series which is also in agreement with the results of Fedoseeva et al. in 2010 [42] when they investigated the effect of Hofmeister series anions on the aggregation/solubility of Malachite green (MG) in aqueous solution.

Investigation of Dyestuff Aggregation via Static and Dynamic Light Scattering

4.1 Aggregation of Dyestuff Induced by Ca^{2+} Ions

In using aqueous dye solutions, the phenomenon of aggregation of dye molecules may be an advantage or disadvantage. Here we investigate the aggregation behavior of the dye molecules to understand the structure of aggregated dyes themselves as well as the mechanism of their aggregation. To study the aggregation of acidic dyestuffs in aqueous solutions, an appropriate agent is needed to trigger the aggregation process. Such an agent has to decrease the solubility of solute in the solvent. According to the findings listed in Table 3.3, calcium chloride containing solvents have shown the lowest solubility for all three dyestuffs. Therefore, $CaCl_2$ can be selected as the agent to initiate the aggregation in dye solutions. Another method to trigger the aggregation of dye solutions is lowering the pH via adding acids. At the present work we use the hydrochloric acid HCl to reduce the pH of dye solutions, thereby initiating the aggregation process.

Before proceeding further, the dyestuff solutions at equilibrium must be characterized to provide suitable reference data for the time-resolved aggregation experiments. As is demonstrated in Figure 4.1 scattering curves measured from both dyestuffs in $PL1OH$ are not angular dependent thereby excluding significant aggregation. From $M_w = \Delta R_\theta / Kc$ the weight-averaged molar mass of red dyestuff is calculated as $251.89 \text{ g.mol}^{-1}$

which is close to the molar mass of a single monomer $286.57 \text{ g.mol}^{-1}$ reported by manufacturer company. For yellow dyestuff the M_w is obtained as $714.28 \text{ g.mol}^{-1}$ almost three times larger than the molar mass of a single monomer $236.45 \text{ g.mol}^{-1}$.

In high concentrations a saturation and precipitation of dyestuff in the solution occurs, therefore the proper concentrations have to be determined for the analysis of SLS-data.

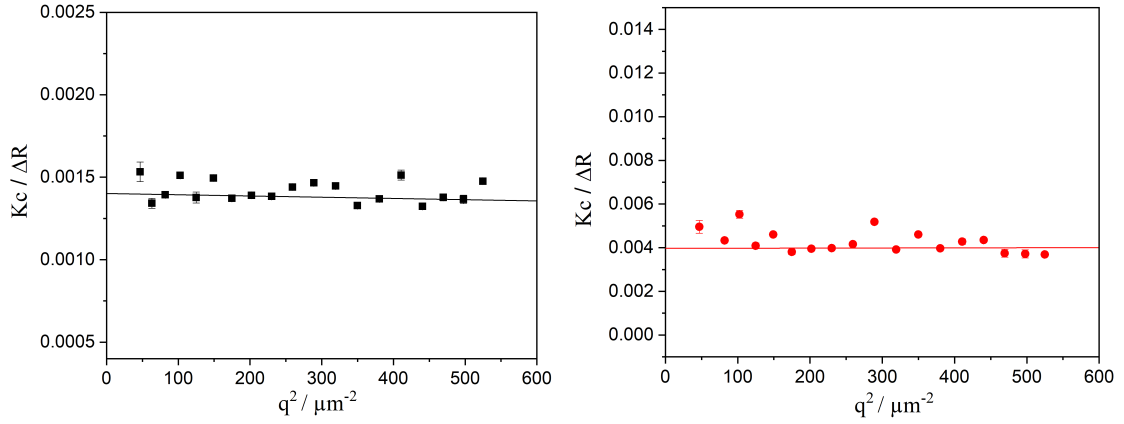


Figure 4.1. SLS scattering curves as a function of scattering angle ($30^\circ \leq \theta \leq 120^\circ$) measured from 0.5 g/L yellow dyestuff ■ and 0.25 g/L red dyestuff ● in *PL1OH*.

4.1.1 Yellow Dyestuff Aggregation Induced by Adding CaCl_2

Having established the equilibrium state prior to the addition of aggregation initiators we can now turn to TR-SLS/DLS experiment on the solutions where aggregation is induced by adding CaCl_2 . It is also important to choose the concentration of CaCl_2 carefully to avoid the formation of CaOH in the basic solvent *PL1OH* [94]. To this purpose, the solubility product of $\text{Ca}(\text{OH})_2$ ($K_{sp} = 5.5 \times 10^{-6}$) can be used to calculate Ca^{2+} concentration at the solubility limit in the solvent with a known pH ($\text{pH} \approx 12$).

$$\begin{aligned} K_{sp} &= [\text{Ca}^{2+}] \cdot [\text{OH}^-]^2 \\ 5.5 \times 10^{-6} &= [\text{Ca}^{2+}] \cdot [0.01]^2 \end{aligned} \tag{4.1}$$

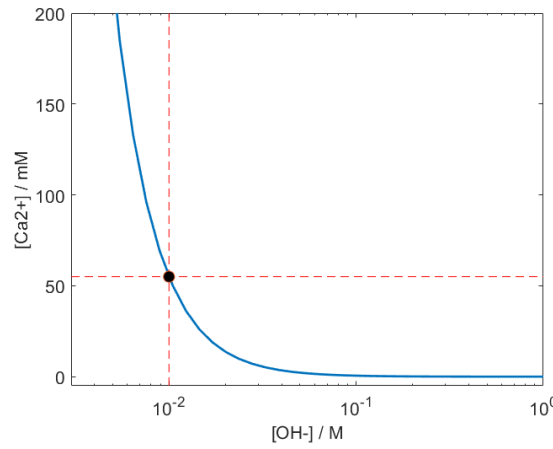


Figure 4.2. Solubility of $Ca(OH)_2$ in aqueous NaOH solutions at $25^\circ C$. The black point indicates the maximum amount of Ca^{2+} which is soluble in the aqueous NaOH solvent with $pH = 12$.

As is indicated in Figure 4.2, the maximum soluble Ca^{2+} in the aqueous NaOH solutions at pH of ~ 12 is 55 mmol.L^{-1} . In the present work, experiments are performed in a concentration range of $1.8 \text{ mmol.L}^{-1} < c < 9 \text{ mmol.L}^{-1}$ of $CaCl_2$.

The time-dependent measurements on both yellow and red dyestuffs were carried out at a temperature of $25^\circ C$ in all measurements. The time frame of a single measurement is 10 s with a delay between measurements of almost 8 s. The total measurement time varies depending on use (between 30 and 120 minutes). The refractive index of toluene is $n_{tol} = 1.4969$, the refractive index of the solvent is $n_{water} = 1.3301$. The refractive index increment dn/dc of yellow dyestuff in PL1Cl and red dyestuff in PL2P at the room temperature is determined to $0.4293 \times 10^{-3} \text{ L/g}$ and $0.6905 \times 10^{-3} \text{ L/g}$ respectively. The absolute Rayleigh ratio RR_{tol} is taken from the measurement software as $1.367 \times 10^{-3} \text{ m}^{-1}$. To calculate the hydrodynamic radius, the viscosity of water is needed which is $\eta = 0.891 \text{ mPa.s}$ at $25^\circ C$.

Experiments with yellow dyestuff were carried out right after mixing 4ml of 1 mmol.L^{-1} dye solution to 2ml of $CaCl_2$ in the concentrations of 1.8 mmol.L^{-1} , 3.6 mmol.L^{-1} and 7.2 mmol.L^{-1} . The final concentration of dyestuff in the mixture is 0.67 mmol.L^{-1} and the final concentrations of $CaCl_2$ are 0.6 mmol.L^{-1} , 1.2 mmol.L^{-1} and 2.4 mmol.L^{-1} .

At the present work, a Guinier plot with a quadratic fit is applied to evaluate the static light scattering data. A cumulant fit is used to evaluate the dynamic light scattering data and obtain the diffusion coefficient.

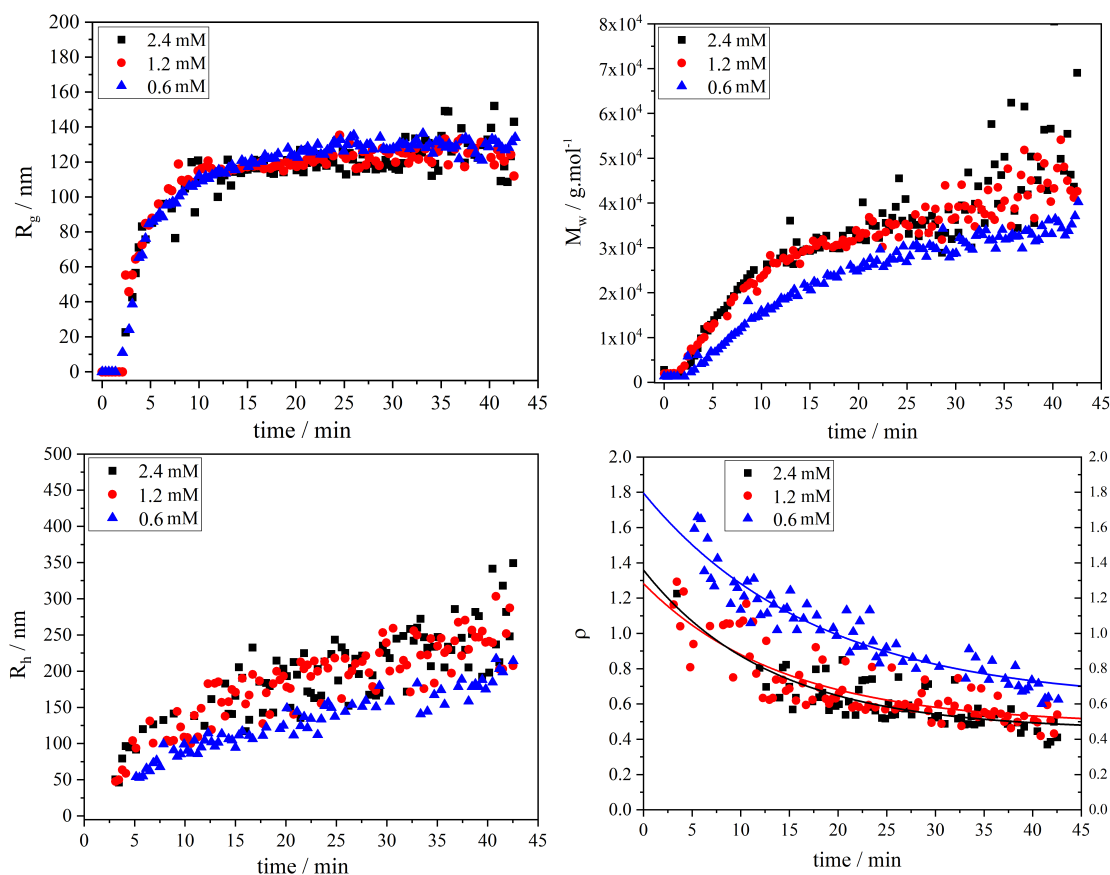


Figure 4.3. Radius of gyration R_g , hydrodynamic radius R_h , molecular weight M_w and ρ -factor of aggregated yellow dyestuff in PL1OH solvent. The final concentration of dyestuff in the mixture is 0.67 mmol.L^{-1} and the final concentrations of CaCl_2 are 0.6 mmol.L^{-1} \blacktriangle , 1.2 mmol.L^{-1} \bullet and 2.4 mmol.L^{-1} \blacksquare .

Figure 4.3 compares the radius of gyration, hydrodynamic radius and weight-averaged molar mass for the aggregated yellow dyestuff. In all three experiments an increase of the particle mass and particle size is observed from time zero when CaCl_2 is added. Particles approached their final size after 10 minutes while the molecular weight is still growing.

A UV-vis spectroscopy measurement has been performed right at the end of light scattering to determine the final amount of consumed monomers. Overlay of molar extinctions before and after adding CaCl_2 are shown in Figure 4.4-A indicating the amounts of consumed monomers too low to be calculated.

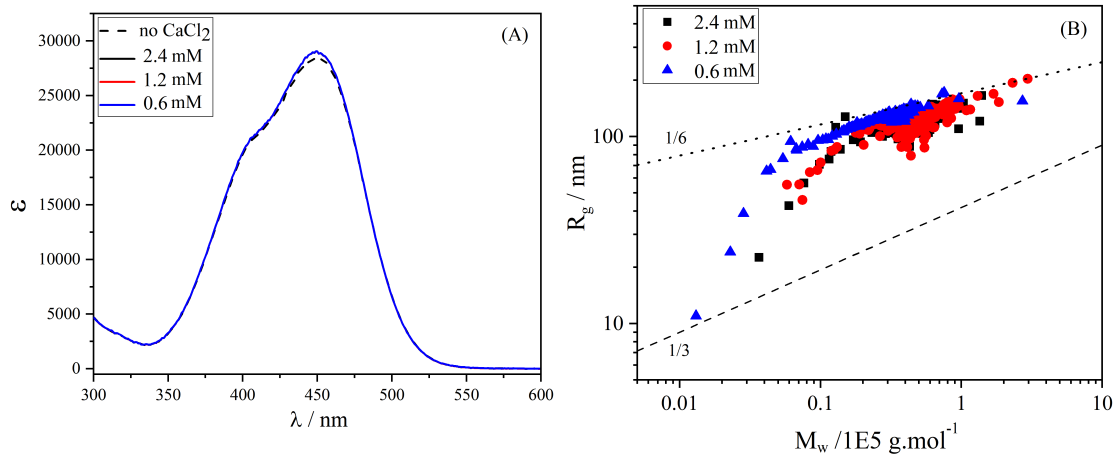


Figure 4.4. (A) Molar extinction coefficients and (B) Correlation of R_g with M_w for yellow dyestuff aggregation in PL1OH. The final concentration of dyestuff in the mixture is 0.67 mmol.L^{-1} and the final concentrations of $CaCl_2$ are 0.6 mmol.L^{-1} \blacktriangle , 1.2 mmol.L^{-1} \bullet and 2.4 mmol.L^{-1} \blacksquare . Dotted line indicates a slope of $1/6$ and dashed line $1/3$.

The exponent values α can be obtained from the correlation of particle size and particle mass presented in Figure 4.4-B. As was discussed in 2.2.3, the α values for self-similar structures of spheres, Gaussian polymer coils, and infinitely thin rods are $1/3$, $1/2$, and 1 , respectively if a step-growth process like coagulation occurs. In case of a monomer-addition growth, the mentioned values are divided by a factor of 2 [87].

Assigning a power-law to the curves of Figure 4.4-B is difficult as all three experimental curves are bended although at the end of aggregation process they approach that power law behavior with $\alpha = 1/6$ which would be compatible with the growth of compact particles according to a monomer addition process.

Establishing a theoretical model to fit the $R_g - M_w$ data during the growth of particles may provide a better perspective to evaluate the aggregation process as is presented in Figure 4.5. It can be seen that a **monomer addition** process considering a sphere shape for monomers with outer radius of $R_0 = 10 \text{ nm}$ and density of $\rho = 1 \text{ g/mL}$ has a good agreement with our experimental data. Of course such a large value for R_0 can be questioned. By selecting a smaller value like $R_0 = 0.454 \text{ nm}$ the resulted molecular weight will be $M_0 \approx 236 \text{ g/mol}$ which is in agreement with the molecular weight of the yellow dyestuff monomer $M_0 = 236.45 \text{ g/mol}$ but then there will be no agreement between the theoretical fit and our experimental data.

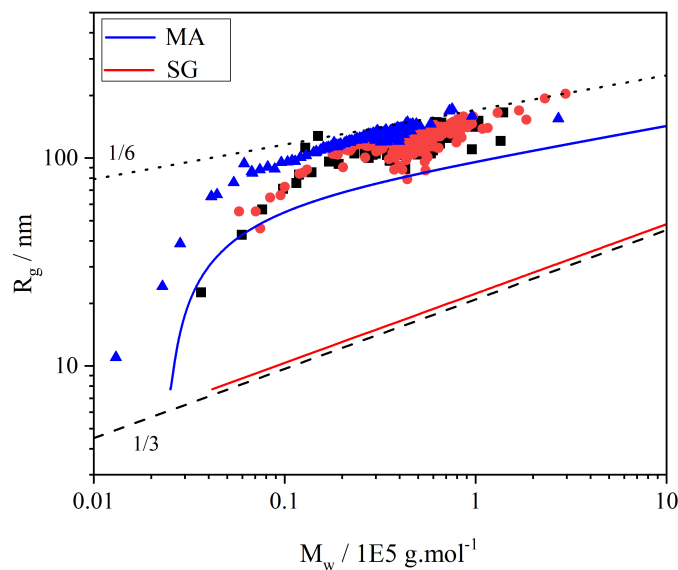


Figure 4.5. Correlation of R_g with M_w for yellow dyestuff aggregation in PL1OH. The final concentration of dyestuff in the mixture is 0.67 mmol.L^{-1} and the final concentrations of CaCl_2 are 0.6 mmol.L^{-1} \blacktriangle , 1.2 mmol.L^{-1} \bullet and 2.4 mmol.L^{-1} \blacksquare . The blue line represents a monomer addition process and the red line belongs to the step growth. The dotted line indicates a slope of $1/6$ and dashed line $1/3$.

The idea of formation of compact spheres is also supported by structure-sensitive parameter ρ shown in Figure 4.3 which displays a decreasing trend from $\rho \approx 1.5$ to final values in the regime of $0.4 < \rho < 0.7$. Such low values are observed for compact particles like spheres ($\rho = 0.77$) which are significantly smaller than ρ of polymer coils with $1.2 < \rho < 1.6$.

Formation of homogeneous, rather compact particles is further confirmed by the form-factors (Figure 4.6) of the particles, which was taken right after the time-resolved light scattering measurements. The experimental data points in plots (A) and (B) lay between the theoretical curves of sphere and Gaussian coil. In plot (C) the data points overlay with the theoretical curve from the model of a mono-disperse sphere. By increasing $q.R_g$ a deviation comes into view which is likely to stem from a certain degree of polydispersity. The final measured values of M_w , R_g , R_h , and ρ are listed in Table 4.1.

Table 4.1. The final values of R_g , R_h and M_w of aggregated yellow dyestuff at the end of TR-SLS/DLS measurement. Aggregation is initiated with variable concentrations of $CaCl_2$ and the final concentration of yellow dyestuff in the mixture is 0.67 mmol.L^{-1} . Second table shows the same parameters measured from the single angle device, right at the end of TR-SLS/DLS.

final c_{CaCl_2} [mol/L]	final R_g [nm]	final R_h [nm]	final M_w [g/mol]	ρ [g/mol]	pH of mixture
2.4×10^{-3}	140	350	0.5×10^5	0.49	11.84
1.2×10^{-3}	131	246	0.4×10^5	0.53	11.91
0.6×10^{-3}	128	175	0.3×10^5	0.71	11.93

final c_{CaCl_2} [mol/L]	final R_g [nm]	final R_h [nm]	final M_w [g/mol]
2.4×10^{-3}	253	820	3.51×10^5
1.2×10^{-3}	196	831	1.74×10^5
0.6×10^{-3}	177	430	0.84×10^5

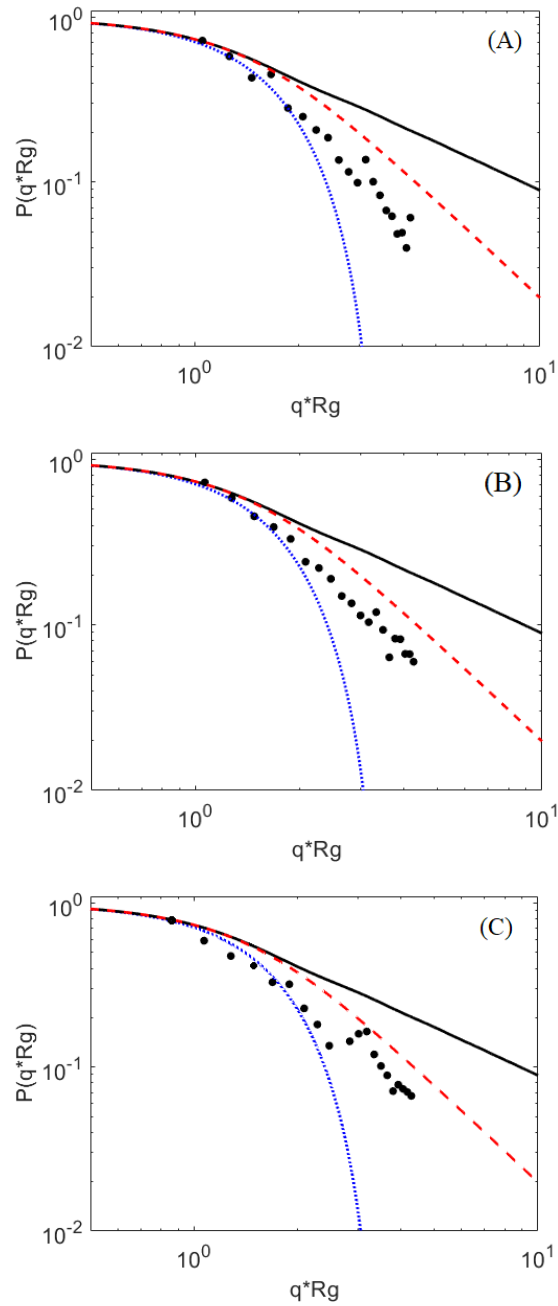


Figure 4.6. Formfactor of the aggregated yellow dyestuff initiated by $CaCl_2$. The final concentrations of $CaCl_2$ in the mixture are (A) 2.4 mmol.L^{-1} , (B) 1.2 mmol.L^{-1} and (C) 0.6 mmol.L^{-1} . The measurements are performed in an angular range of $20^\circ \leq \theta \leq 120^\circ$. The experimental data \bullet is compared to the theoretical scattering curves of a rod (—), Gaussian coil (---) and hard spheres (...)

4.1.2 Red Dyestuff Aggregation Induced by Adding $CaCl_2$

A concentration series of three samples with $CaCl_2$ contents of 9, 8 and 7.2 mmol.L^{-1} is prepared to initiate the aggregation in 0.8 mmol.L^{-1} red dyestuff solution. 4 ml of dye solution is mixed with 2 ml of aqueous $CaCl_2$ and TR-SLS/DLS is performed in 25° . Figure 4.7 represents the molecular weight M_w , radius of gyration R_g , hydrodynamic radius R_h and the molar extinction ϵ measured from aggregated red dyestuff.

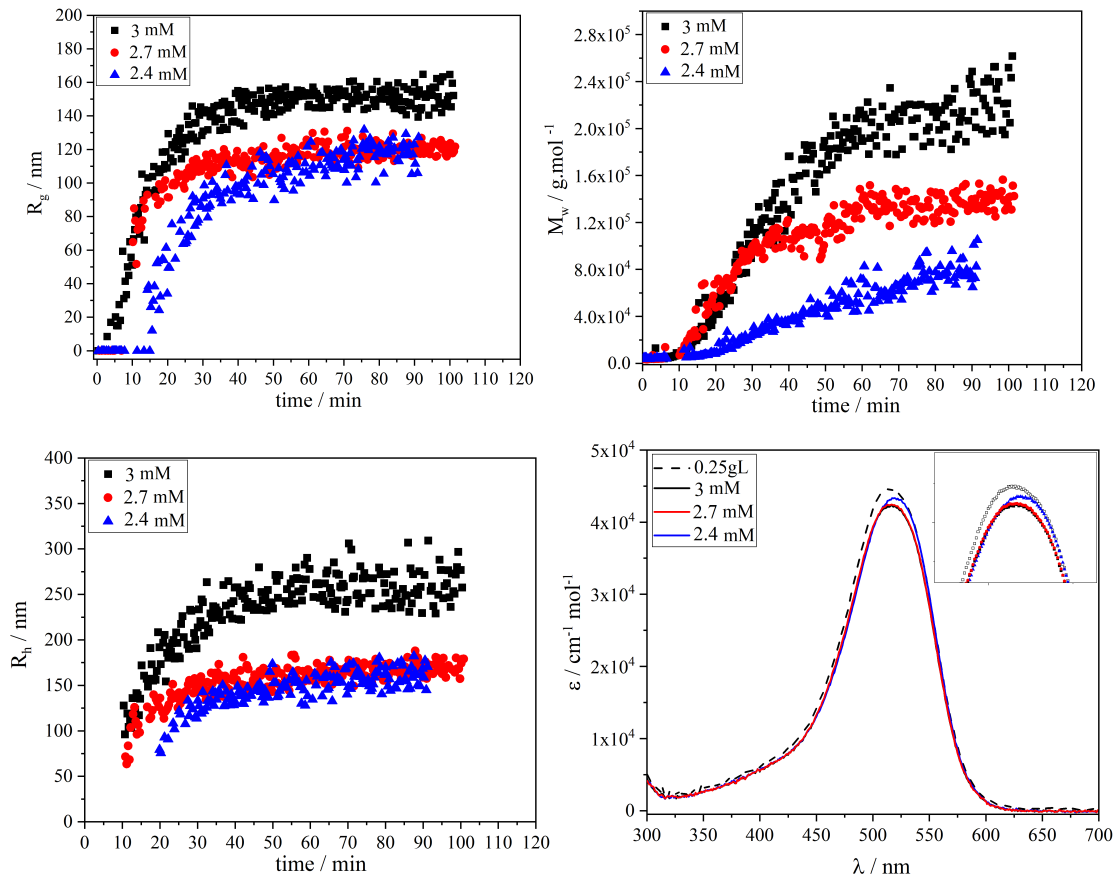


Figure 4.7. Radius of gyration R_g , hydrodynamic radius R_h and molecular weight M_w of aggregated red dyestuff in PL1OH solvent. The final concentration of red dyestuff in the solution is 0.58 mmol.L^{-1} and the final concentration of $CaCl_2$ is 2.4 mmol.L^{-1} \blacktriangle , 2.7 mmol.L^{-1} \bullet and 3 mmol.L^{-1} \blacksquare . The UV-vis spectroscopy of aggregating solutions is done right after the time resolved light scattering measurement and compared to the spectrum in the absence of $CaCl_2$ (dashed line).

Figure 4.7 illustrates a continuous increase of the particle size in terms of R_g and R_h during the first 30-40 minutes of all three measurements. Particle growth at $CaCl_2$ 2.4 mM turned out to be slower than the other measurements although the calculation of

molar extinction ϵ from UV-vis spectroscopy at the end of light scattering measurement reveals no big difference for the final amount of consumed monomers in the three measurements. The zoomed plot in Figure 4.7 demonstrates that at concentrations of 3 mM and 2.7 mM CaCl_2 maximum amount of consumed monomers by aggregation are slightly higher than at 2.4 mM showing a trend which is in a good agreement with calculated molar masses. All in all, the three spectra are almost overlaying with the spectrum before aggregation which can explain the low molecular weight of aggregated particles. There are still plenty of monomers ($> 98\%$) which are not used in aggregation process.

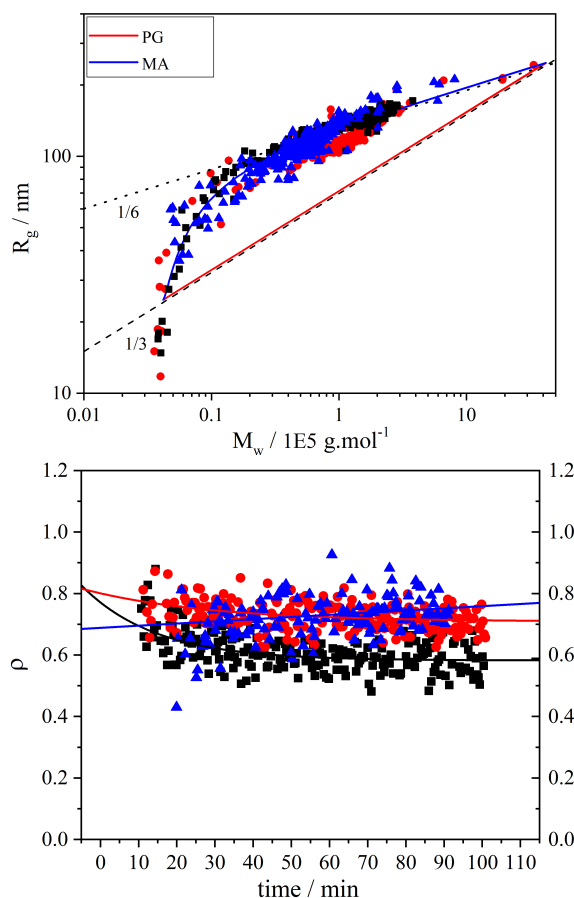


Figure 4.8. Correlation of R_g with M_w and shape sensitive factor ρ of aggregated red dyestuff in PL1OH solvent. The final concentration of red dyestuff in the solution is 0.58 mmol.L^{-1} and the final concentration of CaCl_2 is 2.4 mmol.L^{-1} \blacktriangle , 2.7 mmol.L^{-1} \bullet and 3 mmol.L^{-1} \blacksquare . The blue line represents a monomer addition process and the red line belongs to the step growth. The dotted line indicates a slope of $1/6$ and dashed line $1/3$.

From the power law in Figure 4.8, it is difficult to make a decision about the aggregation

process due to the bended curves. Again following the aggregation process in time can provide a better understanding of growth mechanism. As the red line shows, a step growth is far from our experimental data. Instead, the blue curve which represents a monomer addition process considering a sphere shape for monomers with outer radius of $R_0 = 10\text{ nm}$ and density of $\rho = 1\text{ g/mL}$ has a good agreement with our data. Again it can be seen that we have to choose a large value for R_0 to fit our experimental values.

The shape sensitive factor ρ for the measurement of 3 mM accept the value 0.6 - 0.76 which predicts the compact structures like a cube or sphere. Another hint can be given by representing the scattering curves which stay closer to the curve of a sphere than of a Gaussian coil. The scattering curves shift toward the Gaussian model coil by decreasing the content of $CaCl_2$ although the ρ -ratio of 0.75 for the experiments of 2.7 mM and 2.4 mM still votes for compact structures. The final measured values of M_w , R_g , R_h , and ρ of the aggregated red dyestuff are listed in Table 4.2.

Table 4.2. The final values of R_g , R_h and M_w of aggregated red dyestuff at the end of TR-SLS/DLS measurement. Aggregation is initiated with variable concentrations of $CaCl_2$ and the final concentration of red dyestuff in the mixture is 0.58 mmol.L^{-1} . Second table shows the same parameter measured from the single angle device, right at the end of TR-SLS/DLS.

final c_{CaCl_2} [mol/L]	final R_g [nm]	final R_h [nm]	final M_w [g/mol]	ρ [g/mol]	pH of mixture
3×10^{-3}	160	257	2.2×10^5	0.60	11.97
2.7×10^{-3}	120	160	1.4×10^5	0.75	11.96
2.4×10^{-3}	120	160	0.8×10^5	0.75	11.98

final c_{CaCl_2} [mol/L]	final R_g [nm]	final R_h [nm]	final M_w [g/mol]
3×10^{-3}	175	217	0.9×10^5
2.7×10^{-3}	165	191	0.7×10^5
2.4×10^{-3}	204	261	0.5×10^5

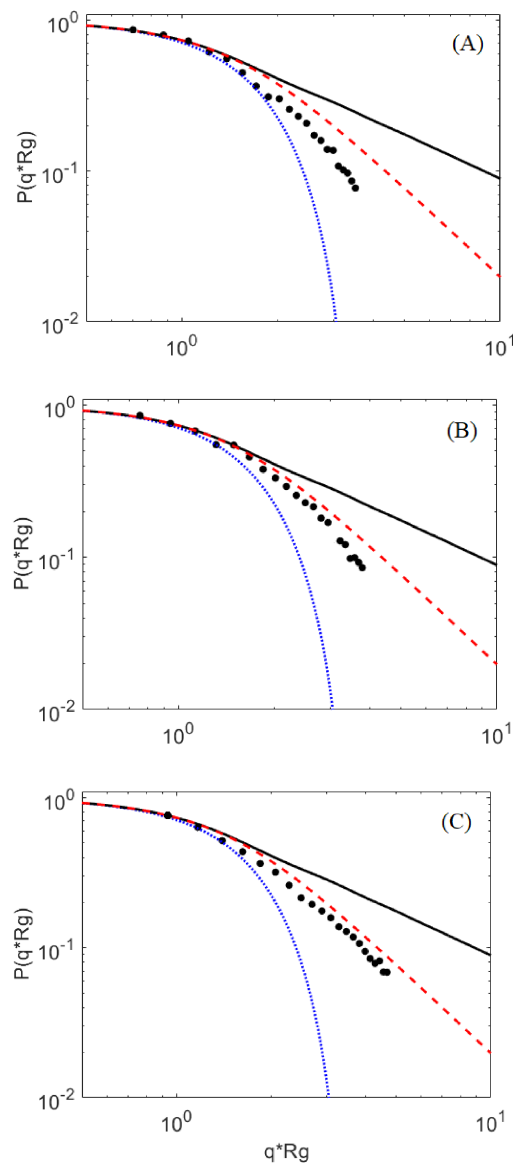


Figure 4.9. Representation of formfactor for aggregated red dyestuff in PL1OH solvent. The final concentration of red dyestuff in the solution is 0.58 mmol.L^{-1} and the final concentration of CaCl_2 is (A) 2.4 mmol.L^{-1} , (B) 2.7 mmol.L^{-1} and (C) 3 mmol.L^{-1} . The measurements are performed in an angular range of $20^\circ \leq \theta \leq 120^\circ$. The experimental data \bullet is compared to the theoretical scattering curves of a rod (—), Gaussian coil (---) and hard spheres (...).

4.2 Aggregation of Dyestuff Induced by Lowering the pH

4.2.1 Yellow Dyestuff Aggregation Induced by Lowering the pH

The dyestuff aggregation in PL1OH solvent has also been studied after addition of hydrochloric acid instead of $CaCl_2$. Since the aggregation process occurred rapidly, acid was added gradually (step by step) to the yellow dye solution at a concentration of 1 mmol.L^{-1} and pH of 11.8. The measurement has been performed during 100 minutes and the results are presented in Figure 4.12. Before going through the details of R_g , R_h and M_w , it is worthy to explain that how these parameters are extracted from light scattering data. The representation of $Kc/\Delta R$ versus q^2 for this measurements is displayed in Figure 4.10 to demonstrate how a Guinier plot with linear fit is used to yield the parameters R_g and M_w . The plots are selected only at 4 different times of TR-SLS/DLS measurements to be shown here while this calculation is done 300 times to cover the entire measurements including 300 runs. The same procedure has been already done for the case of aggregation with $CaCl_2$.

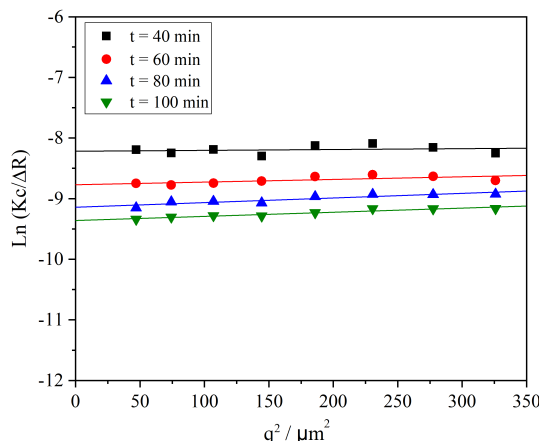


Figure 4.10. Representation of $Kc/\Delta R$ versus q^2 for yellow dyestuff solution where the aggregation is induced by a stepwise addition of HCl to 4 ml of 1 mmol.L^{-1} yellow dyestuff solution. The plots are selected at 4 different times of each measurement.

Correspondingly, Figure 4.11 shows how the cumulant method is applied to the same selected measurements representing the plot of D_z versus q^2 . As is mentioned in 4.1 the intercept of this fit is used to obtain the hydrodynamic radius R_h from Equation 2.20.

After performing the all steps explained in Figures 4.10 and 4.11 for the entire measurements (300 runs), radius of gyration R_g , molecular weight M_w and hydrodynamic radius R_h of aggregated yellow dyestuff are obtained. This parameters are plotted in

Figures 4.12 where the aggregation process is started after mixing 1 mmol.L^{-1} yellow solution with HCl. The M_w value in the beginning of aggregation process is almost 4 times larger than the molecular weight of a single monomer ($236.45 \text{ g.mol}^{-1}$). pH of dye solution before and after mixing with HCl is measured as 11.8ss and 8.1 respectively.

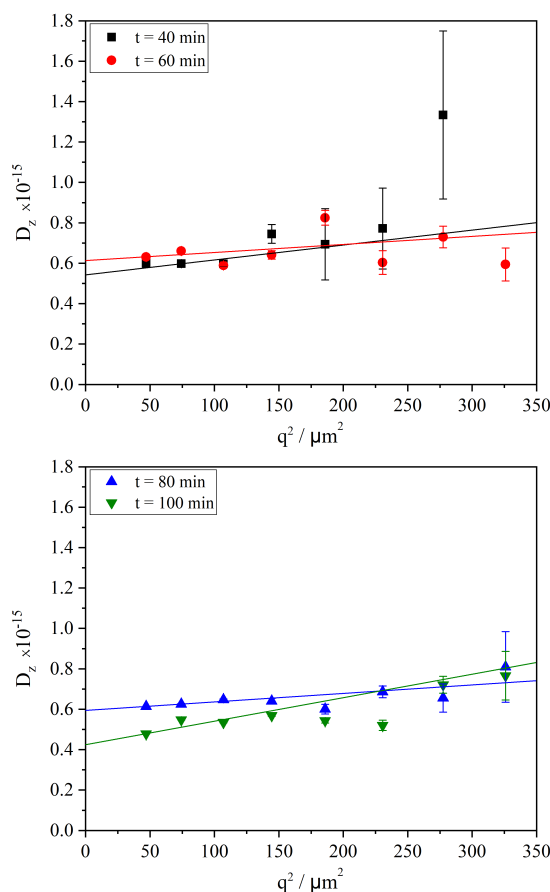


Figure 4.11. Plot of D_z versus q^2 for a yellow dyestuff solution where aggregation is induced by a stepwise addition of HCl to 4 ml of 1 mmol.L^{-1} yellow dyestuff solution. The plots are selected at 4 different times of each measurement. A linear fit yields the D_0 as the intercept which can be inserted in the Equation 2.20 giving the hydrodynamic radius R_h .

It can be seen that the particles grow with different speed during the steps of adding acid. During the first 20 minutes after adding HCl, the molecular weight and radius of gyration increase. Adding HCl could be continued to promote the aggregation process yielding larger molecular weight but it is omitted after the fourth step of addition. This is necessary to continue angular dependent SLS measurement. The very large size of particles remove the possibility of determining the intercept from $Kc/\Delta R$.

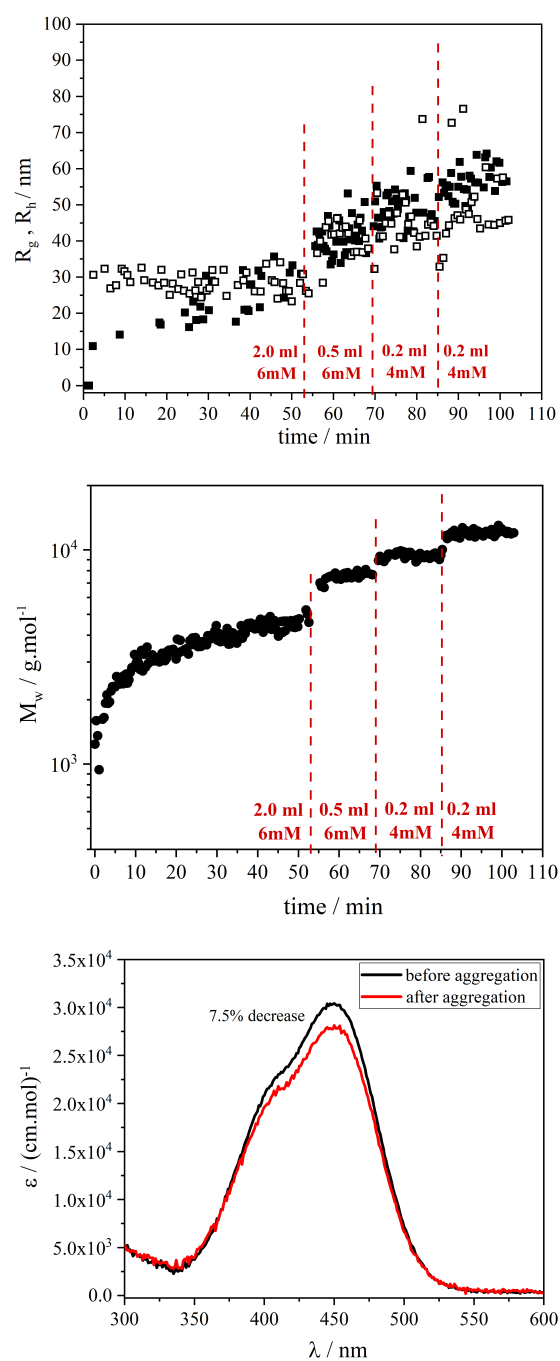


Figure 4.12. Radius of gyration (■), hydrodynamic radius (□) and molecular weight (●) of aggregated yellow dyestuff. The aggregation is induced by a stepwise addition of HCl to 4 ml of $1\text{mmol}\cdot\text{L}^{-1}$ yellow dyestuff solution. Molar extinction represents the solution state after the final step of adding HCl.

In order to get further information on the structure of the particles we may have a look at the correlation of the particle size R_g with the weight-averaged molar mass M_w . By eliminating the aggregation time, we can establish a power law and determine the shape sensitive exponent α for self-similar structures as is shown in Figure 4.13. Due to the stepwise addition of HCl, a continuous correlation of R_g and M_w may not provide further information so the data are represented as the average of last 10 data points of R_g and M_w at each step of adding HCl.

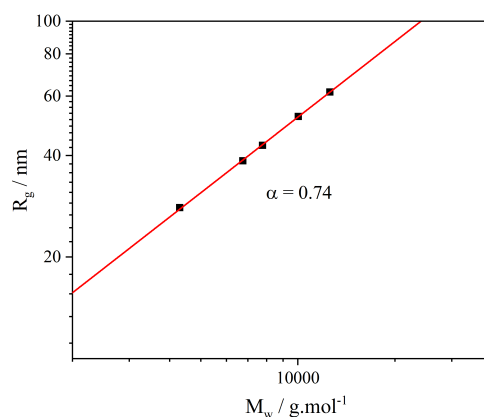


Figure 4.13. Correlation of the radius of gyration R_g with the weight-averaged molar mass M_w for aggregated yellow dyestuff in PL1OH. The data are represented as the average of last 10 data points of R_g and M_w at each step of adding HCl to 4ml of the 1mmol.L^{-1} yellow dyestuff solution.

The value $\alpha = 0.74$ falls between 1 and $1/2$. Hence, the following alternatives can be discussed: (i) In case of the step growth process i.e. any particle reacts with any other particle in solution, exponents α directly corresponds to a lower limit of $\alpha = 1/3$ suggesting the structure of a sphere and the upper limit of $\alpha = 1$ suggesting the rod-like particles. Correspondingly, the $\alpha = 1/2$ is assigned to a fractal-like structure comparable to that of a polymer coil [95]. (ii) Monomer addition dominates the aggregation process, i.e. the weight-averaged molar mass of aggregated particles M_w describes an average of a bimodal ensemble of monomers and growing particles if the entire dyestuff concentration c_0 corresponding to the concentration at $t = 0$ is used for the calculation only. The resulting α exponent is decreased by a factor of $1/2$. Accordingly, compact spherical structures formed in a monomer addition process adopt an exponent of $\alpha = 1/6$, $\alpha = 1/4$ represents a fractal-like structure and $\alpha = 1/2$ corresponds to the rod-like particle.

The molar extinction plotted in Figures 4.12 provides the monomer concentration at the end of aggregation process c_{mon} which enables us to calculate the concentration of

aggregated particles c_{agg} according to Equation 4.2:

$$c_{agg} = c_0 - c_{mon} \quad (4.2)$$

From c_{agg} an additional weight-averaged mass for the aggregated particles M_{agg} can be calculated as:

$$\begin{aligned} M_{agg} &= \Delta R_{\theta=0} / K c_{agg} \\ c_{agg} &= \frac{7.5}{100} c_0 \\ M_{agg} &= \frac{100}{7.5} M_w = 1.06 \times 10^5 \text{ g/mol} \end{aligned} \quad (4.3)$$

The calculated molecular weight from UV-vis spectra M_{agg} is almost 9 times larger than M_w which gives us a hint to assign an ensemble of monomer and aggregates to M_w .

Considering a monomer addition process, $\alpha = 0.74$ does not fit into the regime of theoretically defined exponents, although the measured form factor votes for rather compact structures like spheres. The formfactor of the particles is plotted in Figure 4.14 in an angular range of $20 \leq \theta \leq 120$. The scattering behavior of the yellow aggregates can be described approximately by the form factor of the spheres, although three theoretical lines are so close to each other due to the small size of particles. It must be mentioned that the measured values from SLS ($R_g = 61 \text{ nm}$, $R_h = 46.01 \text{ nm}$ and $M_w = 14000 \text{ g/mol}$) are in a good agreement with the final values of TR-SLS/DLS. The final measured values of M_w , R_g , R_h and monomer consumption at the end of aggregation process are listed in Table 4.3.

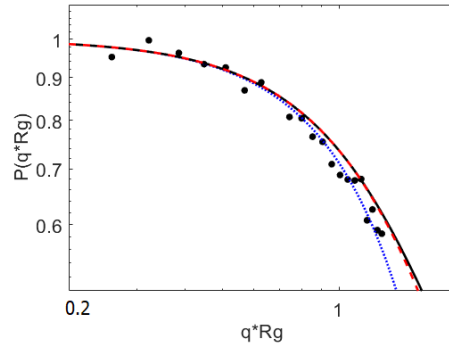


Figure 4.14. Plot of the form factor $P(q.R_g)$ versus $q.R_g$ measured after mixing 4 ml of 1 mmol.L^{-1} yellow dyestuff solution to the 2.9 ml of 8 mM HCl. The measurement is performed in an angular range of $20^\circ \leq \theta \leq 120^\circ$. The experimental data \bullet is compared to the theoretical scattering curves of a rod (—), Gaussian coil (---) and hard spheres (...)

Table 4.3. The final values of R_g , R_h and M_w of aggregated particles measured from TR-SLS/DLS after mixing HCl with 4ml of 1mmol.L^{-1} yellow dyestuff in PL1OH. M_{agg} is calculated from Equation 4.2.

initial c_{dye} [mol/L]	final R_g [nm]	final R_h [nm]	final M_w [g/mol]	M_{agg} [g/mol]	α	ρ	pH of mixture
1×10^{-3}	59.7	49.2	1.2×10^4	1.06×10^5	0.74	1.25	8.1

4.2.2 Red Dyestuff Aggregation Induced by Lowering the pH

The red dyestuffs in PL1OH shows the same tendency as yellow to form aggregates if it is exposed to the hydrochloric acid as an initiator agent. It has been studied in PL1OH solvent at two initial dyestuff concentrations of 0.2mmol.L^{-1} and 0.8mmol.L^{-1} . Again the acid was added step by step triggering an instant growth of the particles. The initial and final pH of samples are listed in Table 4.4.

Table 4.4. Information of the samples before and after performing the measurements.

initial c_{dye} [mol/L]	final c_{dye} [mol/L]	initial pH	final pH
0.2×10^{-3}	0.12×10^{-3}	12.08	7.83
0.8×10^{-3}	0.50×10^{-3}	12.00	7.74

Before going through the details of R_g , R_h and M_w , it is worthy to explain that how these parameters are extracted from light scattering data. The representation of $Kc/\Delta R$ versus q^2 for this measurements is displayed in Figure 4.15 to demonstrate how a Guinier plot with linear fit is used to yield the parameters R_g and M_w . The plots are selected only at 4 different times of TR-SLS/DLS measurements to be shown here while this calculation is done 300 times to cover the entire measurements including 300 runs. The same procedure has been already done for the case of aggregation with CaCl_2 .

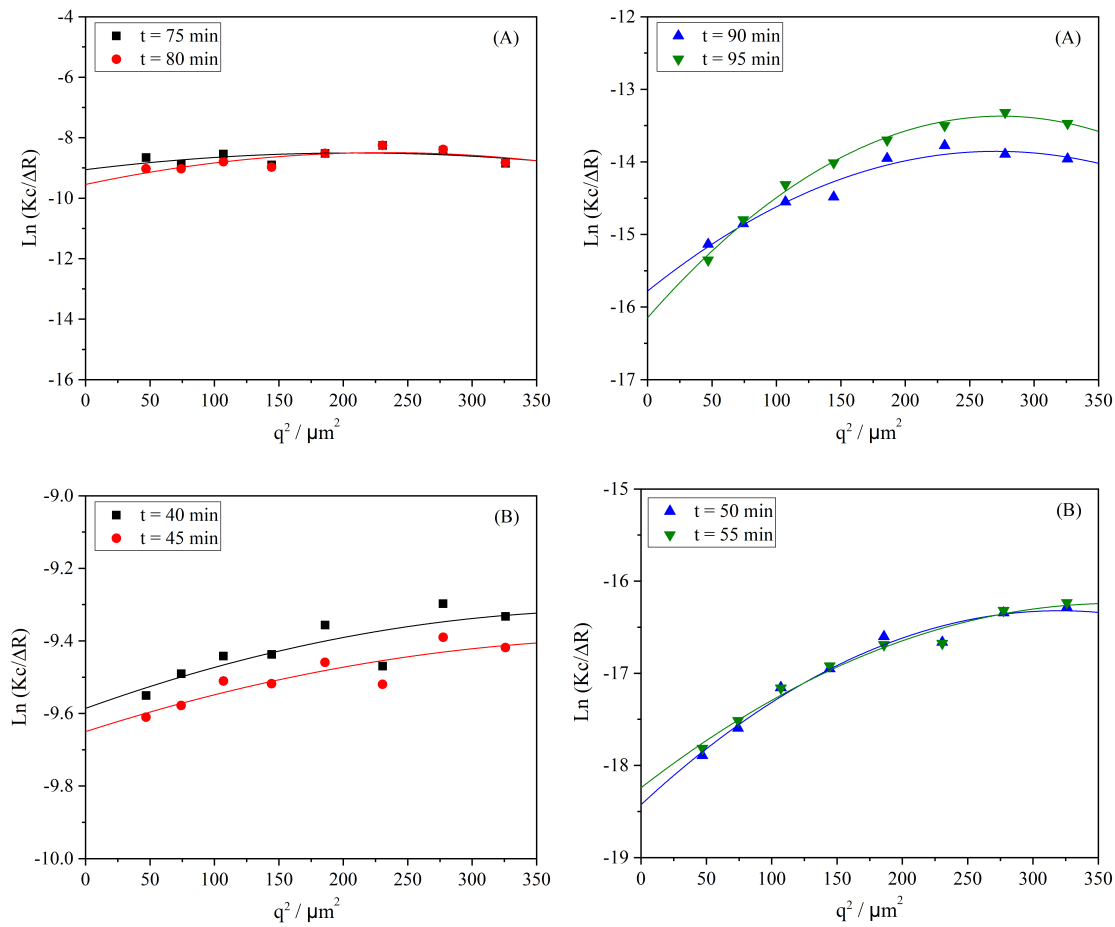


Figure 4.15. Representation of $Kc/\Delta R$ versus q^2 for a red dyestuff solution where the aggregation is induced by a stepwise addition of HCl to 4 ml of (A) 0.2mmol.L^{-1} and (B) 0.8mmol.L^{-1} red dyestuff solution. The plots represent at 4 different times of each concentration.

Figure 4.16 shows how the cumulant method is applied for the same selected measurements fitting the plot of D_z versus q^2 . As is mentioned in 4.1 the intercept of this fit is used to obtain the hydrodynamic value R_h from Equation 2.20.

After performing the steps explained in Figures 4.15 and 4.16 for the entire measurements (300 runs), radius of gyration R_g , molecular weight M_w and hydrodynamic radius R_h of aggregated red dyestuff are obtained. This parameters are plotted in Figures 4.17 and 4.18 where the aggregation process is started after mixing 0.1mmol.L^{-1} and 0.2mmol.L^{-1} red solution with HCl.

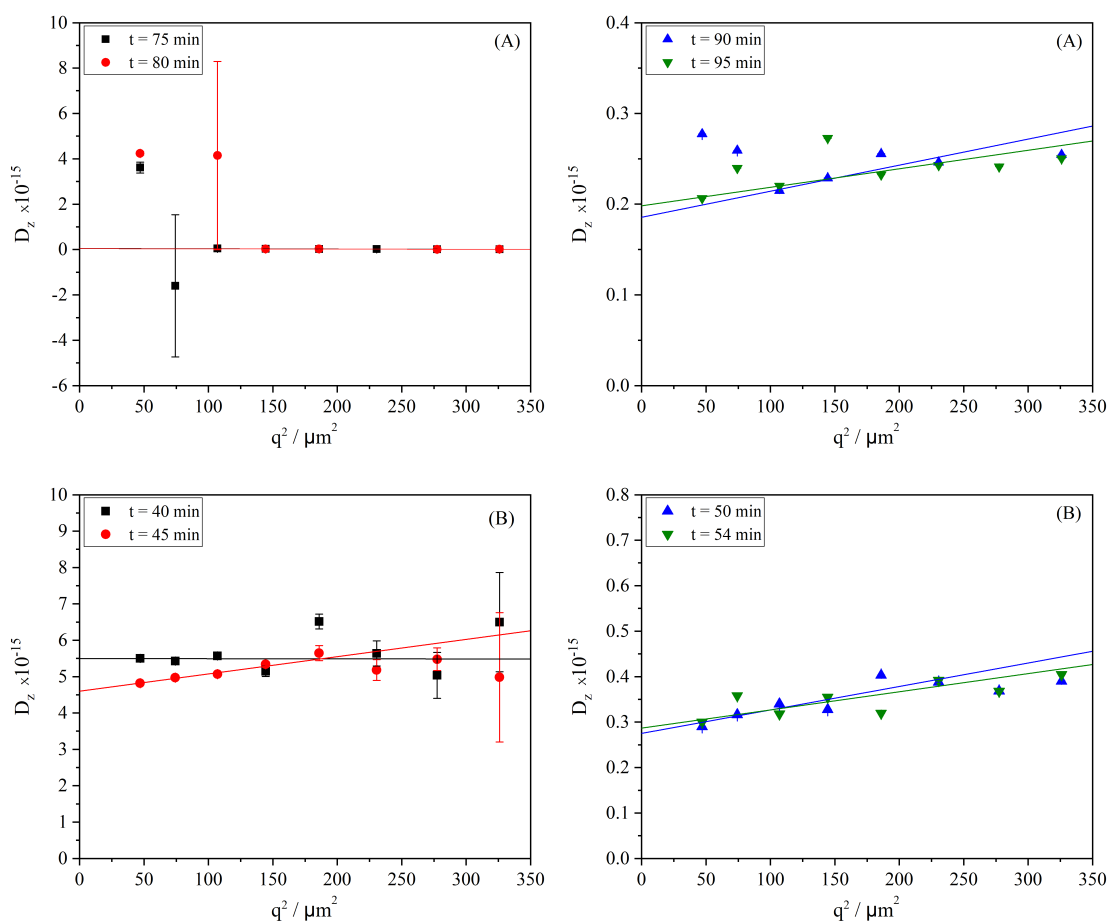


Figure 4.16. Plot of D_z versus q^2 for a red dyestuff solution where the aggregation is induced by a stepwise addition of HCl to 4 ml of (A) 0.2mmol.L^{-1} and (B) 0.8mmol.L^{-1} red dyestuff solution. The plots represent at 4 different times of each concentration. A linear fit yields the D_0 as the intercept which can be inserted in the Equation 2.20 giving the hydrodynamic radius R_h .

Figures 4.17 and 4.18 represent the radius of gyration R_g , hydrodynamic radius R_h and weight-averaged molar mass M_w of aggregated red dyestuff at each concentrations. The monomer consumption is measured right after the last step of the aggregation process via UV-vis spectroscopy.

In general, It can be seen that with increasing the initial dyestuff concentration, a larger M_w of aggregated particles is achieved. The onset of aggregation process in the measurement of 0.8mmol.L^{-1} is slower than 0.2mmol.L^{-1} which may stem from the weaker acid in the first step of measurement.

Progress of the aggregation results in a very large values for radii as they reach an average close to $R_g \sim 200 - 240 \text{ nm}$ and $R_h \sim 1000 - 1100 \text{ nm}$ not comparing with each other anymore. This discrepancy can be explained by the underestimation of R_g values. By increasing the particle size the Guinier regime is shifted toward lower q as the light scattering data is based on a fixed q -range. Consequently the Guinier regime may gradually leave the q -range accessible by the instrument. Apparently this shift begins to have an influence once R_g gets close to 200 nm . As can be seen from Figure 4.17 and Figure 4.18, R_h increases more pronounced with time than R_g . Therefore, establishing a correlation of final size R_g and mass M_w is not possible except in a limited time frame of $27 \text{ min} \leq t \leq 47 \text{ min}$ of the second-

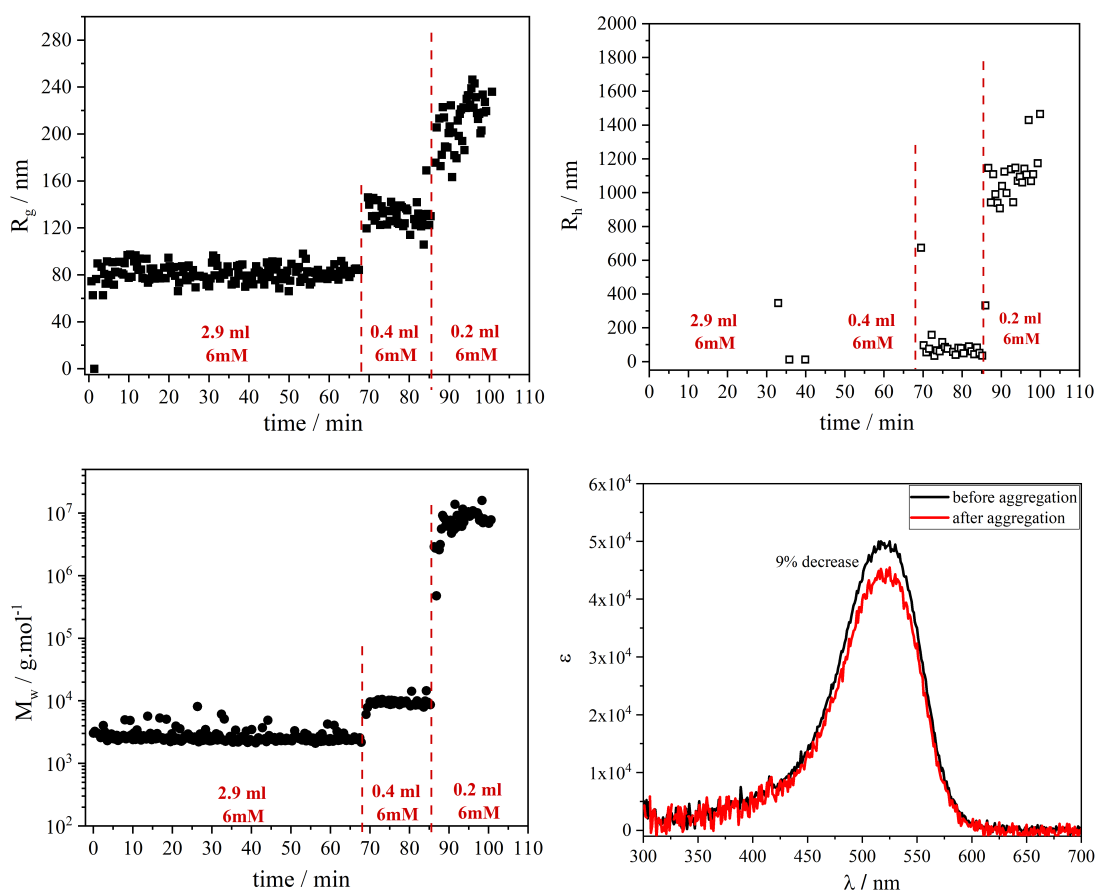


Figure 4.17. Radius of gyration (■), hydrodynamic radius (□) and molecular weight (●) of aggregated red dyestuff as a function of time in PL1OH. The aggregation is induced by a stepwise addition of HCl to 4 ml of 0.2 mmol.L^{-1} red dyestuff solution. The molar extinction coefficient ϵ enables estimation of the amount of consumed monomers after the final step of measurement.

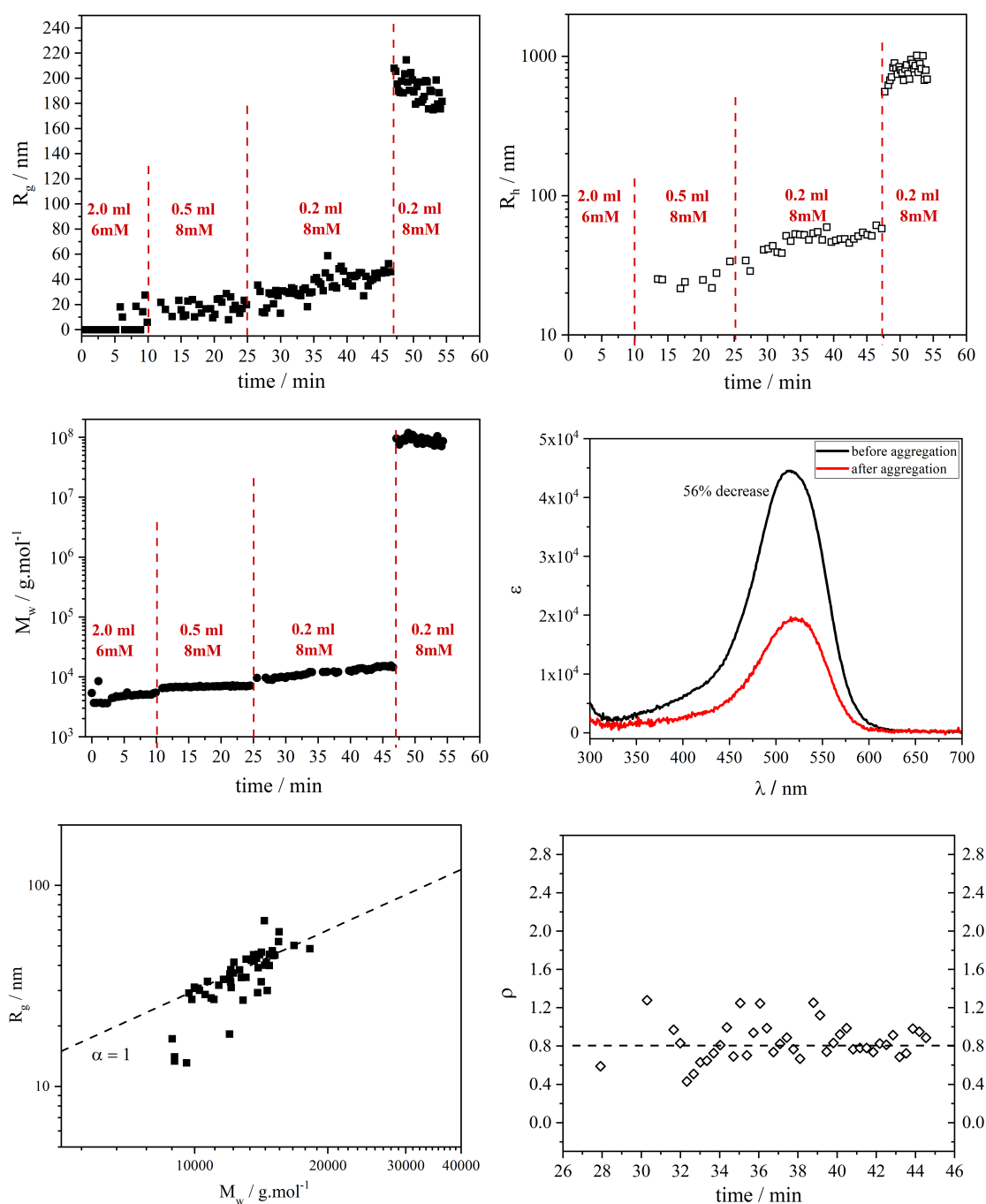


Figure 4.18. Radius of gyration (■), hydrodynamic radius (□) and molecular weight (●) of aggregated red dyestuff as a function of time in PL10H. The aggregation is induced by a stepwise addition of HCl to 4 ml of 0.8 mmol.L⁻¹ red dyestuff solution. Power law is established for a range of time 27 min ≤ t ≤ 47 min. Evolution of the ρ ratio is also shown during the last step of aggregation process. The molar extinction coefficient ϵ enables an estimation of the amount of consumed monomers in the final step of measurement.

-measurement which is displayed in Figure 4.18. At this time frame when the third step of HCl is added to the dye solution, R_g is still in Guinier regime and comparable to R_h so the power law and ρ ratio is meaningful. Correlation of R_g and M_w at this time adopts the value of $\alpha = 1$ which can refer to the case of rod-like particles if the growth occurs according to a step-growth process. But the shape sensitive factor ρ rather votes for the formation of compact particles than rods.

Table 4.5 gives an overview on the final measured values from each measurement. Since the equilibrium states have been reached in both measurements, all final values for M_w are corrected based on Equation 4.2 and 4.3. Again it can be seen that the calculated molecular weight M_{agg} in the first measurement is 10 times and in the second one is almost 2 times larger than the receptive M_w . Therefore the possibility of a bimodal ensemble of monomers and growing particles can be considered.

Additional insight is provided by a closer look at the particle scattering curves of the sample with initial concentration of 0.2 mmol.L^{-1} . As is shown in Figure 4.19, the scattering curve almost coincides with the theoretical curve of sphere in the low q -range. Going towards the larger angles, there is a deviation from the sphere curve although it still lies below the curve of a Gaussian model coil. This deviation might result from a certain degree of polydispersity. Contrary to this interpretation, a minimum within the high q -range is visible which is characteristic for monodisperse spheres if the particles are large enough.

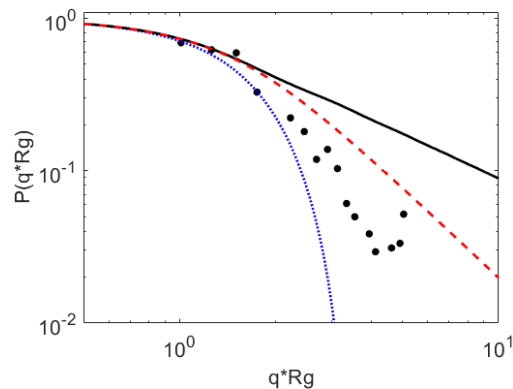


Figure 4.19. Plot of the form factor $P(q.R_g)$ versus $q.R_g$ measured after mixing 4 ml of 0.2 mmol.L^{-1} red dyestuff solution to the 3.5 ml of 6 mM HCl. The measurement is performed in an angular range of $20^\circ \leq \theta \leq 120^\circ$. R_g and M_w are calculated as 223 nm and $1.07 \times 10^7 \text{ g/mol}$. The experimental data \bullet is compared to the theoretical scattering curves of a rod (—), Gaussian coil (---) and hard spheres (...).

Table 4.5. The final values of R_h , R_g and M_w of aggregated particles after mixing HCl with red dyestuff solution in PL1OH. M_{agg} is calculated from Equation 4.2 and 4.3.

initial c_{dye} [mol/L]	final R_g [nm]	final R_h [nm]	final M_w [g/mol]	M_{agg} [g/mol]
0.2×10^{-3}	233.71	1076.51	0.9×10^7	10.0×10^7
0.8×10^{-3}	191.2	1008.98	8.9×10^7	15.9×10^7

5

CHAPTER

Summary

The present study investigated the aggregation of acidic dyestuffs yellow, blue and red via time-resolved static and dynamic light scattering in combination with UV-vis spectrometry. Experiments were carried out at 25°C in pure water and 5% ammonia and in the presence of different salts trying to keep the pH of final solution above 10. Two solvents as PL1Cl with 1% NH_4Cl and PL2P with 1% Na_2HPO_4 have been considered as reference solvents to dissolve the rainbow dyestuffs. Unlike the yellow dyestuff, blue and red solutions exhibited a meta-stable behavior in PL1Cl although none of them show meta-stability in PL2P except the red dyestuff. The UV-vis spectroscopy in the wavelength range of $300\text{ nm} \leq \lambda \leq 800\text{ nm}$ revealed a fair solubility for yellow dyestuff in PL1Cl while PL1Cl was a poor solvent for red and blue.

On the other hand, PL2P provided a good solubility for all three dyestuffs. The reason might be explained by the fact that disodium phosphate Na_2HPO_4 is moderately basic so it increases the pH of PL2P solvent resulting in a better solubility in comparison to the PL1Cl. Observation of a blue shifted absorption peak in the spectra of red and blue dyestuffs may declare the formation of H-aggregates in blue and red solutions.

In the next step, the reference solvents were modified by adding benzyl alcohol, isopropanol and guanidine sulphate. It was found that benzyl alcohol and isopropanol enhance the solubility of dyestuffs while the guanidine sulphate has an opposite effect. Another modification has been done by introducing the different salts from Hofmeister series in the reference solvents as they can change the solubility of dyestuffs significantly. Again the meta-stable behavior has been recognized in red and blue solutions.

Considering different anions, the highest solubility of yellow dyestuff was achieved in the presence of sulphate and the lowest solubility was related to the chloride. Regardless of the close competition between anions increasing the solubility limit, a good stability was observed up to 24 hours in the yellow solutions. In the case of sulphate, an extra measurement was done after 4 days to show the stability of solution at higher age. The effects of different cations on the solubility of yellow dyestuff was comparable. The solubility of guanidinium, potassium and sodium was so close while ammonium has shown the lowest solubility. The all four solutions were stable after 24 hours. The following orders has been found for the power of anions and cations increasing the solubility limit of yellow dyestuff in terms of c_{sat} :

$$SO_4^{2-} > HPO_4^{2-} > I^- > Cl^- \quad ; \quad Gn > K^+ \approx Na^+ > NH_4^+ > Ca^{2+}.$$

Due to meta-stable solutions of blue and red dyestuffs, a second classification can be assigned to the effect of anions and cations increasing the solubility limit of blue and red dyestuff in the meta stable state where the highest solubility of both dyestuffs was resulted from potassium.

A blue shift has been observed for the mentioned dyestuff solutions in all different solvents. As was discussed, the blue shifted absorption peak in water mixtures may be caused by the existence of H-aggregates where the dye molecules aggregate in a plane to plane way to form oligomers. In case of blue dyestuff, the appearance of isosbestic point in some solvents as $PL1HPO_4$, $PL1SO_4$, $PL1K$ and $PL1I$ is a proof for the existence of two species.

Based on increasing the solubility of dyestuff in meta stable and saturated state, the following orders can be derived for the effect of anions and cations on the dyestuffs:

meta stable state for blue dyestuff:

$$I^- > HPO_4^{2-} > SO_4^{2-} \approx Cl^- \quad ; \quad K^+ > Na^+ > NH_4^+ > Gn > Ca^{2+}.$$

saturated state for blue dyestuff:

$$I^- > SO_4^{2-} > HPO_4^{2-} > Cl^- \quad ; \quad Na^+ > NH_4^+ > K^+ > Gn > Ca^{2+}.$$

meta stable state for red dyestuff:

$$Cl^- > HPO_4^{2-} \approx SO_4^{2-} \approx I^- \quad ; \quad K^+ > Na^+ \approx NH_4^+ > Gn > Ca^{2+}.$$

and saturated state for red dyestuff:



From the comparison of this results with Hofmeister series, it can be seen that Ca^{2+} is playing the same role decreasing the solubility of all three dyestuffs as it has played in the case of proteins. Guanidinium also has shown the same effect as Hofmeister series for blue and red dyestuffs while in case of yellow dyestuff it has completely the opposite effect.

Among anions, the effect of iodide is quit interesting as it opposes the order of Hofmeister series by increasing the solubility in both meta-stable and saturated states of yellow and blue dyestuffs. In the case of red dyestuff our finding about iodide is in a agreement with Hofmeister series. In case of yellow dyestuff and of the saturated state of two other dyestuffs, SO_4^{2-} could satisfy the order of Hofmeister series which is also in agreement with the results of Fedoseeva et al. in 2010 [42] when they investigated the effect of Hofmeister series anions on the aggregation/solubility of Malachite green (MG) in aqueous solution.

With these results from UV-vis spectroscopy measurements the appropriate agent was selected in order to initiate the aggregation process. Accordingly, $CaCl_2$ was the suitable candidate to trigger the aggregation of dyestuffs. Combined time-resolved SLS/DLS experiments make available three types of refined data: (i) the exponents α retrieved from plots of radii of gyration versus weight averaged particle mass of the growing particles leading to the information on the mechanism of particle growth and on the morphology of the growing particles; (ii) the ratio of R_g and R_h providing information on the morphology of the growing particles; (iii) the formfactor giving more insight into the structure of aggregated particles. Mixing the aqueous $CaCl_2$ to the yellow and red dye solutions resulted in the particles with a small weight averaged molecular weights. A UV-Vis spectroscopy measurement explained the low molecular weight of created particle as the most of dye molecules are still in monomeric state not participating in the aggregation process.

The size-mass correlation for aggregated yellow particles initiated by $CaCl_2$ followed a power law for self-similar sphere like structures formed in a monomer addition mechanism. This view was further supported by the ρ -value of ≈ 0.71 . Consideration of the formfactors $P(q)$ of the particles, which was taken right after the time-resolved light scattering measurements confirmed the formation of rather compact structure.

The correlation between particle size and mass for aggregated red particles also describes the same results as yellow dyestuff. It assigns the formation of compact particles with a rather homogeneous density which are created during a monomer addition process. This assumption is further supported by ρ -values which are measured in the range of

0.6 – 0.76. This was also supported by the formfactor analysis, which revealed curves falling between the curve of a compact sphere and a fractal-like particle like the one corresponding to polymer coils.

Since the solubility of dyestuff in solution was strongly dependent on the pH values, the hydrochloric acid was considered as a second aggregation agent. As the process was accomplished quickly, the acid was added gradually (step by step) to the yellow and red dye solutions. The $R_g = 60\text{ nm}$ and $R_h = 50\text{ nm}$ are measured for yellow dyestuff and $R_g = 191 - 234\text{ nm}$ and $R_h = 1008 - 1077\text{ nm}$ are measured for red dyestuff.

Unlike the case of CaCl_2 , HCl could trigger the formation of large particles with a high molecular weights. The UV-vis spectroscopy right after the last step of aggregation reveals the consumption of monomers clearly. In case of yellow dyestuff, the exponent of power law $\alpha = 0.74$ falls between 1 and $1/2$ which brings two possibilities of growth processes before we make a decision about the shape of aggregated particles: (i) the step growth process with a lower limit of $\alpha = 1/3$ and the upper limit of $\alpha = 1$. (ii) the monomer addition process in which the weight-averaged molar mass of aggregated particles M_w describes an average of a bimodal ensemble of monomers and growing particles if the entire dyestuff concentration c_0 corresponding to the concentration at $t = 0$ is used for the calculation only. Then the exponents accept a lower limit of $\alpha = 1/6$ and the upper limit of $\alpha = 1/2$. In our measurements the UV-vis spectroscopy acts as a helpful tool to calculate the consumed monomers, thereby obtaining the actual molecular weight of aggregated particles M_{agg} which is almost 9 times larger than M_w giving a hint to assign an ensemble of monomer-aggregates to our system. Considering a monomer addition process, $\alpha = 0.74$ does not fit to the regime of theoretically defined exponents, although the measured form factor votes for rather compact structures like spheres.

In the case of red dyestuff aggregation initiated by HCl, the R_g and R_h are not comparing anymore due to the large values of $R_g = 200\text{ nm}$ where the Guinier regime ($q \cdot R_g < 1$) is not valid anymore. The measured form factor coincides with the theoretical curve of sphere in the low q -range. Going towards the larger angles, there is a deviation from the sphere curve although it still lies below the curve of a Gaussian model coil. The calculated values for M_{agg} are larger than M_w approving again the possibility of a bimodal system.

6

CHAPTER

Appendix I

Data evaluation for static and dynamic light scattering measurements: The measurement program generates two types of files. The first file contains all measurement points with relevant data such as the time (t), the averaged count rates (CR) and the laser intensity (I). In addition, a file is generated for each measuring point, which contains the correlation functions of dynamic light scattering ($g^2(\tau)$) and progress of the count rate over time. Within the scope of this work, a suitable program to visualize the data, and to evaluate it routinely and appropriately is written on the basis of MATLAB by Benjamin Hämisch. The interface will be explained through an example in more detail below.

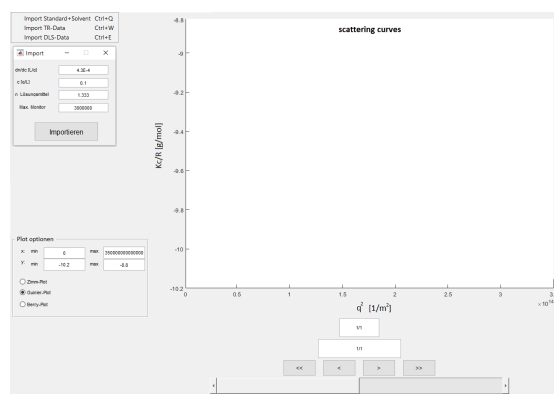


Figure 6.1. Start menu of the Matlab interface written by Benjamin Hämisch, used for TR-SLS data evaluation at the present work.

Figure 6.1 shows the start menu of the interface. This is where the data is imported and an initial visualization of the scattering curves takes place. Options for data import are available on the left-hand side, while the imported data is visualized on the right-hand side. Four files are required for the import, which must first be created. The first file contains the angles that were measured. In addition, a text file is needed for the scattering intensities of the standard toluene and the solvent. Finally, the file is required which contains the data points of the time-dependent measurement. This is characterized by the filename extension ".LST". Once all the required files have been selected, the import can be started using the "Import" button.

As is shown in the core code of the import, first the time and the laser intensities are saved in a separate matrix. The time is displayed in minutes or seconds, depending on the set mode. In the next step, some data which are not required like temperature or the starting angle, are deleted from the matrix. Then the normalized scattering intensities are calculated. With these values $Kc/\Delta R_\theta$ can now be determined. In general, the program uses the laser intensity to check which standard and solvent values are required for the calculation according to Equation 2.6. These are then saved in a temporary matrix in order to generate the corresponding $Kc/\Delta R_\theta$ values. Then the temporary matrix is overwritten for the next data point.

```

%% Import the data from raw file
%% Save Imon, time, temperature and calculate viscosity based on T
handles.mw.SLS.t(:,1) = handles.mw.SLS.raw(:,1)./60;
handles.mw.DLS.T = handles.mw.SLS.raw(:,11)-273.15;
handles.mw.SLS.RR = handles.mw.DLS.T.*3.544E-7+1.279E-4;
handles.mw.DLS.eta = (1.38704.*exp(-handles.mw.DLS.T./24.4419)+0.38825)*1E-3;
handles.mw.SLS.Imon(:,1) = handles.mw.SLS.raw(:,12);
%% Calculation of Attenuator Setting
handles.mw.SLS.Att = (handles.mw.SLS.Imon(:,1)/handles.mw.SLS.max_Imon)*100;
roundTargets = [0.1 0.31 1 3.1 10 31 100];
handles.mw.SLS.Att = interp1(roundTargets,roundTargets,handles.mw.SLS.Att,'nearest');
handles.mw.SLS.Att(isnan(handles.mw.SLS.Att))=0.1;
%% Get rid of data
handles.mw.SLS.raw(:,11:12) = [];
handles.mw.SLS.raw(:,1:2) = [];
handles.mw.SLS.Anzahl = size(handles.mw.SLS.raw,1);
handles.mw.SLS.CR = transpose(fliplr(handles.mw.SLS.raw)); %transpose and flip data
%% Calculation of scattering ratio
for c=1:1:handles.mw.SLS.Anzahl
    handles.mw.SLS.rSample(:,c)= (handles.mw.SLS.CR(:,c)-handles.mw.SLS.DC).*handles.mw.SLS.RelSens...
        .*sin(deg2rad(handles.mw.SLS.Winkel(:,1)))...
        ./handles.mw.SLS.Imon(c);
end
%% Calculation of Kc/R
for c=1:1:handles.mw.SLS.Anzahl
    switch handles.mw.SLS.Att(c)
        case 100
            temp_LM = handles.mw.SLS.rLm(2:9,2);
            temp_Standard = handles.mw.SLS.rStd(2:9,2);
        case 31
            temp_LM = handles.mw.SLS.rLm(2:9,3);
    end
end

```

```

temp_Standard = handles.mw.SLS.rStd(2:9,3);
case 10
temp_LM = handles.mw.SLS.rLm(2:9,3);
temp_Standard = handles.mw.SLS.rStd(2:9,4);
case 3.1
temp_LM = handles.mw.SLS.rLm(2:9,5);
temp_Standard = handles.mw.SLS.rStd(2:9,5);
case 1
temp_LM = handles.mw.SLS.rLm(2:9,6);
temp_Standard = handles.mw.SLS.rStd(2:9,6);
case 0.31
temp_LM = handles.mw.SLS.rLm(2:9,7);
temp_Standard = handles.mw.SLS.rStd(2:9,7);
case 0.1
temp_LM = handles.mw.SLS.rLm(2:9,8);
temp_Standard = handles.mw.SLS.rStd(2:9,8);
end
handles.mw.SLS.KcR{1,1}(:,c)=(handles.mw.SLS.K*handles.mw.SLS.c)./(handles.mw.SLS.RR(c)
).* (handles.mw.SLS.rSample(:,c)-temp_LM)./temp_Standard);
end
handles.mw.SLS.KcR{2,1} = sqrt(handles.mw.SLS.KcR{1,1});
handles.mw.SLS.KcR{3,1} = log(handles.mw.SLS.KcR{1,1});
for k=1:handles.mw.SLS.Anzahl
handles.mw.DLS.CRN{k}(:,2:9)=handles.mw.DLS.CR{k}(:,2:9)./handles.mw.SLS.Imon(k);
end

```

In the next step, the scattering curves can be evaluated depending on the generated data. Various tools are available for this, which can be seen in Figure 6.2. The example is selected as the time-resolved measurement of 1 mmol.L^{-1} yellow dyestuff aggregated by addition of 2 ml CaCl_2 in the concentrations of 1.8 mmol.L^{-1} (the blue data points ▲ in Figure 4.3).

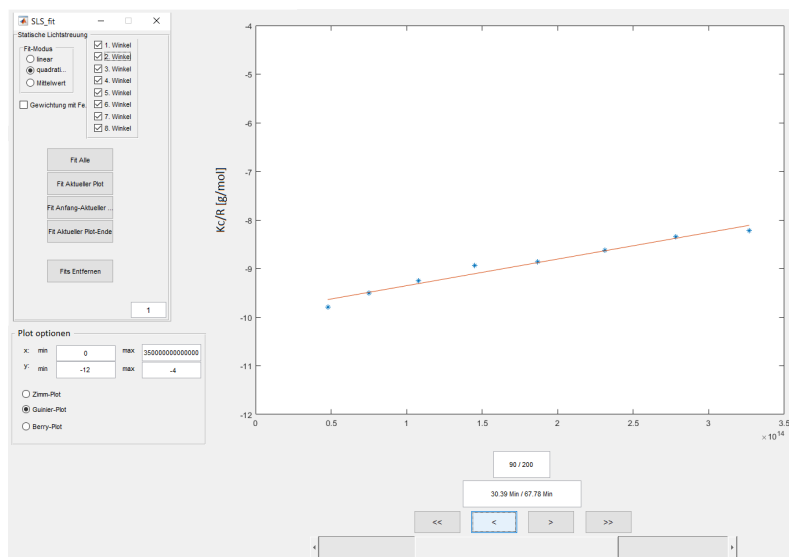


Figure 6.2. Overview of the fit program for static light scattering (linear fit on the Guinier plot).

Here we can set which type of plot can be used for the fit procedure. The choices are Zimm, Berry and Guinier plot. A linear or quadratic fit can also be selected. If it was set at the beginning that the mean value should be formed from three successive measuring points, then the fit can be weighted with the respective error. Finally, we can set which angles should be used for the fit. If the desired fit parameters are set, then we can select whether all scatter curves should be fitted according to this fit or only the current scatter curve.

The fitted data and fitting parameters are saved in a matrix as is shown in Figure 6.4. The plot mode is saved in the first column, number 3 represents the Guinier plot (the numbers 1 and 2 would refer to Zimm and Berry plots respectively). The type of regression is recorded in the second column, where 1 stands for linear and 2 for quadratic fit. In the next columns, first the parameters of the regression are saved, followed by the parameter errors. In this example, a linear fit is used for all scattering curves with the Guinier plot. So the parameters will be saved in the order shown in Figure 6.3.

For quadratic Fit: $y = A x^2 + B x + C$

Plot mode	Fit mode	A	B	C	Err(B)	Err(C)
-----------	----------	---	---	---	--------	--------

Figure 6.3. The order of saving parameters after applying a linear fit on the Guinier plot.

	1	2	3	4	5	6	7	8	9
72	3	1	-1.8141e-...	1.2341e-14	-11.0505	6.2121e-16	0.0489	0	
73	3	1	-1.8637e-...	1.2752e-14	-11.1574	9.7257e-16	0.0765	0	
74	3	1	-1.6596e-...	1.1431e-14	-10.9839	8.2589e-16	0.0650	0	
75	3	1	-2.2452e-...	1.3894e-14	-11.1807	8.8718e-16	0.0698	0	
76	3	1	-2.0192e-...	1.3451e-14	-11.1979	8.8213e-16	0.0694	0	
77	3	1	-1.7033e-...	1.2384e-14	-11.1310	1.4911e-15	0.1173	0	
78	3	1	-1.7289e-...	1.2059e-14	-11.1045	1.0765e-15	0.0847	0	
79	3	1	-1.6491e-...	1.1636e-14	-11.0848	1.5334e-15	0.1206	0	
80	3	1	-1.6869e-...	1.1564e-14	-11.0345	8.1024e-16	0.0637	0	
81	3	1	-1.7031e-...	1.1906e-14	-11.1286	1.6525e-15	0.1300	0	
82	3	1	-1.7649e-...	1.2159e-14	-11.1279	1.1572e-15	0.0910	0	
83	3	1	-1.6622e-...	1.1541e-14	-11.0876	1.3138e-15	0.1033	0	
84	3	1	-4.7303e-...	2.5907e-14	-13.0359	3.9602e-15	0.3115	0	
85	3	1	-1.6261e-...	1.1997e-14	-11.2213	2.2894e-15	0.1801	0	
86	3	1	-1.5825e-...	1.1284e-14	-11.0544	9.1956e-16	0.0723	0	
87	3	1	-2.0965e-...	1.3112e-14	-11.1335	7.6801e-16	0.0604	0	
88	3	1	-1.8591e-...	1.2229e-14	-11.1002	1.2039e-15	0.0947	0	
89	3	1	-2.2595e-...	1.3788e-14	-11.2057	1.9337e-15	0.1521	0	

Figure 6.4. An example of the matrix in which the fitting parameters are stored.

Saving the all parameters in the right order is important as program can distinguish

between the various methods during the subsequent evaluation. The matlab code for this step is shown below. Within the for loop, which is responsible for evaluating the scattering curves, there are three "cases" with "if" loops. These loops investigate which plot mode was used, since the equations for calculating M_w and R_g are different for these three plot modes.

```
%% Zimm, Berry and Guinier plots
for i=1:handles.mw.SLS.Anzahl
    switch handles.mw.fSLS.MwRg(i,6)
        case 1
            if handles.mw.fSLS.MwRg(i,2) < 0 | handles.mw.fSLS.MwRg(i,4) < 0
                handles.mw.fSLS.MwRg(i,:) = 0;
            else
                handles.mw.fSLS.MwRg(i,4) = 1/handles.mw.fSLS.MwRg(i,4);
                handles.mw.fSLS.MwRg(i,2) = sqrt(handles.mw.fSLS.MwRg(i,2) .* 3 .* handles
.mw.fSLS.MwRg(i,4)) .* 10^9;
            end
        case 2
            if handles.mw.fSLS.MwRg(i,2) < 0 | handles.mw.fSLS.MwRg(i,4) < 0
                handles.mw.fSLS.MwRg(i,:) = 0;
            else
                handles.mw.fSLS.MwRg(i,4) = 1/(handles.mw.fSLS.MwRg(i,4)^2);
                handles.mw.fSLS.MwRg(i,2) = sqrt(sqrt(handles.mw.fSLS.MwRg(i,4)) .* 6 .*
handles.mw.fSLS.MwRg(i,2)) .* 10^9;
            end
        case 3
            handles.mw.fSLS.MwRg(i,5) = -handles.mw.fSLS.MwRg(i,5);
            if handles.mw.fSLS.MwRg(i,2) < 0 | handles.mw.fSLS.MwRg(i,4) > 0
                handles.mw.fSLS.MwRg(i,:) = 0;
            else
                handles.mw.fSLS.MwRg(i,4) = exp(-handles.mw.fSLS.MwRg(i,4));
                handles.mw.fSLS.MwRg(i,2) = sqrt(handles.mw.fSLS.MwRg(i,2) .* 3) .* 10^9;
            end
    end
end
```

The work area for evaluating the dynamic light scattering data is shown in Figure 6.5. Different displaying modes can be selected on the left-hand side, including the intensity-time correlation function $g^{(2)} - 1$ or the field-time correlation function $g^{(1)}$. Furthermore, the count rate CR can be mapped as well as the calculated diffusion coefficients versus q^2 . The fitting procedure is based on the cumulant method, with a flexible cutoff. Correlation functions of a desired data set can be displayed on the right side.

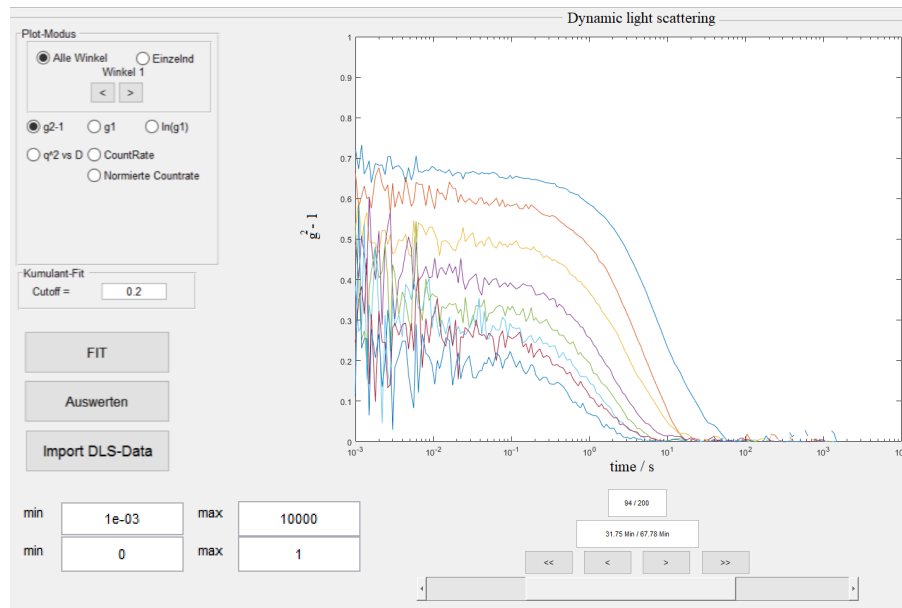


Figure 6.5. Overview of the fit program for dynamic light scattering.

The import of the data for the evaluation of the dynamic light scattering turned out to be not trivial, since not only one file has to be read for all data sets but a separate file for each data set is needed to be read. This would be implemented by the user reading the file of first data record clicking the button "Import DLS-Data". The import runs the files one by one and the running number increases by 1 at each step. However, this type of import is only possible because the data structure follows a fixed pattern. The data records of the correlation functions are always in the same lines within the file. The program code of the actual fit procedure is shown below.

```
%% Cumulant Fit
for k=Start:1:Ende
    k
    Cutoff= mean(handles.DLS.g1{a,k}(26:31,2:9))*handles.fDLS.Cumu.Cutoff;
    handles.fDLS.Cumu.Co(k,:) = Cutoff;
    Cutoff = log(Cutoff);
    for i=2:1:9
        try
            xfit = handles.DLS.ln(g1{1,k}(:,1));
            yfit = handles.DLS.ln(g1{a,k}(:,i)); %Initialisierung der Korrelationsfunktionen
            w(1:size(yfit,1),1) = 1; %für Fit
            outliers = yfit < Cutoff(i-1) | isnan(yfit);
            outliers(1:find(xfit>xMin,1)) = true;
            [z,s] = polyfit3(xfit(~outliers),yfit(~outliers),2,[],w(~outliers));
            handles.fDLS.Cumu.Coeff{k}(i-1,1:3) = z;
            handles.fDLS.Cumu.Coeff{k}(i-1,4:6) = sqrt(diag(inv(s.R)*inv(s.R')))...
                .* s.normr.^2./s.df);
            if a == 2
                handles.fDLS.Cumu.Coeff{k}(i-1,4:6) = handles.fDLS.Cumu.Coeff{k}...
                    (i-1,4:6)./2;
            end
        catch
```

```

        handles.fDLS.Cumu.Coeff{k}(i-1,:) = NaN;
    end
end
%% Fit Gamma vs. q^2
try
    handles.fDLS.Cumu.D{k}(:,1:2) = [-handles.fDLS.Cumu.Coeff{k}(:,2) ./ ...
        handles.SLS.Winkel(:,2) handles.fDLS.Cumu.Coeff{k}(:,4) ./ ...
        handles.SLS.Winkel(:,2)]; % Calc D_app and Err(D_app)
    handles.fDLS.Cumu.gamma{k}(:,1) = -handles.fDLS.Cumu.Coeff{k}(:,2); %gamma
    handles.fDLS.Cumu.gamma{k}(:,2) = handles.fDLS.Cumu.Coeff{k}(:,5); %error
    outliers = isnan(handles.fDLS.Cumu.gamma{k}(:,1)) | handles.fDLS. ...
        Cumu.gamma{k}(:,1)<0 | handles.fDLS.Cumu.gamma{k}(:,2) ./ handles.fDLS. ...
        Cumu.gamma{k}(:,1))>0.1;
    xfit = handles.SLS.Winkel(:,2);
    yfit = handles.fDLS.Cumu.gamma{k}(:,1); % assign y for fit gamma

    % quadratic fit for gamma vs q^2 with intercept = 0;
    [z s] = polyfit3(xfit(~outliers),yfit(~outliers),2,[3]);
    handles.fDLS.Cumu.Dq(k,1:3) = z;
    handles.fDLS.Cumu.Dq(k,4:6) = sqrt(diag(inv(s.R)*inv(s.R'))). ...
        *s.normr.^2./s.df);
    outliersD = isnan(handles.fDLS.Cumu.D{k}(:,1)) | handles.fDLS.Cumu.D{k} ...
        (:,1)<0 | handles.fDLS.Cumu.D{k}(:,2) ./ handles.fDLS.Cumu.D{k}(:,1)>0.1;
    yfit = handles.fDLS.Cumu.D{k}(:,1);
    [z s] = polyfit3(xfit(~outliersD),yfit(~outliersD),1);
    handles.fDLS.Cumu.Dq(k,7:8) = z;
    handles.fDLS.Cumu.Dq(k,9:10) = sqrt(diag(inv(s.R)*inv(s.R'))).* ...
        s.normr.^2./s.df);
catch
    handles.fDLS.Cumu.Dq(k,:) = NaN;
end

```

The process of a fit can be divided into three steps, which are processed within a "for" loop for each run. The first step describes the initialization of the x-values and the calculation of the cutoff for the respective data set. This is followed by another for loop, which now starts all 8 angles using the cumulant method.

To apply the cumulant method, the field-time correlation function $g^{(1)}$ is plotted versus time t as is displayed in Figure 6.6. The slope of each curve provides eight Γ values, thereby yielding the eight values of apparent diffusion coefficient D_z . In the last step, the D_z is plotted versus q^2 (Figure 6.6). Using a linear regression, D_z is extrapolated to $q^2 = 0$ and the diffusion coefficient D_0 is obtained.

Finally hydrodynamic radius R_h can be calculated from Equation 2.20. If this entire process is not possible due to the data situation, for example if the measurement is very noisy, then the script skips the process (the corresponding run would be discarded). The calculated values of R_g , R_h and M_w can then exported from the program.

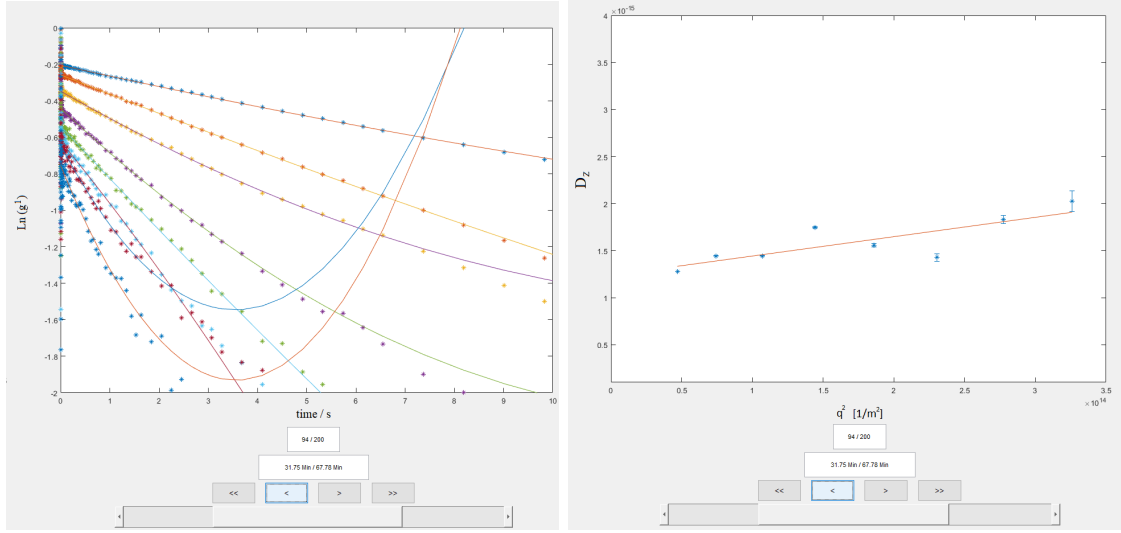


Figure 6.6. (A) Finding the parameter Γ via fitting the plot of $g^{(1)}$ versus time t . (B) Extrapolation of D_z to $q^2 = 0$ via a linear fit (cumulant fit, single mode).

Example of calculation to obtain the SLS and DLS parameters R_g , M_w and R_h for aggregated **yellow** dyestuffs after mixing 4ml of yellow dye solution with 2ml of CaCl_2 . Final concentration of dyestuff in the mixture is $0.67 \text{ /mmol.L}^{-1}$ and CaCl_2 is 0.6 /mmol.L^{-1} . The example is related to the $t = 31 \text{ min}$ (31 minutes after mixing the two components). A Guinier plot with a linear regression is used to fit the SLS data. R_g is calculated from the slope of this plot and the M_w from the intercept.

$$\begin{aligned}
 \ln \frac{Kc}{\Delta R_\theta} &= \ln \frac{1}{M_w} + \frac{(R_g \cdot q)^2}{3} \\
 K &= \frac{4\pi^2 n_{tol}^2}{N_A \lambda_i^2} \left(\frac{dn}{dc} \right)^2 \\
 \pi &= 3.14; \quad n_{tol} = 1.49; \quad N_A = 6.0221409 \times 10^{23}; \quad \lambda_i = 832.5 \text{ nm}; \\
 \frac{dn}{dc} &= 0.4129 \text{ ml.g}^{-1}; \quad c = 0.16 \text{ g/L}; \\
 R_g &= 127.57 \text{ nm}; \quad M_w = 1.02 \times 10^4
 \end{aligned} \tag{6.1}$$

Using a linear regression in Figure 6.6, D_z is extrapolated to $q^2 = 0$ and the diffusion coefficient D_0 is obtained. Hydrodynamic radius R_h can be calculated from Equation

2.20.

$$R_h = \frac{k_B T}{6\pi\eta} \frac{1}{D_0}$$

$$\eta = 8.9 \times 10^{-4}; \quad k_B = 1.3806 \times 10^{-23}; \quad D_0 = 1.24 \times 10^{-15};$$

$$R_h = 197.8 \text{ nm}$$
(6.2)

Calculation of the aggregation number and molecular weight of the aggregated particles based on a given shape. The calculations are done by programming in MATLAB R2018a.

```

1  %%% This code is written by Kate Doostdar (Feb 2019)
2  %to calculate the molecular weight based on the
3  %known shape of particles%%
4  -
5  clear all
6  %%% experimental values; 'Rg' in cm3 and 'Mw' in g/mol%%
7  Rh = 233.71e-7; Mw = 0.9e7;
8  -
9  ro = 1;
10 M_mon = 286.57;
11 c_tot = (0.1449e-3)/(M_mon);
12 n_tot = c_tot*(6.022e23);
13 Vp = (4/3)*pi*(Rh^3);
14 mp = ro*Vp*(6.022e23)
15 P_n = mp/M_mon;
16 %%% n_mon = x %%%
17 syms x
18 eqn = ((x*M_mon.^2) + ((n_tot-x)/P_n).*mp.^2))./(
19 ((x.*M_mon) + ((n_tot-x)/P_n).*mp)) == Mw ;
20 S = solve(eqn,x);
21 -
22 n_mon = double(S)
23 n_pol = (n_tot - n_mon)/ P_n
24 n_tot
25 M_pol = n_pol*mp
26
27

```

Figure 6.7. Concentrations of yellow dyestuff are presented in mmol/L ($\lambda = 490 \text{ nm}$).

The check measurements for PL1Cl and aqueous HCl solutions before mixing. The measurements are done at room temperature.

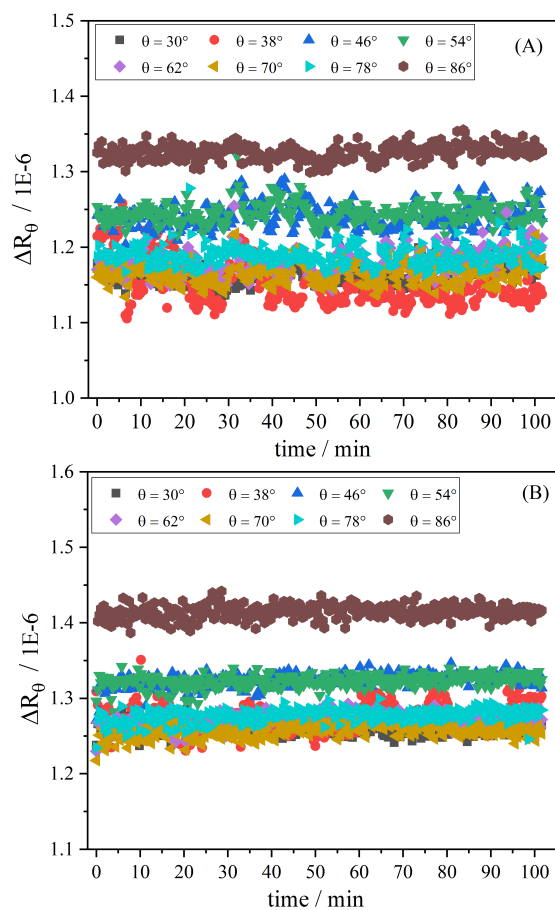


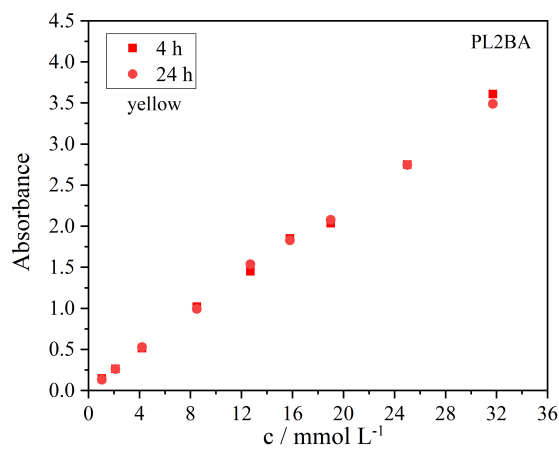
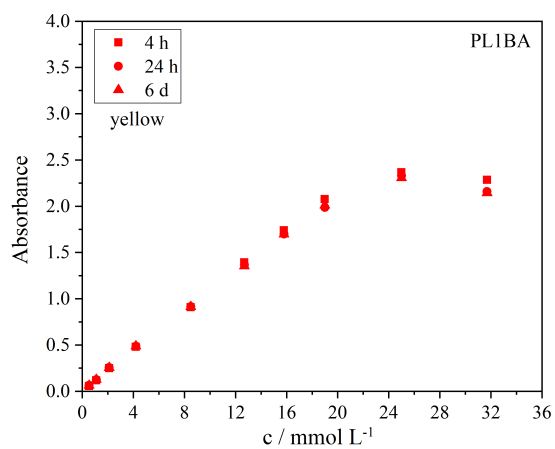
Figure 6.8. Scattered light in terms of rayleigh ratio ΔR_θ from (A) PL1Cl solvent and (B) HCl 1M.

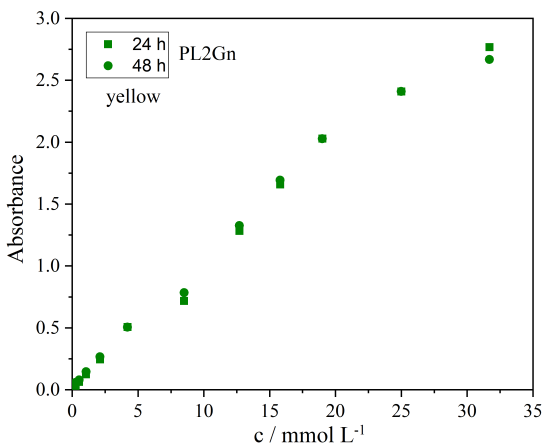
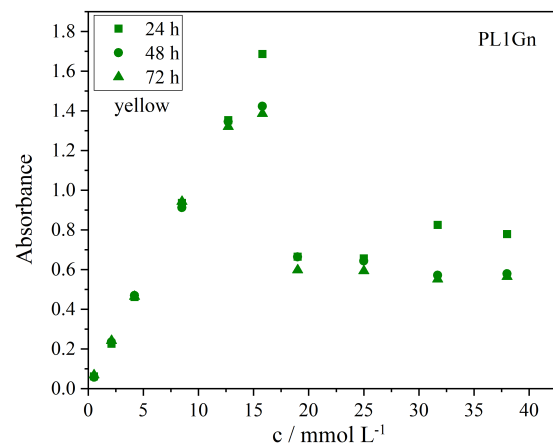
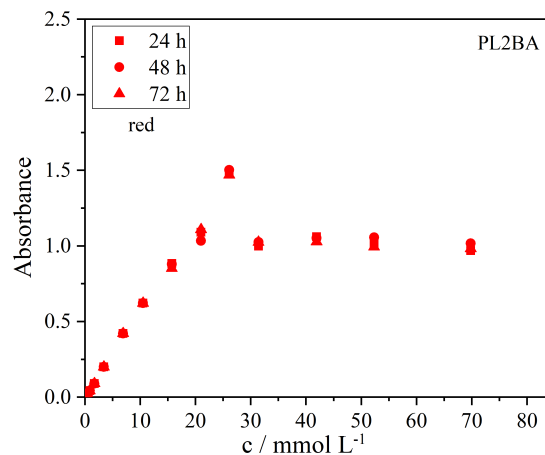
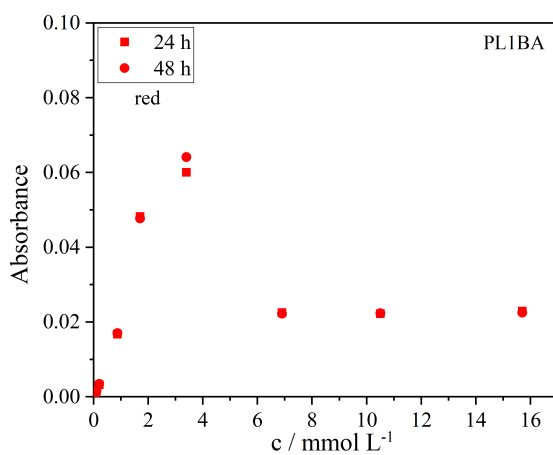
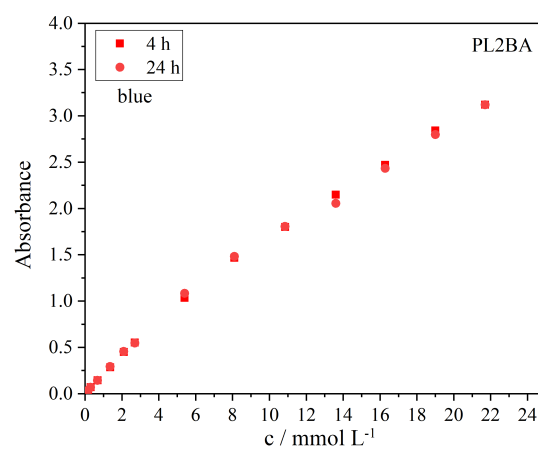
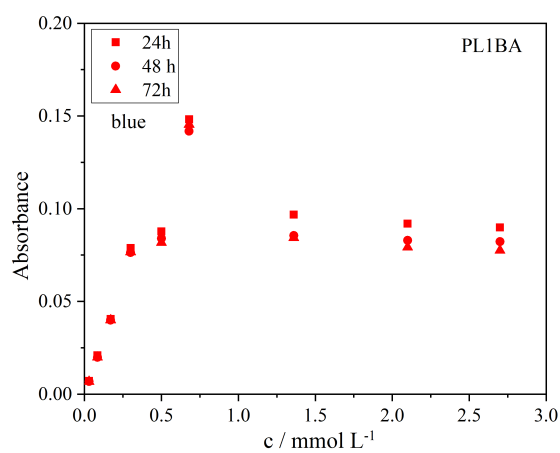
7

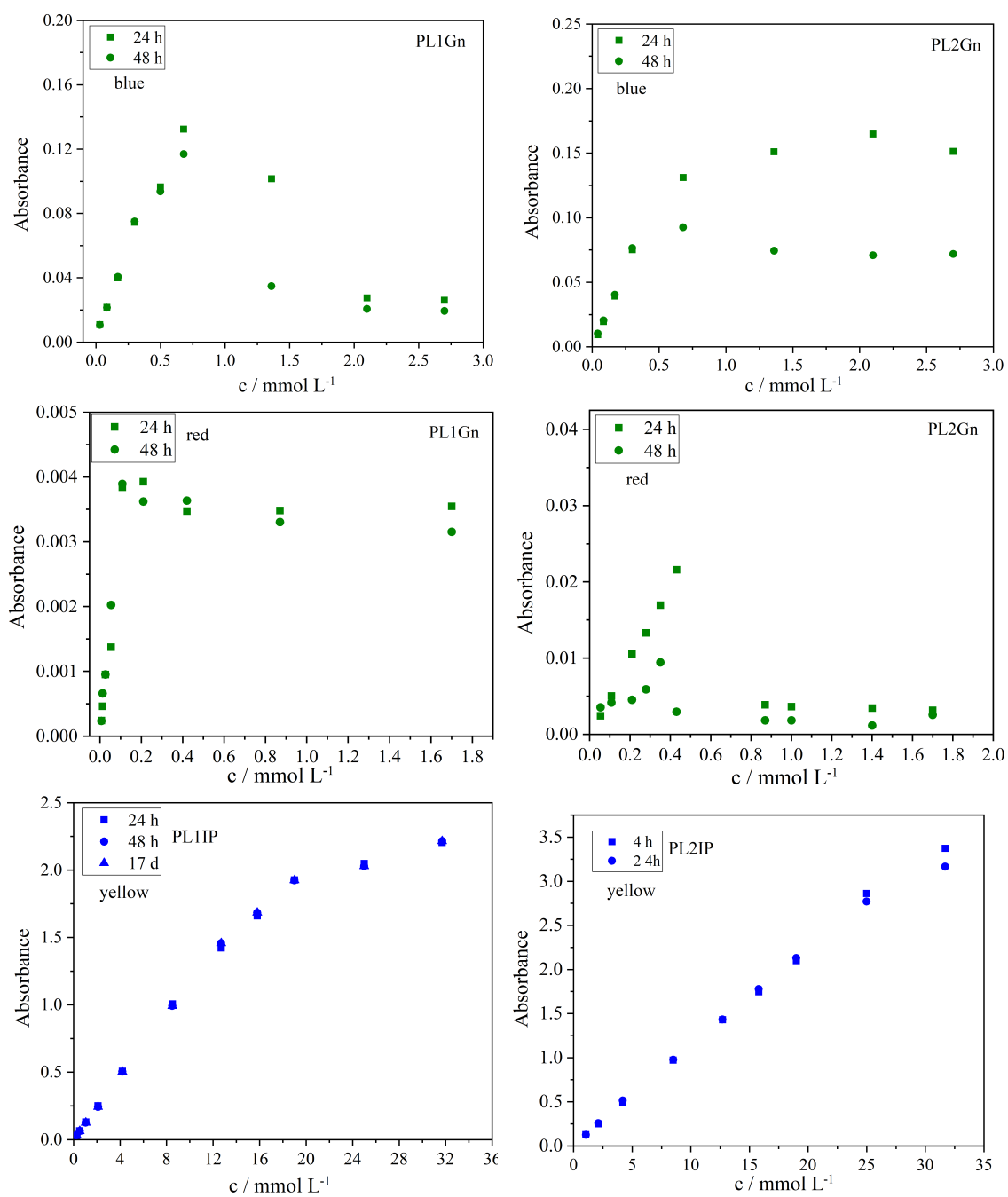
CHAPTER

Appendix II

Stability of acidic dyestuffs in PL1BA, PL2BA, PL1Gn, PL2Gn, PL1IP and PL2IP solvents.







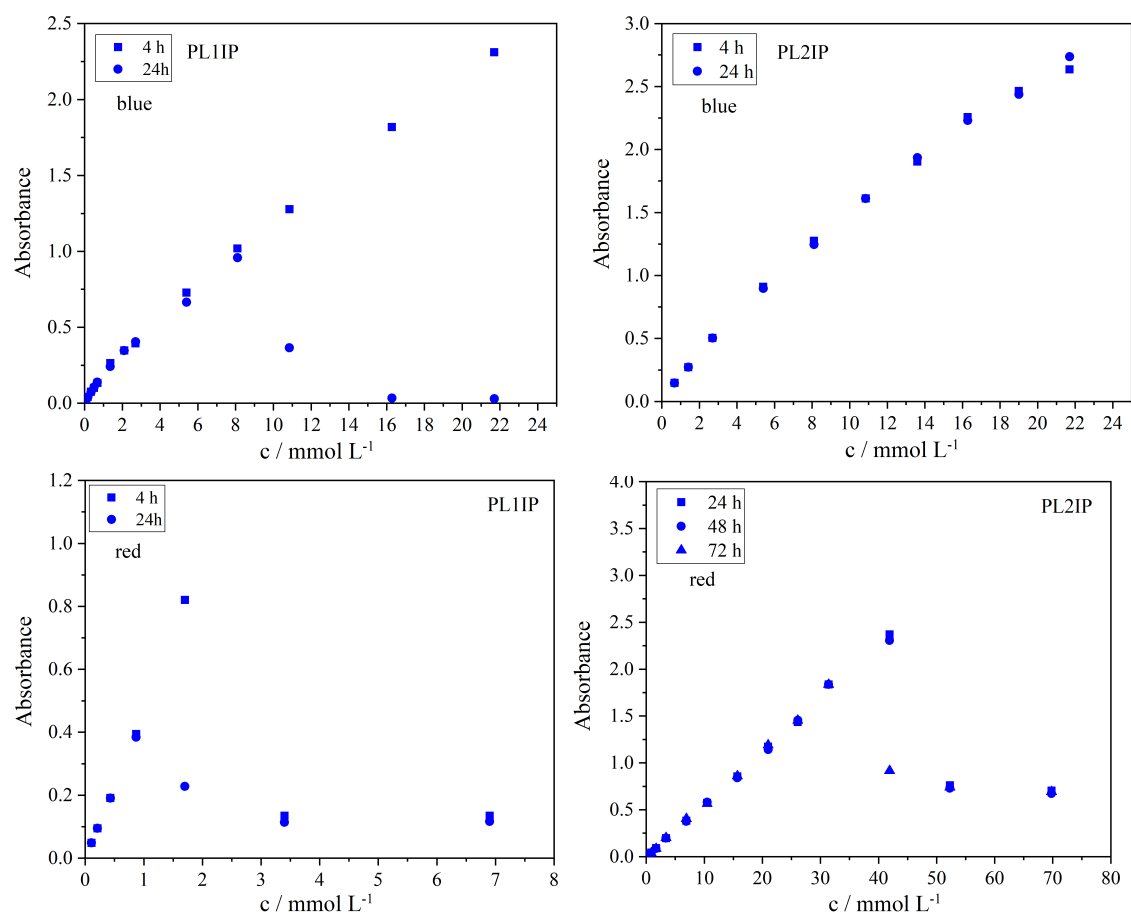


Figure 7.1. Evaluation of the stability of (A) yellow dyestuff at $\lambda = 490\text{ nm}$ (B) blue dyestuff at $\lambda = 600\text{ nm}$ and (C) red dyestuff at $\lambda = 585\text{ nm}$ in PL1BA, PL2BA, PL1Gn, PL2Gn, PL1IP and PL2IP solvents.

Absorbance spectra at different concentrations of yellow, red and blue dyestuffs in both PL1C1 and PL2P solvents. All measurements are done at the age of 4 hours and temperature of $T = 25^\circ\text{C}$.

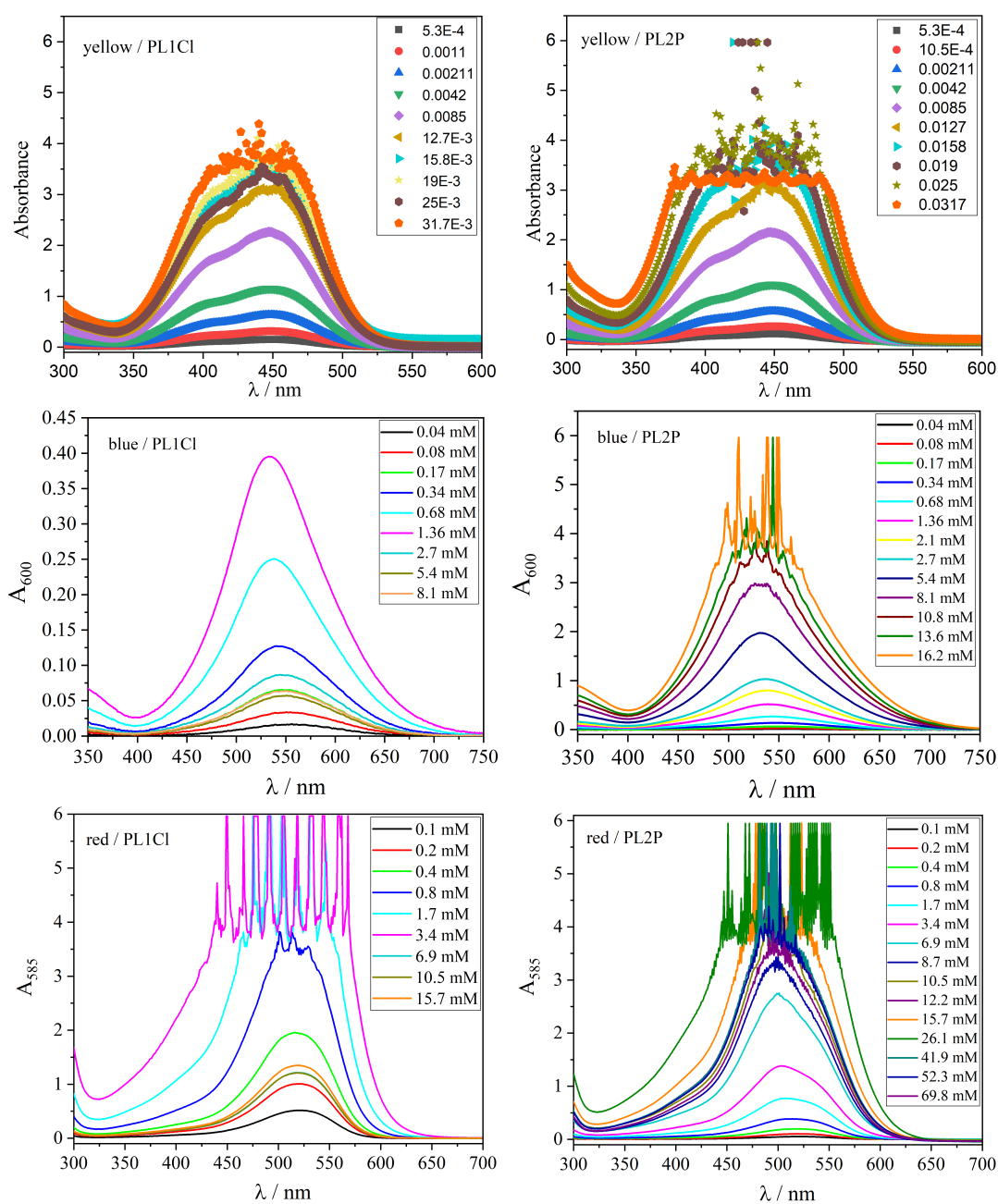


Figure 7.2. Absorbance spectra for different concentrations (in mmol/L) of yellow dyestuff at $\lambda = 490\text{ nm}$, blue dyestuff at $\lambda = 600\text{ nm}$ and red dyestuff at $\lambda = 585\text{ nm}$ in PL1Cl and PL2P solvents.

Molar extinctions and absorbance spectra in the presence of additives benzyl alcohol (BA), isopropanol (IP) and Guanidinium sulphate (Gn) at different concentrations of yellow, red and blue dyestuffs in both PL1Cl and PL2P solvents. All measurements are done at the age of 4 hours and temperature of $T = 25^\circ\text{C}$.

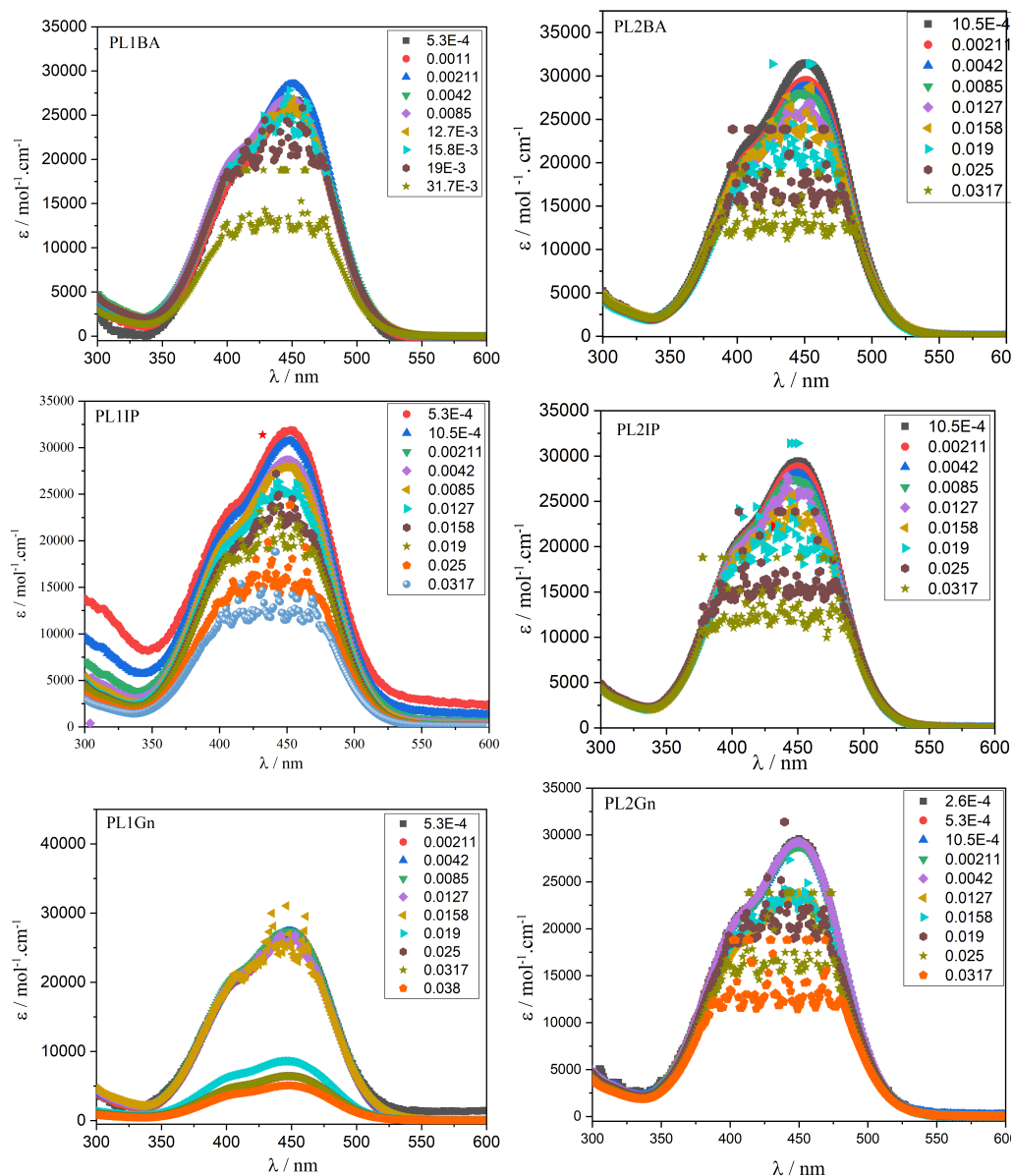


Figure 7.3. Molar extinctions for different concentrations (in mmol/L) of yellow dyestuff in different solvents. The spectra are measured at the wavelength of $\lambda = 490 \text{ nm}$ and the age of 24 hours.

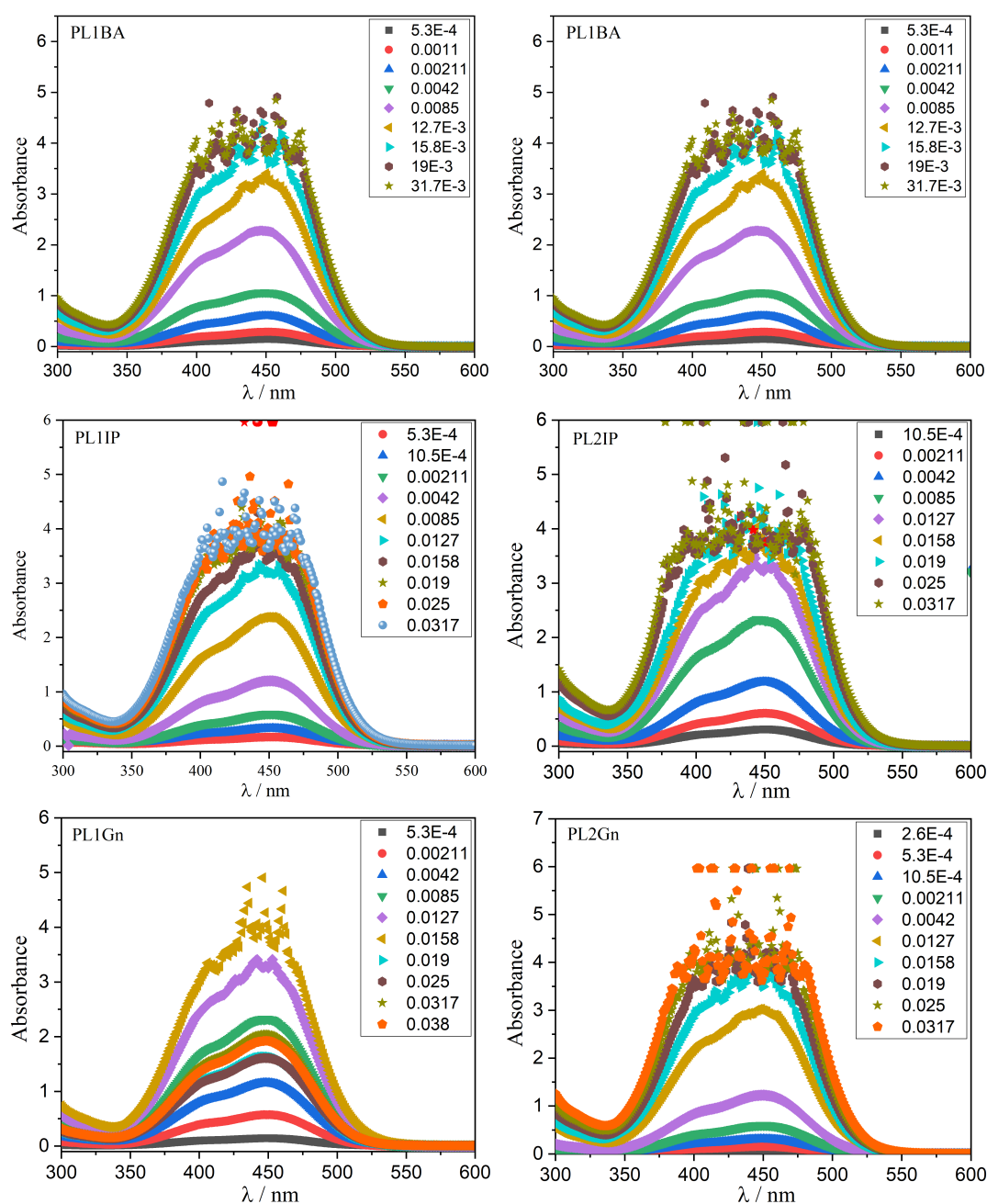


Figure 7.4. Absorbance spectra for different concentrations (in $mmol/L$) of yellow dyestuff in different solvents. The spectra are measured at the wavelength of $\lambda = 490\text{ nm}$ and the age of 24 hours.

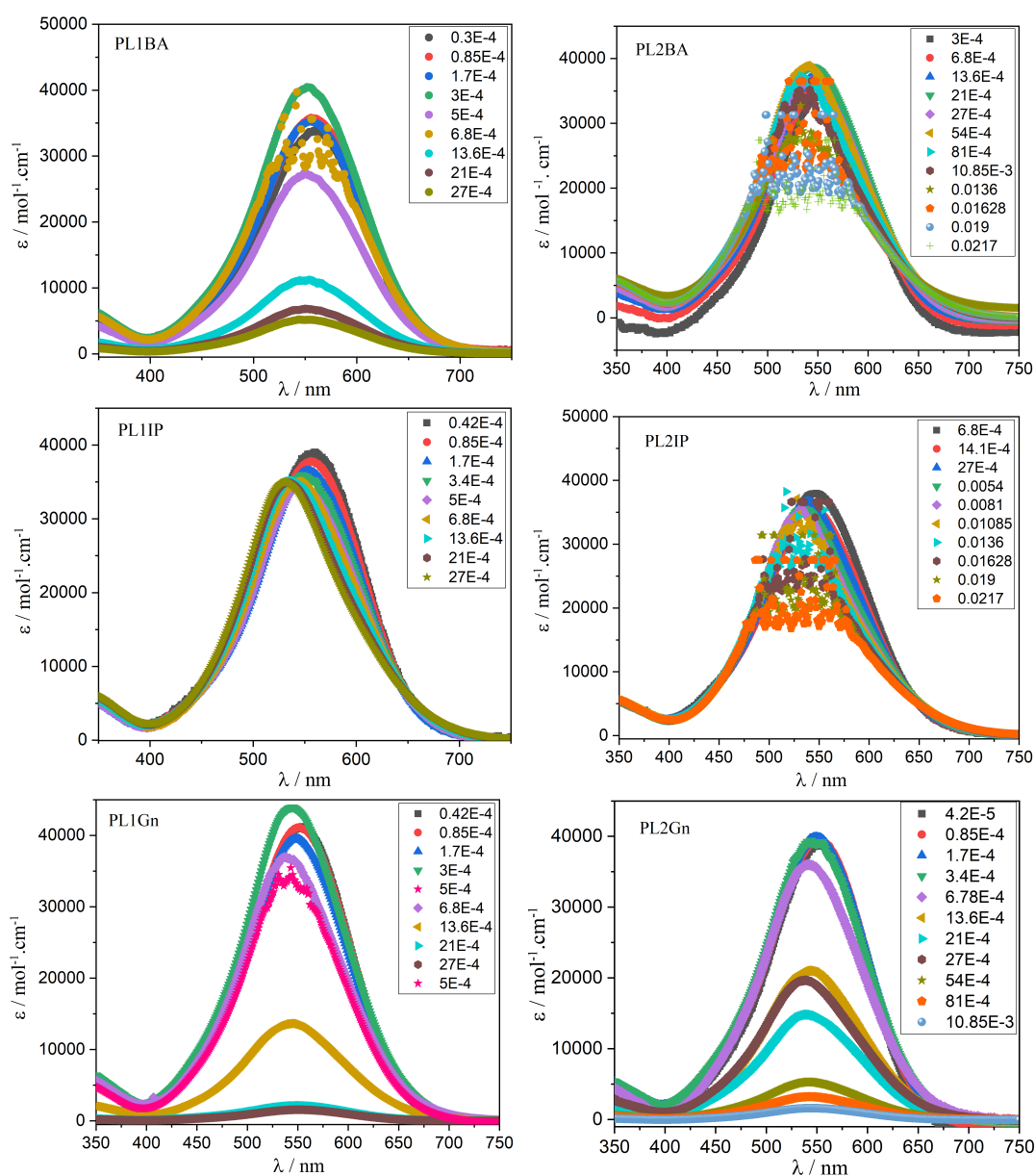


Figure 7.5. Molar extinctions for different concentrations (in mmol/L) of blue dyestuff in different solvents. The spectra are measured at the wavelength of $\lambda = 600 \text{ nm}$ and the age of 24 hours.

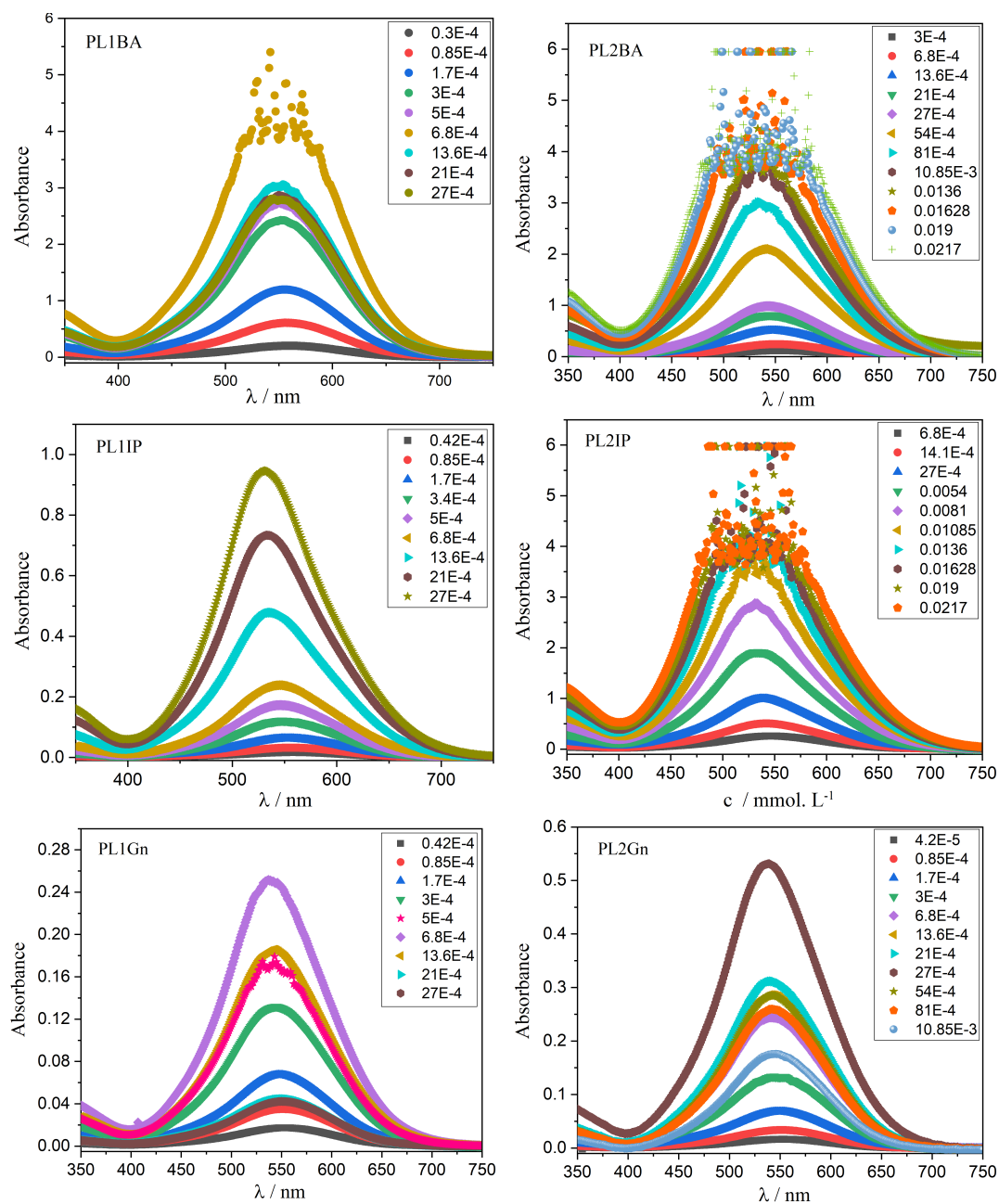


Figure 7.6. Absorbance spectra for different concentrations (in mmol/L) of blue dyestuff in different solvents. The spectra are measured at the wavelength of $\lambda = 600 \text{ nm}$ and the age of 24 hours.

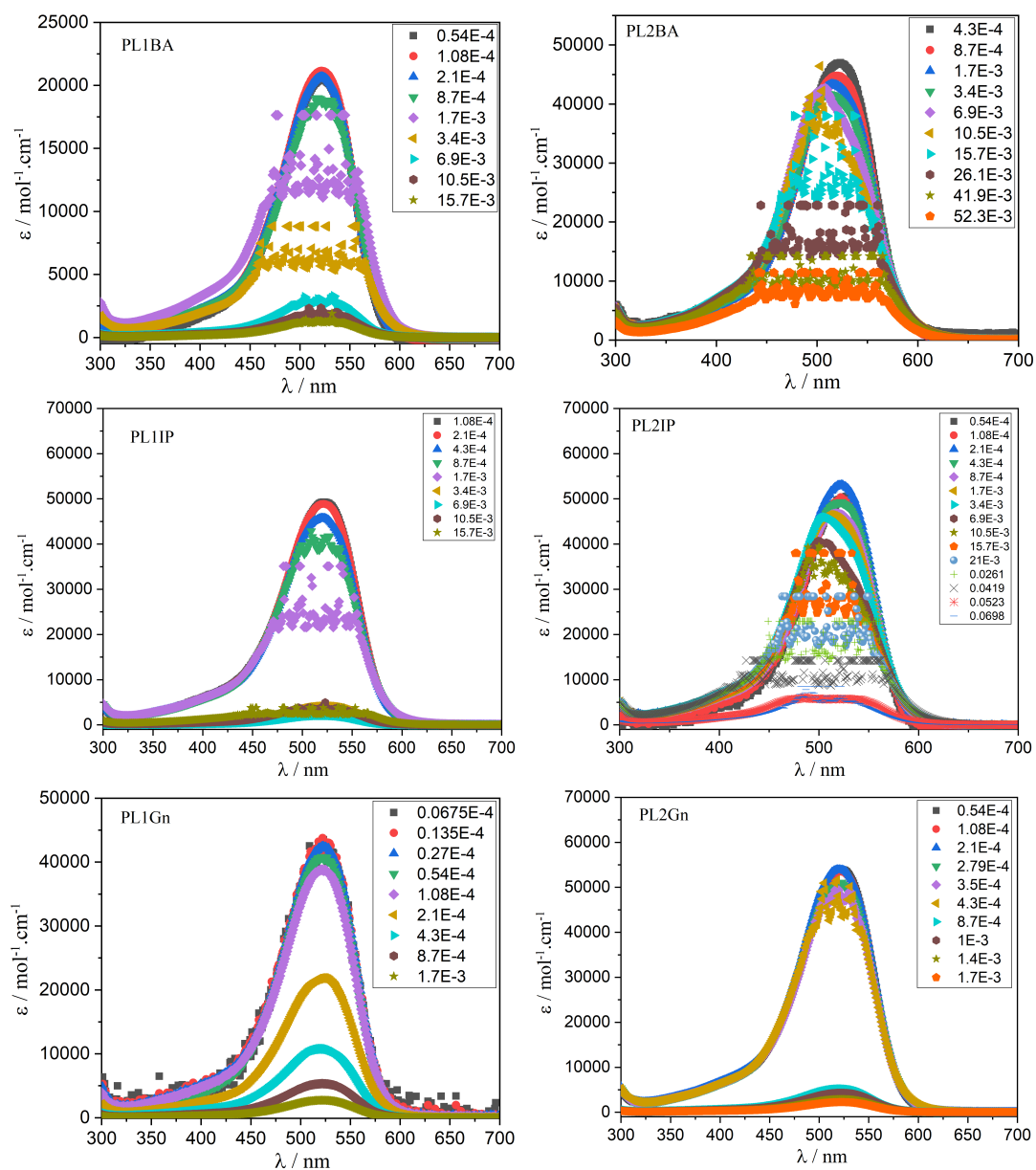


Figure 7.7. Molar extinctions for different concentrations (in mmol/L) of red dyestuff in different solvents. The spectra are measured at the wavelength of $\lambda = 585 \text{ nm}$ and the age of 24 hours.

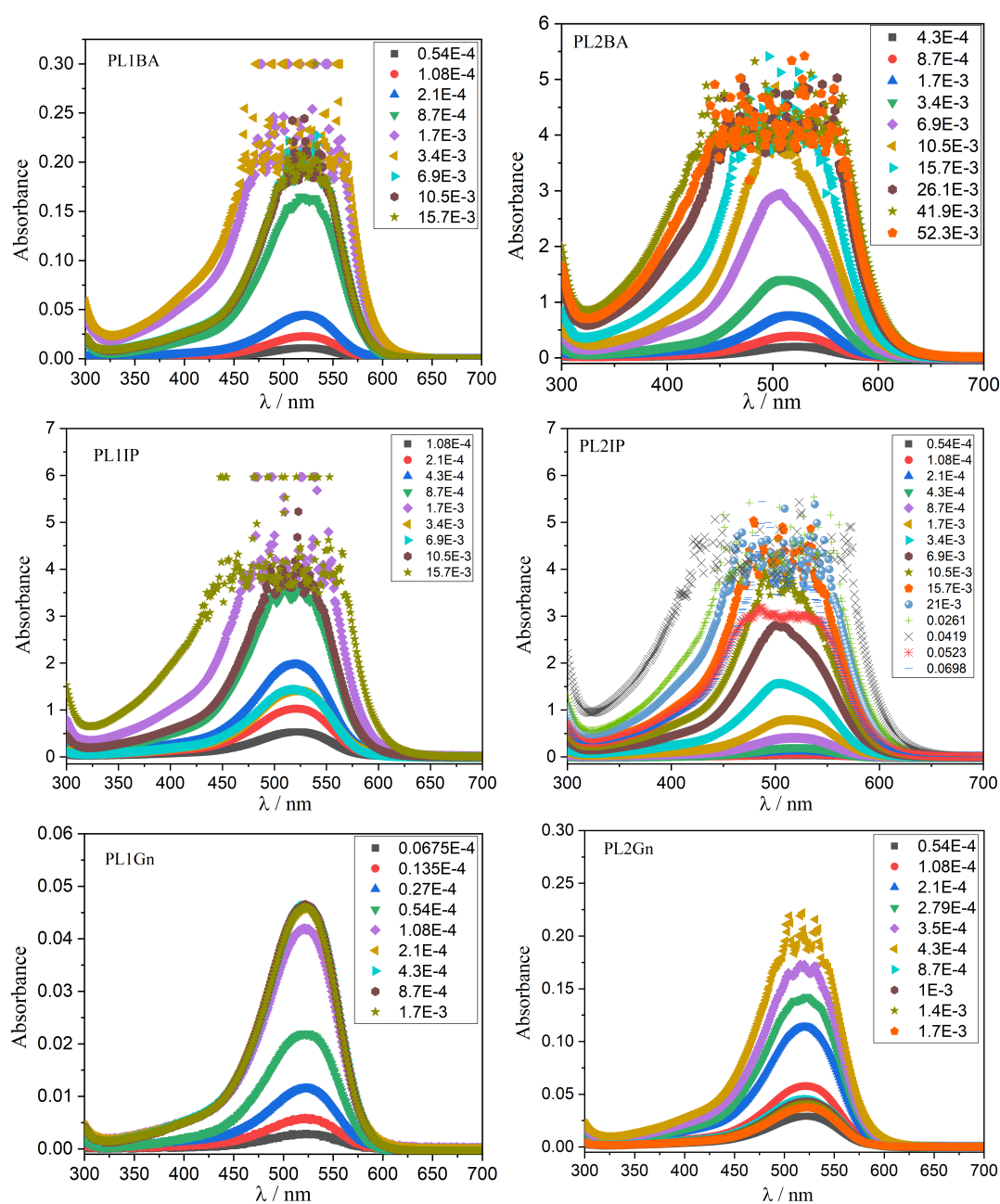


Figure 7.8. Absorbance spectra for different concentrations (in $mmol/L$) of red dyestuff in different solvents. The spectra are measured at the wavelength of $\lambda = 585 nm$ and the age of 24 hours.

CHAPTER 8

Appendix III

Molar extinctions and absorbance spectra of yellow, red and blue dyestuffs in the presence of different salts from Hofmeister series. All measurements are done at the age of 4 hours and temperature of $T = 25^{\circ}C$.

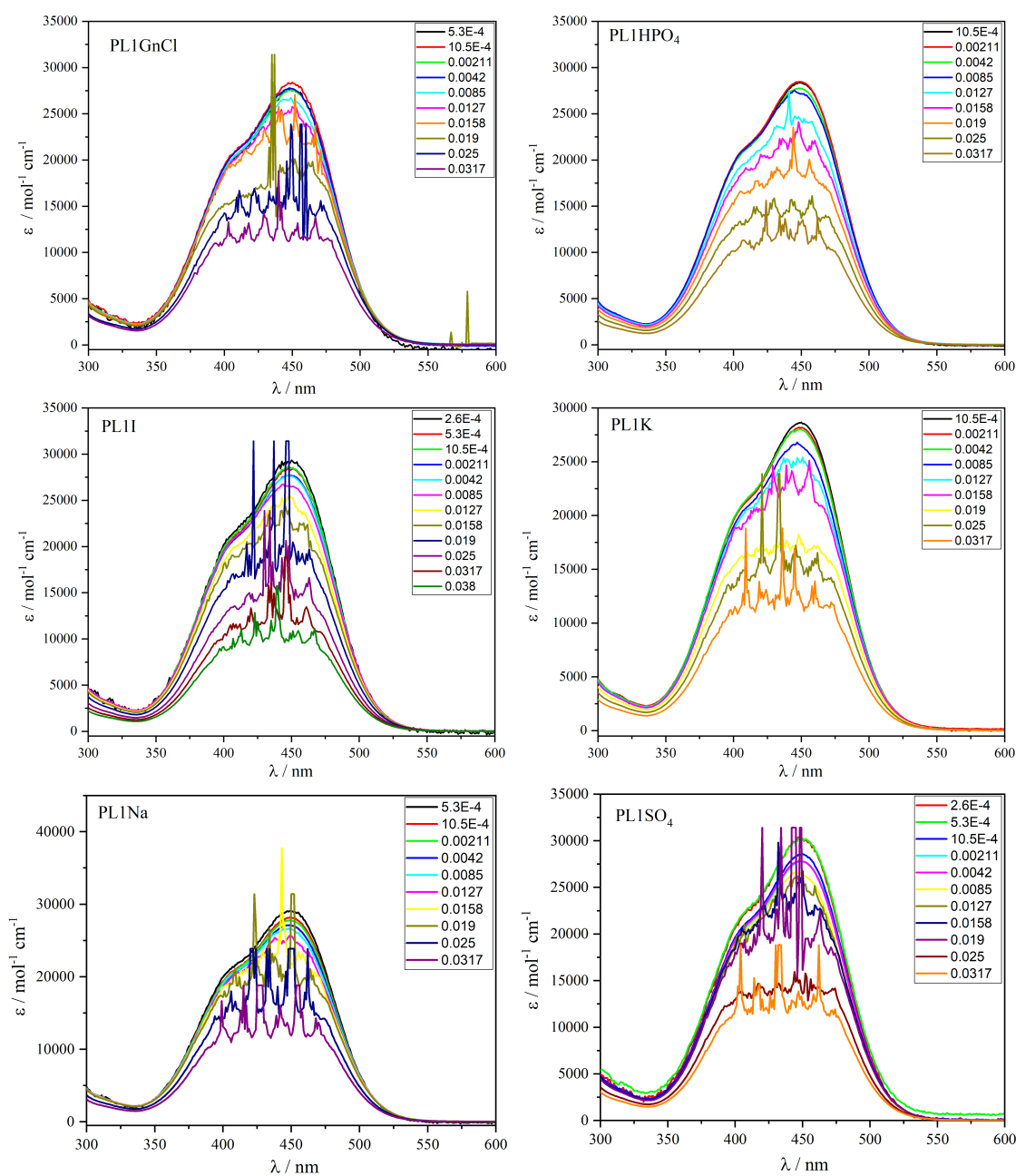


Figure 8.1. Concentrations of yellow dyestuff are presented in mmol/L ($\lambda = 490 \text{ nm}$).

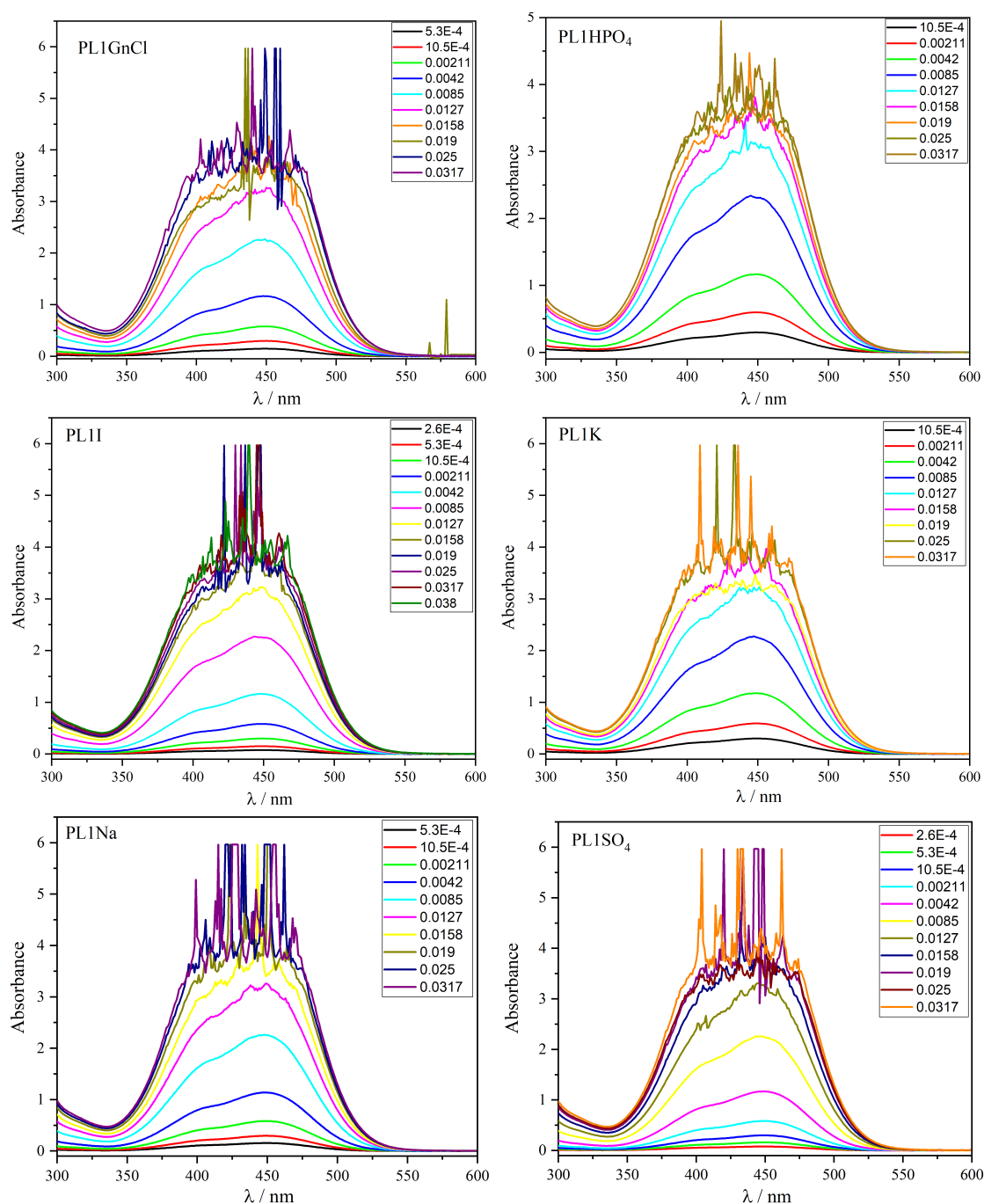


Figure 8.2. Absorbance spectra for different concentrations (in *mmol/L*) of yellow dyestuff in different solvents. The spectra are measured at the wavelength of $\lambda = 490$ nm and the age of 4 hours.

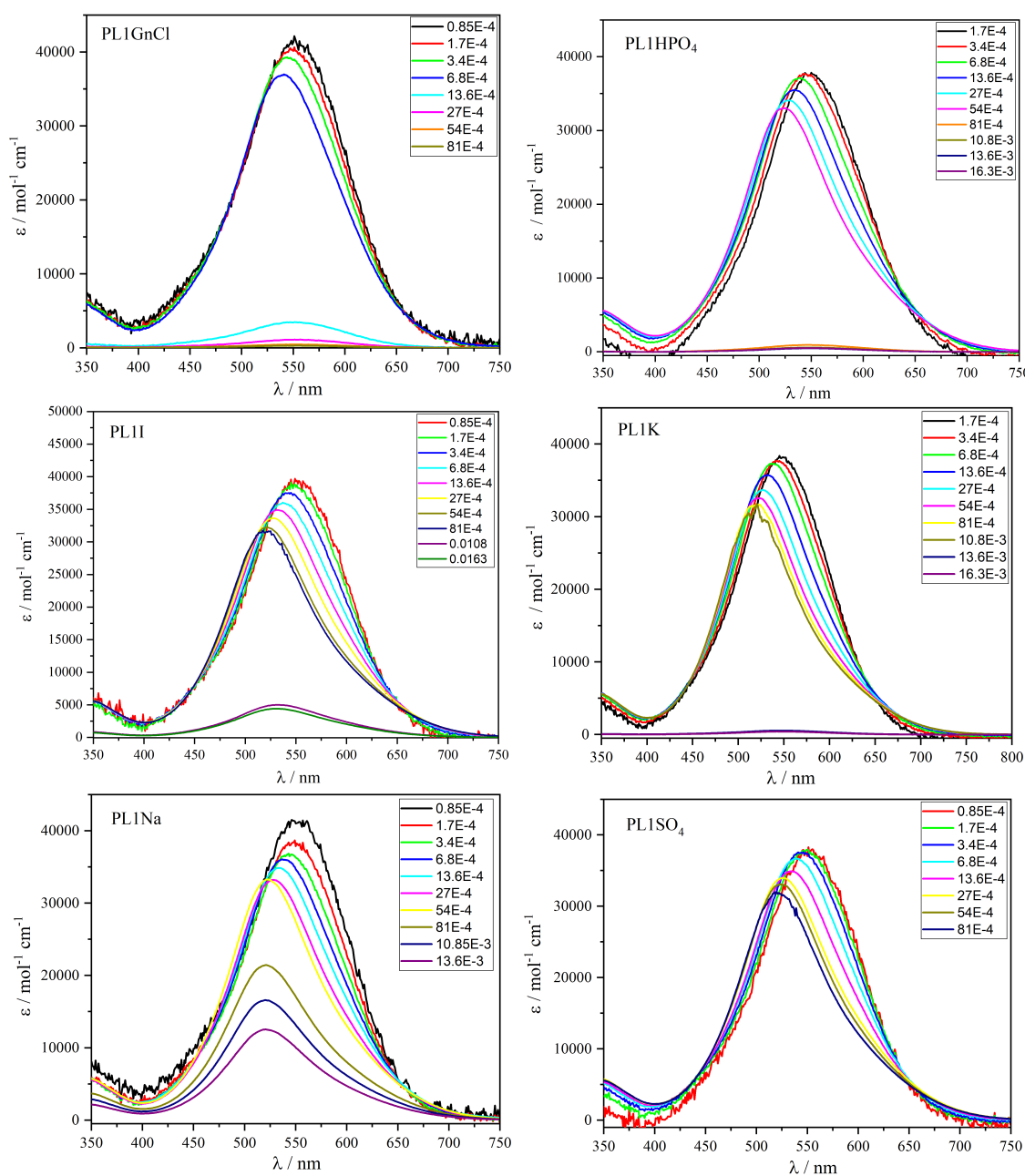


Figure 8.3. Molar extinctions for different concentrations (in mmol/L) of blue dyestuff in different solvents. The spectra are measured at the wavelength of $\lambda = 600 \text{ nm}$ and the age of 4 hours.

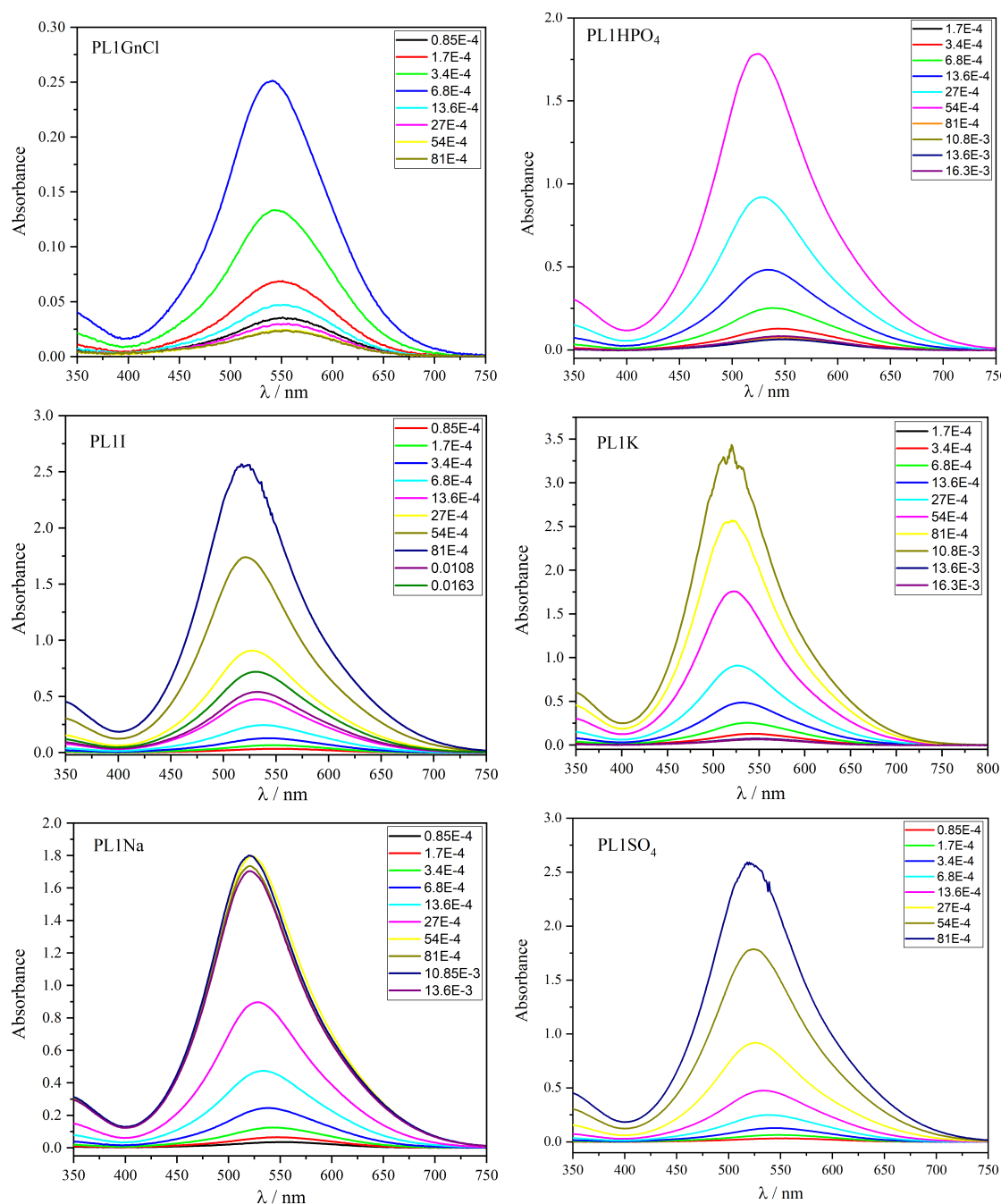


Figure 8.4. Absorbance spectra for different concentrations (in $mmol/L$) of blue dyestuff in different solvents. The spectra are measured at the wavelength of $\lambda = 600\text{ nm}$ and the age of 4 hours.

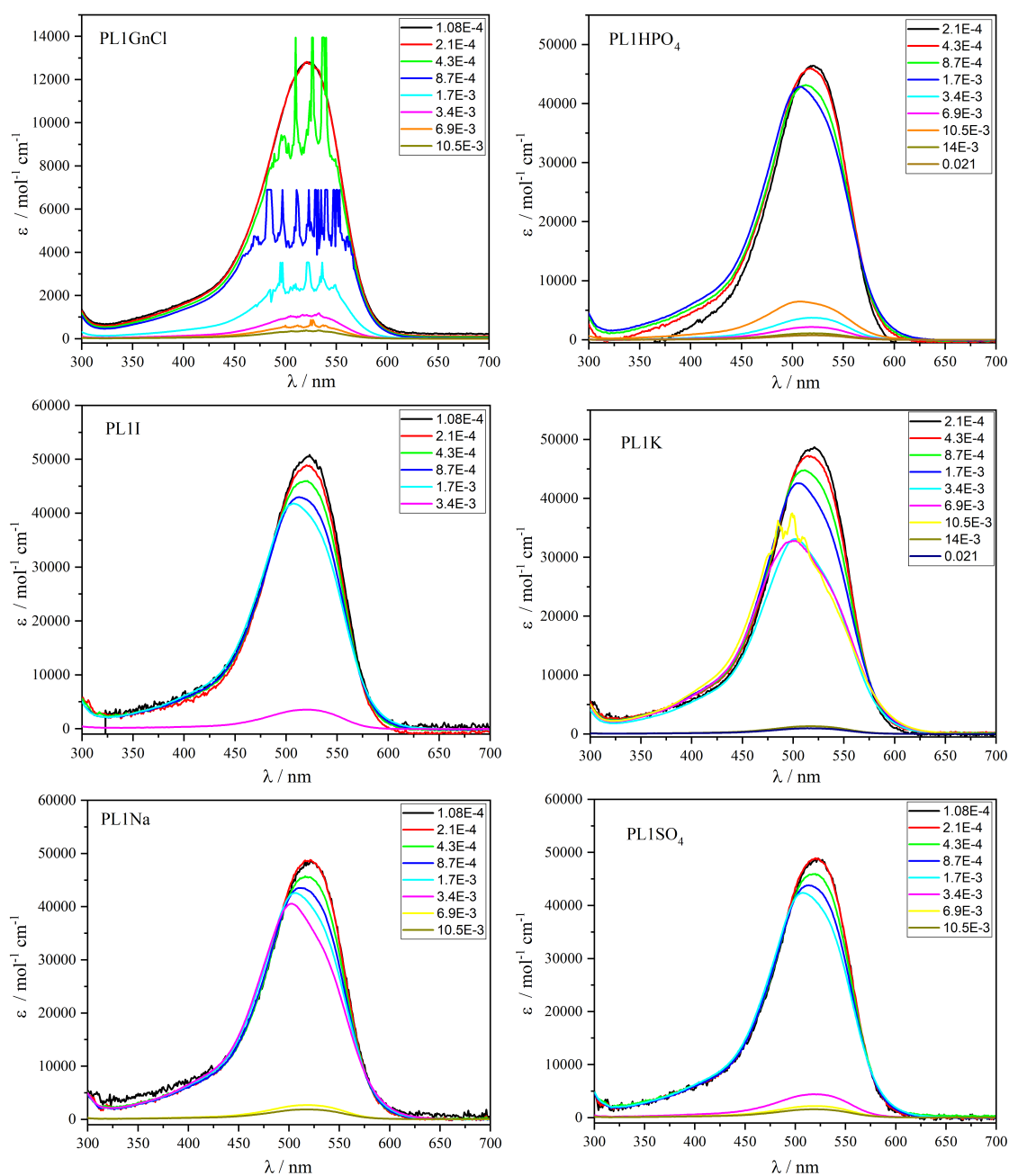


Figure 8.5. Molar extinctions for different concentrations (in mmol/L) of red dyestuff in different solvents. The spectra are measured at the wavelength of $\lambda = 585 \text{ nm}$ and the age of 4 hours.

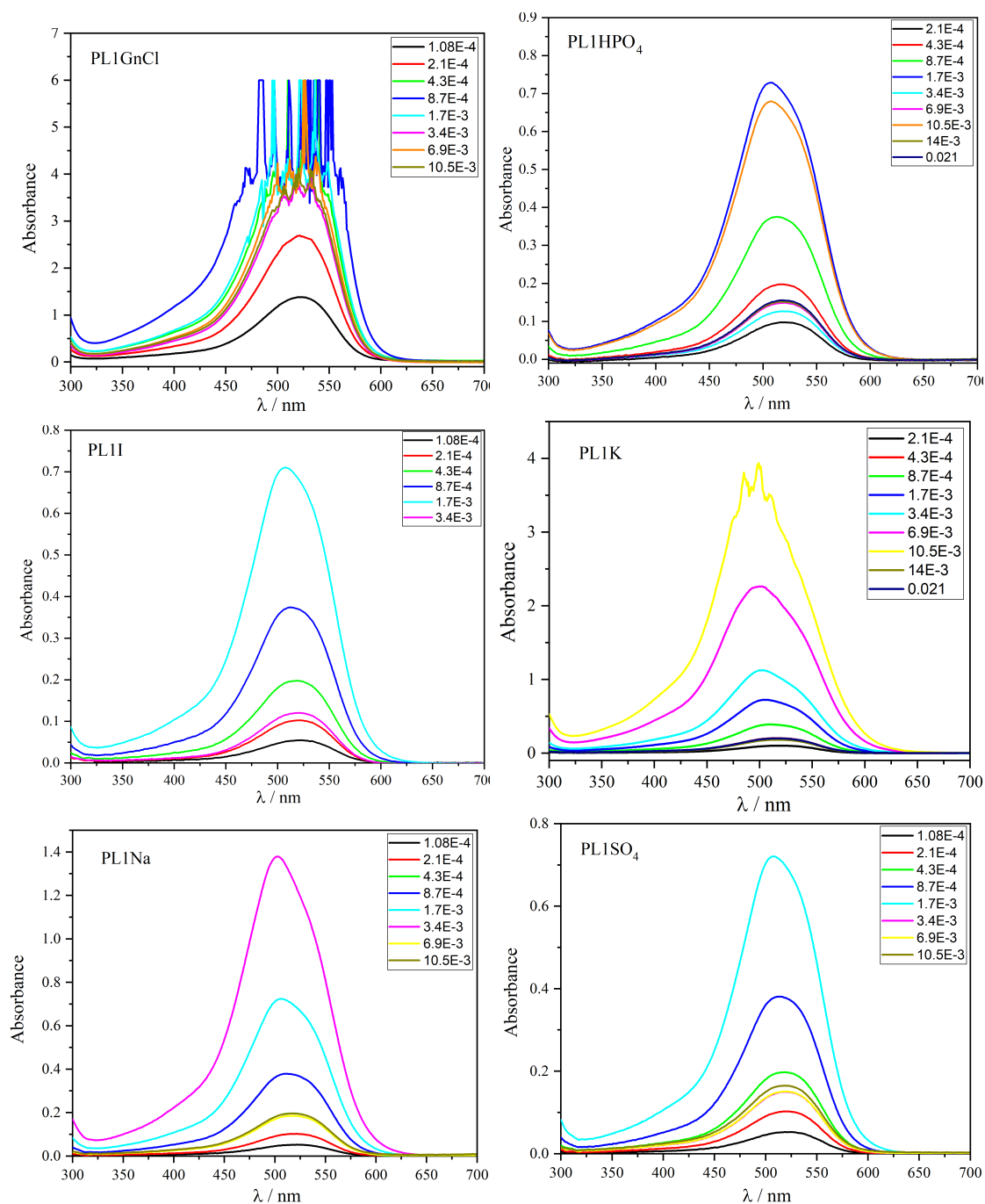


Figure 8.6. Absorbance spectra for different concentrations (in mmol/L) of red dyestuff in different solvents. The spectra are measured at the wavelength of $\lambda = 585 \text{ nm}$ and the age of 4 hours.

Bibliography

- [1] Robbins, C. R. *Chemical and Physical Behavior of Human Hair*. Springer-Verlag Berlin Heidelberg, (2012).
- [2] Donnan, F. G. and Harris, A. B. The osmotic pressure and conductivity of aqueous solutions of congo-red, and reversible membrane equilibria. *Journal of the Chemical Society, Transactions* **99**, 1554–1577 (1911).
- [3] Monahan, A. R. and Blossey, D. F. Aggregation of arylazonaphthols. i. dimerization of bonadur red in aqueous and methanolic systems. *The Journal of Physical Chemistry* **74**(23), 4014–4021 (1970).
- [4] Hamada, K., Kubota, H., Ichimura, A., Lijima, T., and Amiya, S. Aggregation of an azo dye in aqueous solution. *Berichte der Bunsengesellschaft für physikalische Chemie* **89**(8), 859–863 (1985).
- [5] Buwalda, R. T., Jonker, J. M., and Engberts, J. B. F. N. Aggregation of azo dyes with cationic amphiphiles at low concentrations in aqueous solution. *Langmuir* **15**(4), 1083–1089 (1999).
- [6] Neumann, B., Huber, K., and Pollmann, P. A comparative experimental study of the aggregation of acid red 266 in aqueous solution by use of 19f-nmr, uv/vis spectroscopy and static light scattering. *Phys. Chem. Chem. Phys.* **2**, 3687–3695 (2000).
- [7] Haller, R. Beitrage zur kenntnis der adsorptionsverbindungen. *Kolloid-Zeitschrift* **22**(4), 113–133, April (1918).
- [8] Hunger, K. *Industrial dyes: chemistry, properties, applications*. John Wiley & Sons, (2007).
- [9] Zollinger, H. The eighth george douglas lecture the dye and the substrate: The role of hydrophobic bonding in dyeing processes. *Journal of the Society of Dyers and Colourists* **81**(8), 345–350 (1965).

- [10] Ball, P., Meyer, U., and Zollinger, H. Crosslinking effects in reactive dyeing of protein fibers'. *Textile Research Journal* **56**(7), 447–456 (1986).
- [11] Zollinger, H. *Color chemistry: syntheses, properties, and applications of organic dyes and pigments*. John Wiley & Sons, (2003).
- [12] Peters, A. T. and Freeman, H. S. *Physico-Chemical principles of color chemistry*. Springer, (1996).
- [13] Peters, R. H. Nylon fibre: A study of the mechanism of the dyeing process with acid dyes. *Journal of the Society of Dyers and Colourists* **61**(4), 95–100 (1945).
- [14] Fierz, H. E. and Vittum, P. W. *Fundamental proecess of dye chemistry*. Springer, (1920).
- [15] Chakraborty, J. Fundamentals and practices in colouration of textiles. In Fundamentals and Practices in Colouration of Textiles, Chakraborty, J., editor, 184 – 191. Woodhead Publishing India (2010).
- [16] Booth, G., Zollinger, H., McLaren, K., Sharples, W. G., and Westwell, A. *Dyes, General Survey*. American Cancer Society, (2000).
- [17] MEGGY, A. B. The seventh john mercer lecture some recent developments in the theory of dyeing. *Journal of the Society of Dyers and Colourists* **66**(10), 510–521 (1950).
- [18] Collins, K. D. and Washabaugh, M. W. The hofmeister effect and the behaviour of water at interfaces. *Quarterly reviews of biophysics* **18**(4), 323–422 (1985).
- [19] Clarke, R. J. and Lüpfer, C. Influence of anions and cations on the dipole potential of phosphatidylcholine vesicles: a basis for the hofmeister effect. *Biophysical journal* **76**(5), 2614–2624 (1999).
- [20] Cacace, M., Landau, E., and Ramsden, J. The hofmeister series: salt and solvent effects on interfacial phenomena. *Quarterly reviews of biophysics* **30**(3), 241–277 (1997).
- [21] Gurau, M. C., Lim, S.-M., Castellana, E. T., Albertorio, F., Kataoka, S., and Cremer, P. S. On the mechanism of the hofmeister effect. *Journal of the American Chemical Society* **126**(34), 10522–10523 (2004).
- [22] Heuvingh, J., Zappa, M., and Fery, A. Salt softening of polyelectrolyte multilayer capsules. *Langmuir* **21**(7), 3165–3171 (2005).

- [23] Turshatov, A. A., Möbius, D., Bossi, M. L., Hell, S. W., Vedernikov, A. I., Lobova, N. A., Gromov, S. P., Alfimov, M. V., and Zaitsev, S. Y. Molecular organization of an amphiphilic styryl pyridinium dye in monolayers at the air/water interface in the presence of various anions. *Langmuir* **22**(4), 1571–1579 (2006).
- [24] Zhang, Y. and Cremer, P. S. Chemistry of hofmeister anions and osmolytes. *Annual Review of Physical Chemistry* **61**(1), 63–83 (2010). PMID: 20055667.
- [25] Medda, L., Barse, B., Cugia, F., Bostroem, M., Parsons, D. F., Ninham, B. W., Monduzzi, M., and Salis, A. Hofmeister challenges: ion binding and charge of the bsa protein as explicit examples. *Langmuir* **28**(47), 16355–16363 (2012).
- [26] Sowmiya, M., Tiwari, A. K., Eranna, G., Sharma, A. K., and Saha, S. K. Study of the binding interactions of a hemicyanine dye with nanotubes of β -cyclodextrin and effect of a hofmeister series of potassium salts. *The Journal of Physical Chemistry C* **118**(5), 2735–2748 (2014).
- [27] Oncsik, T., Trefalt, G., Borkovec, M., and Szilagyi, I. Specific ion effects on particle aggregation induced by monovalent salts within the hofmeister series. *Langmuir* **31**(13), 3799–3807 (2015).
- [28] Okur, H. I., Hladílková, J., Rembert, K. B., Cho, Y., Heyda, J., Dzubiella, J., Cremer, P. S., and Jungwirth, P. Beyond the hofmeister series: Ion-specific effects on proteins and their biological functions. *The Journal of Physical Chemistry B* **121**(9), 1997–2014 (2017).
- [29] Hofmeister, F. Zur lehre von der wirkung der salze. *Archiv fur experimentelle Pathologie und Pharmakologie* **25**(1), 1–30 (1888).
- [30] Vella, F. *Molecular biology of the cell (third edition)*, volume 22. Garland Publishing, New York and London, (1994).
- [31] Selkoe, D. Cell biology of the amyloid beta-protein precursor and the mechanism of alzheimer’s disease. *Annual review of cell biology* **10**, 373–403 (1994).
- [32] Holmes, W. C. The mechanism of staining the case for the physical theories. *Stain Technology* **4**(3), 75–80 (1929).
- [33] Hou, M. and Baughman, G. L. Predicting the precipitation of acid and direct dyes in natural waters. *Dyes and pigments* **18**(1), 35–46 (1992).
- [34] Inglés, S. E., Katzenstein, A., Schlenker, W., and Huber, K. Time-resolved recording of ionic dyestuff aggregation by static light scattering. *Langmuir* **16**(7), 3010–3018 (2000).

- [35] Gregory, P. and Stead, C. The degradation of water-soluble azo compounds by dilute sodium hypochlorite solution. *Journal of the Society of Dyers and Colourists* **94**(9), 402–407 (1978).
- [36] Haller, R. and Novack, A. —. *Transactions of the Faraday Society* **13**(86) (1920).
- [37] Ostwald, W. Über peptisation von farbstoffen durch neutralsalze. *Berichte der deutschen chemischen Gesellschaft (A and B Series)* **62**(5), 1194–1196 (1929).
- [38] Tanaka, R. Kolloidchemische studien an farbstoffsolten. *Kolloid-Zeitschrift* **53**(2), 200–205 (1930).
- [39] Tanaka, R. Kolloidchemische studien an farbstoffsolten. *Kolloid-Zeitschrift* **54**(2), 156–164 (1931).
- [40] Ostwald, W. The raising of the solubility of dyestuffs by neutral salts. *Transactions of the Faraday Society* **29**(140), 347–351 (1933).
- [41] Hamlin, J., Phillips, D., and Whiting, A. Uv/visible spectroscopic studies of the effects of common salt and urea upon reactive dye solutions. *Dyes and Pigments* **41**(1-2), 137–142 (1999).
- [42] Fedoseeva, M., Fita, P., Punzi, A., and Vauthey, E. Salt effect on the formation of dye aggregates at liquid/liquid interfaces studied by time-resolved surface second harmonic generation. *The Journal of Physical Chemistry C* **114**(32), 13774–13781 (2010).
- [43] Brederick, K. and Schumacher, C. Structure reactivity correlations of azo reactive dyes based on h-acid: Ii. dye degradation by hypochlorite. *Dyes and Pigments* **21**(1), 45–66 (1993).
- [44] Maurya, N. S., Mittal, A. K., Cornel, P., and Rother, E. Biosorption of dyes using dead macro fungi: effect of dye structure, ionic strength and ph. *Bioresource technology* **97**(3), 512–521 (2006).
- [45] Khattri, S. and Singh, M. Removal of malachite green from dye wastewater using neem sawdust by adsorption. *Journal of hazardous materials* **167**(1-3), 1089–1094 (2009).
- [46] Schmidt, A. and Kraenzlein, G. Pure β -anthraquinonyl-urea-chlorid and process of making same., , September 10 (1912). US Patent 1,038,003.
- [47] Seyewetz, A. and Chaix, E. —. *Bull. Sot. Chim.* **41**, 332 (1927).
- [48] Shilov, E. and Minajev, W. —. *Melliand Textilber* **15**, 224–226 (1934).
- [49] Shilov, E. —. *Melliand Textilber* **17**, 425 (1936).

- [50] Desai, N. F. and Giles, C. The oxidation of azo dyes and its relation to light fading. *Journal of the Society of Dyers and Colourists* **65**(12), 639–649 (1949).
- [51] Schmidt, O. —. *Ber. Dtsch. Chem. Ges.* **38**, 3201 (1905).
- [52] Nair, B. Final report on the safety assessment of benzyl alcohol, benzoic acid, and sodium benzoate. *International Journal of Toxicology* **20**(3), 23–50 (2001).
- [53] Logsdon, J. E. and Loke, R. A. *Isopropyl Alcohol*. American Cancer Society, (2000).
- [54] Reeves, R. L., Maggio, M. S., and Harkaway, S. A. A critical spectrophotometric analysis of the dimerization of some ionic azo dyes in aqueous solution. *Journal of Physical Chemistry* **83**(18), 2359–2368 (1979).
- [55] Michels, R., Sinemus, T., Hoffmann, J., Brutschy, B., and Huber, K. Co-aggregation of two anionic azo dyestuffs at a well-defined stoichiometry. *The Journal of Physical Chemistry B* **117**(28), 8611–8619 (2013).
- [56] Michels, R., Hertle, Y., Hellweg, T., and Huber, K. Kinetic and structural features of a dyestuff coaggregation studied by time-resolved static light scattering. *The Journal of Physical Chemistry B* **117**(48), 15165–15175 (2013). PMID: 24175927.
- [57] Lomakin, A., Teplow, D. B., Kirschner, D. A., and Benedek, G. B. Kinetic theory of fibrillogenesis of amyloid beta protein. *Proceedings of the National Academy of Sciences* **94**(15), 7942–7947 (1997).
- [58] Perkampus, H.-H. *UV-VIS Spectroscopy and its Applications*. Springer Science & Business Media, (2013).
- [59] Kuhn, H. and Foersterling, H.-D. *Principles of physical chemistry : understanding molecules, molecular assemblies, supramolecular machines*. John Wiley & Sons, (2000).
- [60] Tyndall, J. On the blue color of the sky, the polarization of skylight, and polarization of light by cloudy matter generally. *Journal of the Franklin Institute* **88**(1), 34–40 (1869).
- [61] Tyndall, J. Notes on the formation and phenomena of clouds. *Proceedings of the Royal Society of London* **1**(17), 317–319 (1869).
- [62] Rayleigh, L. On the transmission of light through an atmosphere containing small particles in suspension, and on the origin of the blue of the sky. *The London, Edinburgh, and Dublin Philosophical Magazine and Journal of Science* **47**(287), 375–384 (1899).

- [63] Rayleigh, L. On the scattering of light by spherical shells, and by complete spheres of periodic structure, when the refractivity is small. *Proceedings of the Royal Society of London. Series A, Containing Papers of a Mathematical and Physical Character* **94**(660), 296–300 (1918).
- [64] Kratochvil, P. *Classical light scattering from polymer solutions*. Elsevier, (1987).
- [65] Burchard, W., Schmidt, M., and Stockmayer, W. Influence of hydrodynamic preaveraging on quasi-elastic scattering from flexible linear and star-branched macromolecules. *Macromolecules* **13**(3), 580–587 (1980).
- [66] Burchard, W. *Static and dynamic light scattering from branched polymers and biopolymers*. Springer Berlin Heidelberg, Berlin, Heidelberg, (1983).
- [67] Chu, B. *Laser light scattering: basic principles and practice*. Courier Corporation, (2007).
- [68] Berne, B. J. and Pecora, R. *Dynamic light scattering: with applications to chemistry, biology, and physics*. Courier Corporation, (2000).
- [69] Pecora, R. *Dynamic light scattering: applications of photon correlation spectroscopy*. Springer Science & Business Media, (2013).
- [70] Zemb, T. and Lindner, P. *Neutron, X-Rays and Light. Scattering Methods Applied to Soft Condensed Matter*. North-Holland Delta. Elsevier Science, (2002).
- [71] Rubinstein, M. and Colby, R. *Polymer Physics*. OUP Oxford, (2003).
- [72] Einstein, A. Über die von der molekularkinetischen theorie der wärme geforderte bewegung von in ruhenden flüssigkeiten suspendierten teilchen. *Annalen der physik* **4** (1905).
- [73] Berry, G. Thermodynamic and conformational properties of polystyrene. i. light-scattering studies on dilute solutions of linear polystyrenes. *The Journal of Chemical Physics* **44**(12), 4550–4564 (1966).
- [74] Koppel, D. E. Analysis of macromolecular polydispersity in intensity correlation spectroscopy: The method of cumulants. *The Journal of Chemical Physics* **57**(11), 4814–4820 (1972).
- [75] Zimm, B. H. Apparatus and methods for measurement and interpretation of the angular variation of light scattering; preliminary results on polystyrene solutions. *The Journal of Chemical Physics* **16**(12), 1099–1116 (1948).
- [76] Guinier, A., Fournet, G., and Yudowitch, K. L. *Small-angle scattering of X-rays*. Wiley New York, (1955).

- [77] Neugebauer, T. Berechnung der lichtzerstreuung von fadenkettenlösungen. *Annalen der Physik* **434**(7 - 8), 509 – 533 (1943).
- [78] Debye, P. Molecular-weight determination by light scattering. *The Journal of Physical and Colloid Chemistry* **51**(1), 18–32 (1947).
- [79] Rayleigh, L. On the diffraction of light by spheres of small relative index. *Royal Society of London. Series A* **90**, 219 – 225 (1914).
- [80] Siegert, A. J. F. *On the fluctuations in signals returned by many independently moving scatterers*. [Cambridge, Mass.] Radiation Laboratory, Massachusetts Institute of Technology, (1943).
- [81] Dainty, J. C. *Laser Speckle and Related Phenomena*. Springer, (1975).
- [82] Burchard, W., Schmidt, M., and Stockmayer, W. Information on polydispersity and branching from combined quasi-elastic and integrated scattering. *Macromolecules* **13**(5), 1265–1272 (1980).
- [83] Schmidt, M. Combined integrated and dynamic light scattering by poly(α -benzyl glutamate) in a helocogenic solvent. *Macromolecules* **17**(4), 553–560 (1984).
- [84] Donkai, N., Inagaki, H., Kajiwara, K., Urakawa, H., and Schmidt, M. Dilute solution properties of imogolite. *Die Makromolekulare Chemie* **186**(12), 2623–2638 (1985).
- [85] Schmidt, M. and Burchard, W. Translational diffusion and hydrodynamic radius of unperturbed flexible chains. *Macromolecules* **14**(1), 210–211 (1981).
- [86] Flory, P. J. *Principles Of Polymer Chemistry*. Cornell University Press, (1953).
- [87] Liu, J., Rieger, J., and Huber, K. Analysis of the nucleation and growth of amorphous CaCO_3 by means of time-resolved static light scattering. *Langmuir* **24**(15), 8262–8271 (2008). PMID: 18611042.
- [88] Liu, J., Pancera, S., Boyko, V., Shukla, A., Narayanan, T., and Huber, K. Evaluation of the particle growth of amorphous calcium carbonate in water by means of the porod invariant from saxs. *Langmuir* **26**(22), 17405–17412 (2010). PMID: 20961060.
- [89] Smoluchowski. Drei Vorträge über Diffusion, Brownsche Bewegung und Koagulation von Kolloidteilchen. *Zeitschrift für Physik* **17**, 557–585, January (1916).
- [90] Brice, B. A. and Halwer, M. A differential refractometer*. *J. Opt. Soc. Am.* **41**(12), 1033–1037, Dec (1951).
- [91] Gernod Baur, *SLS-Systemtechnik. Differential refractometer: E-mail, 31.07.2016*.

- [92] Nüesch, F. and Grätzel, M. H-aggregation and correlated absorption and emission of a merocyanine dye in solution, at the surface and in the solid state. a link between crystal structure and photophysical properties. *Chemical physics* **193**(1-2), 1–17 (1995).
- [93] Eisfeld, A. and Briggs, J. The j-and h-bands of organic dye aggregates. *Chemical Physics* **324**(2-3), 376–384 (2006).
- [94] Pallagi, A., Tasi, Á., Gácsi, A., Csáti, M., Pálinkó, I., Peintler, G., and Sipos, P. The solubility of $\text{Ca}(\text{OH})_2$ in extremely concentrated NaOH solutions at 25 c. *Central European Journal of Chemistry* **10**(2), 332–337 (2012).
- [95] De Gennes, P.-G. and Gennes, P.-G. *Scaling concepts in polymer physics*. Cornell university press, (1979).